A VERSATILE PLATFORM FOR HIGHLY SENSITIVE ANALYSIS OF DNA SIZE, CONFORMATION, AND BINDING INTERACTIONS IN FREE SOLUTION

by
Sarah M. Friedrich

A dissertation submitted to Johns Hopkins University in conformity with the requirements for the degree of Doctor of Philosophy

Baltimore, Maryland
March, 2018

Abstract

Nucleic acid analysis has enhanced our understanding of biological processes and disease progression, elucidated the association of genetic variants and disease, and led to the design and implementation of new treatment strategies. These diverse applications require analysis of a variety of characteristics of nucleic acid molecules including size or length, detection or quantification of specific sequences, analysis of conformations or conformational changes, and observation of interactions between nucleic acids and other biomolecules. In addition to this variability in measurement modality, samples themselves can contain multiple species, further convoluting the complexity of analysis. Strategies that can detect rare or transient species, characterize population distributions, offer high sensitivity and quantification capabilities, and analyze small sample volumes enable the collection of rich multiparametric data from a single biosample. Platforms that integrate micro- and nano- fluidic operations with high sensitivity single molecule detection facilitate manipulation and detection of individual nucleic acid molecules and are well poised to fulfill this need.

In this thesis, we present a single molecule free solution hydrodynamic separation (SML-FSHS) platform for highly sensitive, quantitative, and versatile analysis of DNA molecules. Coupling a microfluidic size separation strategy with single molecule detection enables the unique ability to sensitively and quantitatively analyze multiple nucleic acid properties in free solution with extremely high detection sensitivity and low reagent consumption. The separation strategy achieves separation and sizing over a wide dynamic range, while single molecule burst analysis enables layered insight into DNA conformation and packing. Moreover, size-based separation of intermolecular interactions enables detection and quantification of binding properties in a free solution environment. The simplicity of operation, free solution conditions and potential for automation make the platform attractive for a variety of lab-based analysis. Such a system can be used to garner diverse information about DNA conformation, structure, and interactions.

We start by outlining the various DNA properties of interest and discuss some of the existing alternative microfluidic single molecule analysis methods (Chapter 1). Then, we introduce our SML-FSHS platform and demonstrate its utility for DNA length separation and sizing (Chapter 2). Next, we explore layered conformational analysis through a combination of hydrodynamic mobility and single molecule burst analysis (Chapter 3). Then, we further expand the platform's application to analyze intermolecular interactions including DNA hybridization and DNA-protein binding analysis (Chapter 4). Finally, we develop an integrated in-line preconcentration technique to further increase the concentration sensitivity beyond the capabilities of traditional methods (Chapter 5).

Advisor: Jeff Tza-Huei Wang
Committee members: Dr. Rebecca Schulman, Dr. Tian-Li Wang, Dr. Jeff Tza-Huei Wang

Preface

Now that the journey is nearly over, I find myself reflecting graciously on the opportunities and experiences I've had here at Hopkins. I applied to the biomedical engineering PhD program as a mechanical engineering major with undergraduate research experience in composite materials for structural applications—in short, lacking any significant experience or exposure to biomedical research. Despite my naivety, Hopkins and my advisor Dr. Tza-Huei "Jeff" Wang took a chance and accepted me into the school and into his research group. During my time here at Hopkins, I've had so many amazing opportunities to travel the world for conferences and collaborations, meet people from a diverse set of backgrounds, and continue my own personal development beyond what I had even considered when I began this journey. This document presents just a part of the learning and development that I've experienced during my doctoral research experience.

I am so grateful to the many people who have helped me to reach this goal. My advisor Dr. Jeff Wang has been extremely supportive and encouraging through every step. His mentoring style provided a balance of guidance and direction to keep me moving forward as well as space and freedom to explore my own ideas and further my own development as an independent thinker and researcher. I would also like to thank my mini-mentor Dr. Kelvin Liu. His work formed the foundation of my research, but his guidance also helped to shape my thinking, hone my writing skills, and encourage me to think practically while continuing to move forward. Every current member and alumni of the Wang lab is amazing. You all keep lab fun, interesting, and collaborative, and I am privileged to call you my colleagues and friends. Thank you for your advice and suggestions, stimulating conversations, and putting up with all my questions during lab meetings. I am also grateful to my undergraduate research advisor Dr. Erik Thostenson and additional mentor Dr.

Amanda Wu for inspiring and encouraging me to participate in research and pursue my graduate degree. I would also like to thank my research collaborators for providing ideas and expertise that elevated our projects and expanded my thinking. And of course, I must thank my friends and classmates, both old and new, who helped to celebrate successes, get past failures, and made this whole experience a lot more enjoyable.

Finally, I would like to thank my family. My parents, Stuart and Lyell, make me feel like I can do anything. Without their confidence in me, I don't know that I would have undertaken this endeavor. My sister, Rebekah, is an all-star who no matter how busy her crazy life can be, will always support and make time for family. And finally, I'd like to thank my boyfriend Tom, who supported and encouraged me through every part of this journey, whose stability helped to ground me when it felt too overwhelming, and who and made sure I didn't become a recluse sometime around year 4. I am so happy to be able to share this work with all of you who helped to bring it into being.

Table of Contents

List of Tables

List of Figures

Chapter 1

1. Single Molecule Analysis of Nucleic Acids in Micro- and Nano- Fluidics

1.1 Background

Nucleic acid molecules are information rich. They are involved in many critical biological processes including inheritance, cellular activities such as gene expression and cell differentiation, aging, disease progression, and epidemiology. Because nucleic acids are involved in so many aspects of human health, they hold great potential as broad-based biomarkers. For example, the utility of cell-free nucleic acids as biomarkers has been demonstrated for non-invasive diagnosis of fetal aneuploidy[1], non-invasive sequencing of the entire prenatal genome[2], and is being explored in diseases such as cancer[3, 4].

While much progress has been made in the understanding and categorization of nucleic acids based on their structure and function (e.g. DNA, transfer tRNA, messenger mRNA, micro miRNA, etc.), the cellular environment in which they form, act, and from which we sample, is quite complex. Analysis of these diverse species requires tools that are capable of accurate detection and characterization amidst a complex molecular background. Even more complex samples that contain nucleic acid material derived from multiple tissues, such as blood and urine, can provide a snapshot of systemic health for noninvasive health monitoring and diagnostics. In cancer diagnostics, a blood sample may even prove more descriptive than a tissue biopsy[5, 6], since branched evolution can introduce intratumor heterogeneity[7, 8]. Liquid biopsies, therefore, have the potential to enable patient health assessment that is both more complete and less invasive than standard methods, so long as the analysis techniques are capable of accurately probing these highly complex samples. Single molecule detection strategies enable observations of individual molecules, providing unparalleled detection sensitivity and quantification capability, and enabling analysis of subpopulations that are hidden in bulk measurements. Such high sensitivity detection also facilitates analysis of smaller sample sizes, which can be easier to collect and process, potentially be analyzed faster, and minimize the use of precious or rare samples. While compartmentalized amplification strategies, such as digital PCR[9-11] and enzyme-linked signal amplification[12, 13] can achieve highly sensitive detection and quantification of specific sequences and some epigenetic methylation modifications, many properties cannot be easily amplified, such as unbiased length, long range sequence structure, or conformational analysis. Moreover, multiplexing limitations restrict the number of sequences that can be probed within a single amplification reaction. Amplification strategies therefore have limited potential for multiparametric analysis of diverse populations within a single sample. For this reason, direct interrogation of single unamplified molecules holds the greatest potential for versatile, sensitive, and quantitative nucleic acid measurement technologies.

Manipulation and detection of single molecules requires a different tool set than bulk sample analysis. Microfluidic devices can play multiple roles in enhancing this particular form of analysis and detection. First, nucleic acid molecules are small, ranging from nm to μm in characteristic dimension. Detection of single molecules requires decreasing the background noise (signal) below the signal emitted by each molecule by limiting the sources of noise. This can be done by decreasing the size of the detection region to a similarly small area on the order of nm to μm in one or more dimensions. Microfluidic devices can be designed to complement high sensitivity single molecule detectors in multiple ways.[14] First, the sample volume can be confined to match the dimensions of the detection volume, ensuring that the molecule of interest is detected by the single molecule detector for higher mass detection efficiency. Second, micro-and nano- features can be designed to enhance the signal emitted from each molecule. Alternatively, compartmentalization of signal amplification reactions to small micro-reactors such as droplets or wells can be used to increase the local concentration of signal-emitting molecules. Finally, the precise manipulation of individual nucleic acid molecules requires tools and features on the same size scale (nm to μm). Such features can be integrated in microfluidic devices, enabling, for example, the ability to directly and accurately detect rare molecular species, as well as the ability to perform high throughput analysis to generate large data sets more quickly. Analysis of single nucleic acid molecules in microfluidic devices is thus poised to both address biological and clinical needs as well as overcome technological barriers that are currently limiting the implementation and use of emerging bioanalytical technologies.

1.2 Nucleic Acid Properties and Assessment Modalities

Nucleic acid molecules have numerous properties and attributes that hold unique utility in life science research and diagnostics applications. The need to assess such a broad range of properties for variable application requirements has led to the development of a number of approaches to assess these properties. These assessment modalities are summarized in **Fig. 1.1**.

From the most global perspective, we can observe the molecule's size or length. Length analysis is generally easier, cheaper, and faster than the methods required to analyze other characteristics, and can provide diagnostic and identification information. For example, the size distribution of circulating DNA can serve as a biomarker for cancer detection.[15, 16] Second, size selection can be an important identification or purification step: for example to isolate miRNA from the total RNA in a cell sample or fetal DNA from a mother's circulating DNA[17], and enzymatic digestion of whole genomes can produce a unique size distribution barcode that can be used to identify the organism[18].

However, many applications require a deeper analysis of the nucleic acid sequence. Sequence-specific detection to identify particular genes, diseases, or pathogens can be achieved with hybridization-based assays but requires prior knowledge of the identifying sequence and provides no information on any additional sequences present in the sample. In addition, broad-based detection, in which a single test can be used to diagnose multiple genetic variants, requires highly multiplexed analysis. Knowledge of the whole sequence in real-time would provide the richest source of information for broad-based analysis. Recently introduced single molecule sequencing platforms [19, 20] show promise towards this end, but error rates, cost, time, and intense data processing requirements will need to be overcome before this could be used as a routine clinical diagnostic.

Analysis of larger-scale abnormalities in the genome, such as structural variants and chromosomal rearrangements, requires analysis of extremely large DNA molecules and is difficult to achieve using the above methods. Optical mapping has been used to generate a physical genomic map of whole nucleic acid molecules or genomes by tabulating locations of specifically marked sequences.[21-24] However, mapping cannot be used to identify small structural changes below the optical resolution limit or to obtain sequence information in the untagged regions.

Moreover, it is becoming increasingly apparent that many changes in genetic expression are not caused by changes in sequence, but rather epigenetic modifications ranging from DNA methylation to histone modifications[25] and miRNA expression. Single molecule techniques are well poised to address this area, since these epigenetic modifications are difficult to copy in an amplification-based method. While some analysis has been demonstrated using optical mapping and single molecule sequencing, detection of only some of the many epigenetic modifications has been demonstrated thus far.

Finally, nucleic interactions with other biomolecules is a critical area of study for basic research as well as diagnostic and therapeutic development. Nucleic acids can interact with a wide array of other molecules including nucleic acids, proteins, and small molecules. Single molecule studies of interactions between molecules allows for more accurate kinetic and thermodynamic characterization as well as analysis of population distributions.[26-28] The unique requirements for characterization of binding interactions including kinetics, stoichiometry, affinity, and conformational changes has led to the development of many unique microfluidic and single molecule detection platforms specifically for this analytical subset.[29, 30]

Efforts to develop highly sensitive and quantitative analysis methods for such a broad range of properties has led to the development of a number of individual platforms that target only one or a small subset of these attributes. A summary of these recent advances is provided in ref [31]. Despite the value of developing specialized technologies to address these unmet needs, the simplicity and convenience of a single platform capable of analyzing multiple properties cannot be overlooked.

1.3. Summary and Thesis Objectives

The goal of this thesis was to develop a highly versatile platform capable of analyzing a wide array of nucleic acid properties and interactions with high specificity, quantification capabilities, and simplicity. To achieve this goal, we utilize an integrated microfluidic separation strategy with single molecule detection in a platform we call Single Molecule Free Solution Hydrodynamic Separation (SML-FSHS). In the first chapter, we introduce the integrated platform including the underlying Hydrodynamic Separation mechanism and the advantages of our modified single molecule detection platform. We then demonstrate the capability of the platform for length-based separation and sizing of DNA fragments with higher detection sensitivity, quantification, and sizing dynamic range than is capable with traditional existing methods.

Next, we expand the capabilities of the platform to analyze global DNA conformational changes. Combinatorial analysis of single molecule burst parameters and hydrodynamic mobility are used to assess large-scale changes to DNA molecules in free solution. We demonstrate sensitivity to DNA topology and simple salt conditions which each result in large-scale changes in average DNA radius. Finally, we demonstrate that this combinatorial analysis of mobility and single molecule burst analysis can be used to decouple DNA length, hydrodynamic radius, and total DNA content.

We then further expand the platform capabilities to detect DNA-biomolecule interactions including both DNA-DNA and DNA-protein interactions. For DNA-DNA interactions, we demonstrate quantitative analysis of hybridization efficiency as a result of DNA length and sequence complementarity. We also demonstrate the utility of the wide dynamic sizing range for the detection of rare target species. For DNA-protein analysis, we develop a high-throughput stacking method that enables quantitative analysis of binding affinity and stoichiometry. The separation method enables identification and quantification of the free and complexed species as well as estimation of the size-change associated with the binding event.

In the final chapter, we push the limits of the detection sensitivity by developing and integrating an in-line flow-based preconcentration method. Our preconcentration method utilizes a previously unreported phenomenon that we call Molecular Rheotaxis (MRT) to induce DNA migration without the use of an electric field. We demonstrate the ease with which MRT can be integrated SML-FSHS, becoming the only integrated DNA preconcentration and separation method that does not require an externally applied electric field. We use a numerical model in combination with experimental results to explore and describe the underlying mechanism, optimize the concentration parameters, and ultimately achieve over 10,000-fold DNA preconcentration. In so doing, we demonstrate an exceedingly versatile, quantitative, and sensitive DNA separation and analysis platforms.

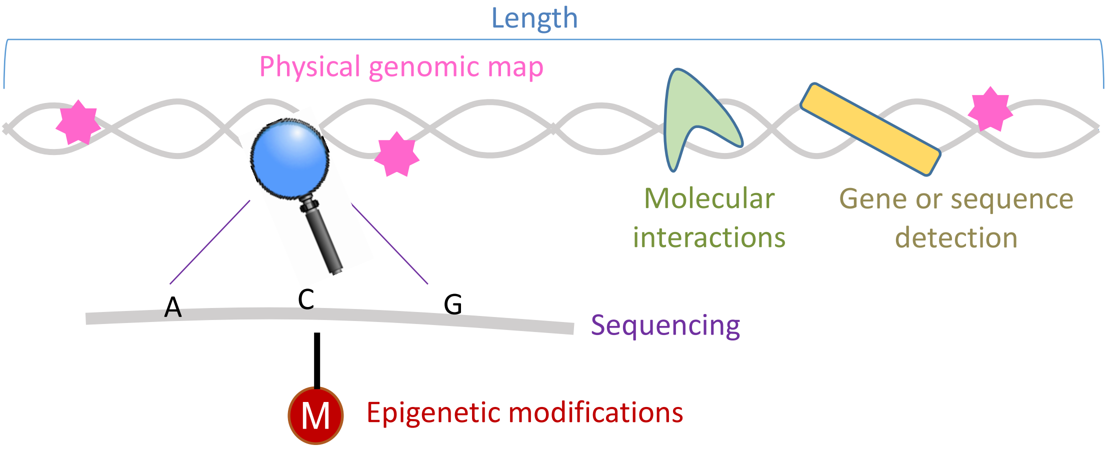
Length
Physical genomic map
Molecular interactions
Gene or sequence detection
A
C
G
Sequencing
M
Epigenetic modifications

Figure 1.1: Categorization of nucleic acid assessment modalities.

Commonly assessed properties in microfluidic single molecule analysis of DNA molecules include length or size analysis, sequence-specific detection, physical genomic mapping, single molecule sequencing, detection of epigenetic modifications, and characterization of molecular interactions involving nucleic acid molecules. Reproduced from Ref. [31] with permission from The Royal Society of Chemistry.

Chapter 2

2. Single Molecule Free Solution Hydrodynamic Separation

2.1 Background

In this chapter, we introduce our Single Molecule Free Solutions Hydrodynamic Separation (SML-FSHS) platform and its utility for length-based separation and sizing of DNA molecules.[32, 33] High resolution separation of DNA and other biological molecules remains an important method for biological study. The length of a nucleic acid molecule is one of the simplest parameters to measure and is useful for many purposes. First, the size distribution of DNA from a complex sample, such as blood, can be used to assess the origin (maternal or fetal[17], cancerous or normal tissue[15, 16, 34, 35]) or disease status. Second, because gel electrophoresis size separations are relatively cheap, easy and routine benchtop techniques, many assays have been designed to link size analysis with other characteristics, such as restriction enzymatic digestion of genomic DNA for pathogen identification[36] and forensic DNA fingerprinting[37], and multiplexed ligation-dependent probe amplification (MLPA) for sequence-specific detection and quantification[38]. Thus, numerous characteristics can be probed via a simple, sensitive, and robust separation method.

The most common analytical methods used to separate DNA are electrophoretic. These methods exploit the high charge density of DNA molecules to induce migration in an electric field. Conventional benchtop gel electrophoresis is simple and inexpensive but is not capable of handling small sample volumes and has limited separation resolution and detection sensitivity. Capillary electrophoresis (CE) miniaturizes this electrophoretic method, enabling increased separation resolution and detection sensitivity with significantly decreased separation times and reagent consumption. The availability and simplicity of commercial CE instruments has further enhanced the widespread integration of CE in standard lab workflows. Despite the popularity of these platforms, there are limitations. Typically, a polymeric sieving matrix or drag-tag conjugation scheme is required to induce a size-dependence in the electrophoretic mobility of DNA molecules. Moreover, wall coatings are often required to reduce the effects of electroosmotic flow, steps of capillary cleaning, priming, and coating between separations can limit sample throughput, the high voltages and complex injection schemes involved in some CE and microchip electrophoresis platforms can introduce added complexities and unintended consequences, and the sizing range that can be separated in a single run is limited.[32, 39-41]

Hydrodynamic separations are an alternative method. Sample components are separated based on the size-dependent sampling of flow streamlines in either an open capillary tube or a bead-packed column. Packed-column HDC refers to columns packed with solid inert beads, with separation occurring within the interstitial medium between the beads. It is generally used to characterize polymer and particle distributions, particularly through the implementation of multiple detectors.[42] However, open tubular HDC in microcapillaries with inner diameters ~1-5 μm has enabled size separation of macromolecules[43] including denatured proteins[44] and nucleic acid fragments[45, 46] with comparable resolution to electrophoresis. The advantages of this open microcapillary Free Solution Hydrodynamic Separation (FSHS) include (1) ultralow sample consumption (picoliters), (2) wide dynamic sizing range in a single run, and (3) the quantifiable relationship between elution time and effective radius.[32, 47] The sizing range and resolution is also tunable through changes in capillary dimensions, temperature, and elution buffer.[46-48]

Laser-induced-fluorescence (LIF) detection has been used in both CE and FSHS to improve the detection sensitivity.[46, 49-51] In fact, single molecule detection in capillary electrophoresis (SM-CE) has been demonstrated.[52] However, the mismatch between the extremely small single molecule confocal observation volume (~ 1 fL) and the larger capillary cross section results in low mass detection efficiency (<1%), which limits detection sensitivity and quantification accuracy and increases the variability of the single molecule bursts that are detected.[32] The small channel cross-section used for FSHS provides a unique opportunity for single molecule detection and quantification. Cylindrical Illumination Confocal Spectroscopy (CICS), a modified single molecule (SML) confocal detection system, can span the entire microcapillary lumen.[53] This allows for near 100% mass detection efficiency and highly uniform fluorescent bursts regardless of the molecular trajectory through the microchannel and observation volume. Integrating CICS with free solution hydrodynamic separation couples the benefits of FSHS with the high sensitivity and additional analytical capabilities of single molecule detection.[32, 33, 48] This integrated single molecule free solution hydrodynamic separation (SML-FSHS) is one of the most sensitive and quantitative separation platforms for DNA length analysis.[32, 54]

In this chapter, we introduce the SML-FSHS platform and its use for DNA length separation and sizing. We start by introducing the theory underlying both the separation mechanism and the CICS single molecule detection platform. We introduce the integrated SML-FSHS platform and its operation. Finally, we demonstrate the unique capabilities that make it so attractive for DNA fragment length sizing analysis including extremely low sample consumption, high quantification capabilities, extremely high mass detection sensitivity, and high resolution over a wide dynamic sizing range.

2.2 Theory

2.2.1 Free Solution Hydrodynamic Separation

The separation mechanism underlying Free Solution Hydrodynamic Separation is shared by all Hydrodynamic Chromatography (HDC) methods.[42] In short, sample components are separated based on the size-dependent sampling of flow streamlines. A schematic is shown in **Fig. 2.1**. Laminar flow in a capillary has a parabolic velocity profile due to the no-slip boundary condition at the capillary walls. Molecules in the capillary are free to diffuse across the cross section of the channel and sample many different flow streams. Over a long capillary length, this diffusion results in a flow velocity that is an average of the sampled flow streams. The average velocity of the solute is thus the integrated average of all velocity streams. The center of mass of a larger molecule, however, is excluded from the walls by its effective radius. This prevents larger molecules from sampling the slowest flow regimes near the wall, resulting in a faster average velocity. Thus, larger molecules will move at a faster average velocity than smaller molecules, with the solute moving the slowest.

FSHS is performed in a long capillary is filled with a running buffer. A short pL-sized sample plug is hydrodynamically injected into the beginning of the capillary and subsequently driven down the length of the capillary. As the plug travels down the length of the capillary, the difference in average velocities between the component species causes them to separate and reaching the end-point detector in a size-dependent manner, Molecules with larger effective radii will have faster average velocities and shorter elution times. The average elution time (or retention time) of a molecule t is related to its effective radius r, the radius of the capillary R, and the average elution time of the solute t_0. Multiple models have been proposed to relate these parameters, depending on the properties of the molecules or colloids and the ratio between molecule size and capillary radius.[55] The simple linear model has worked well under some conditions to describe the separation of dsDNA.[47] By further relating the radius of DNA to its length L in terms of bp or kbp, a relationship between DNA elution time and DNA length can be established:

$$t = A + B \times L^{0.567} + C \times L^{1.134} \tag{1}$$

where A, B, and C are fitted parameters that are related to the capillary radius, average solvent flow rate, and scaling factor that relates a DNA length in basepairs to its gyration radius.

The simple quadratic model takes both exclusion and hydrodynamic effects into account, allowing for analysis over a wider range of molecule to capillary radius ratios:

$$\frac{t_0}{t} = m = \frac{2\mathrm{r}}{R} + \left(\frac{\mathrm{r}}{R}\right)^2 \tag{2}$$

where m is the relative mobility of the DNA fragment. The elution time of the solvent t_0 can be estimated by the elution time of a small dye molecule. This relationship is used to estimate the effective radius of a separated species.

2.2.2 Cylindrical Illumination Confocal Spectroscopy

Cylindrical Illumination Confocal Spectroscopy (CICS) is a modified confocal spectroscopy platform optimized for single molecule detection (SMD) within a microfluidic channel. We provide a brief overview of the concept here, but refer the reader to reference [53] for a more detailed explanation. A comparison of CICS and traditional confocal SMD is provided in **Fig. 2.2**. Traditional SMD focuses a collimated laser beam to a diffractionlimited spot that is typically much smaller than the dimensions of a microfluidic channel. This mis-match of channel cross section and observation volume limits both the single molecule burst uniformity and single molecule detection efficiency. The result is a decrease in mass detection sensitivity and an increase in signal variation that limits its quantitative accuracy. CICS uses a cylindrical lens to expand the beam in one dimension, creating a laser sheet rather than a laser spot. This sheet can span the entire cross section of a microfluidic channel, so that the entire cross section is incased within the highly uniform detection volume. This allows for near 100% mass detection efficiency and highly uniform fluorescent bursts regardless of the molecular trajectory through the microchannel and observation volume.

2.3 Integrated SML-FSHS platform

The small channel cross-section used for FSHS is well sized to couple with CICS for single molecule detection of separated DNA. We call this integrated platform Single Molecule Free Solution Hydrodynamic Separation (SML-FSHS).[32]

A schematic of the optical components and integration with the microcapillary is shown in **Fig. 2.3**. This system contains one laser diode (OBIS 640-40LX, Coherent Inc.) which emits at 640 nm. The beam was expanded using two doublet spherical lenses SL1 and SL2 (f=19mm and f=75mm, Thorlabs) and a 25 μm pinhole. A cylindrical lens CL (f=150 mm) was used to expand the beam in one dimension and a full mirror FM was used to direct the optical path to focus on the back focal plane of a 100X oil objective (1.3 NA, Olympus, UPlanFLN). The objective also collected the emitted light. A dichroic mirror DM (Semrock, Di01-R635) separated excitation light from emitted light, which then passed through a confocal slit aperture CA (National Aperture) before being passed through an emission filter BP (Semrock, FF01-676/37) and focused with a doublet lens SL5 onto a silicon avalanche photodiode (APD, Excelitas, SPCM-AQR10). Two CMOS cameras were used for focusing and alignment of the capillary lumen. A pellicle beamsplitter PB split a fraction of the optical path before the DM to focus (SL6) on the first camera (cCMOS, Thorlabs), which was used for course alignment and maintaining focus during experiments. The camera after the CA (mCMOS, Thorlabs) was used to align the capillary lumen within the rectangular aperture and only received signal when the removable mirror (RM1) was in place. The detection window of the capillary was mounted on a glass slide, which was held by vacuum to a 3-axis piezo stage (9063-XYZ-PPP, Newport Corp.). The entire footprint of all optical components is confined to a 2 ft by 2 ft benchtop optical breadboard (Thorlabs). A single power supply and control system was built to power the laser, stage, and APD, and was connected to a laptop computer for control of all components.

2.4 Single Molecule Analysis

Photon counts were collected from the APD in 0.1 or 1 ms bins. This raw APD trace was analyzed with a custom computer program to identify single molecule bursts and store particular burst parameters for each identified burst. A screenshot of the MATLAB GUI is shown in **Fig. 2.4**. For single molecule analysis, a thresholding algorithm is used to identify the single molecule bursts. A burst is identified when the photon counts of the raw trace exceed an input threshold value. The burst start and end are determined by when the photon trace crosses the input baseline value. Three data filter algorithms that have previously been implemented in single molecule analysis were also implemented. Unless otherwise noted, these filters were not typically used in our data analysis. Upon identifying a single molecule burst, six parameters were stored for each burst: burst start (time), burst end (time), maximum burst height (photons), time at burst height max, burst width (burst end – burst start), and total burst size (sum of all photons within burst). These burst parameters were used to characterize size and conformation properties at the single molecule level.

To build a single molecule chromatogram, the bursts were counted into larger bins (typically between 0.5 and 10 s, depending on the solute flow rate). These chromatograms were fit to a series of gaussian peaks using OriginPro. The peak center is used as the average retention time, and peak area determines the quantity of molecules present in the peak. This enables absolute quantification in terms of number of molecules for each separated species.

Separation resolution can be calculated in two ways. First, the resolution R between two peaks can be determined simply through comparison of the peak centers and standard deviations:

$$R = \frac{2(t_2 - t_1)}{w_2 + w_1} \tag{3}$$

where t_2 and t_1 are the elution times of each species and w_1 and w_2 are the characteristic widths of each peak. This is commonly either full-width-half-max (FWHM) or 4 standard deviations (95% of peak area). This equation provides a relative measure of separation resolution. Alternatively, one can use a separation model (e.g. equation 1) to translate the characteristic peak width to absolute resolution in terms of bp.

2.5 Experimental Details

All experiments were performed using fused silica capillaries (Polymicro Technologies, Phoenix, AZ) with internal diameters estimated using SEM to be 2.1 and 0.6 μm. The protective polyimide coating was burned from a small region of the capillary to form a viewing window with minimal background fluorescence. The capillary length was measured from the center of the viewing window, which was aligned with the APD focal volume, to the end of the capillary. An injection chamber is designed to hold a 200 μL PCR tube from which both sample and elution buffer are introduced. The capillary is held in place in the solution as compressed nitrogen gas is pumped into the chamber at a constant, controlled pressure to drive the solution into the capillary. Electronic gas pressure regulators and a custom LabView program were used to control the injection pressure and time.

All separations were carried out in 1x TE Buffer (10 mM Tris, 1 mM EDTA, pH 8). Samples were prepared from λ *Hind*III digest (New England BioLabs, Ipswich, MA), a 50bp DNA ladder (New England BioLabs, Ipswich, MA), or a 20 bp DNA ladder (Thermo Scientific, Pittsburg, PA) diluted in this same buffer to the noted concentration and stained with TOTO-3 Iodide (Life Technologies, Grand Island, NY) at an 8bp:dye ratio for at least 1 hour at room temperature prior to injection. Each capillary was filled with buffer, then injected with a small sample plug, and followed by more elution buffer. Photon counts were collected in 1 ms bins from the APD using a custom LabView program. This raw trace can be further binned into larger time intervals (0.5-20 seconds) and analyzed in terms of either bulk fluorescence or single molecule counts.

2.6 Mass Detection Sensitivity and Low Sample Consumption

Single molecule detection with CICS enables high mass detection sensitivity and efficiency. The high mass detection efficiency and burst uniformity is demonstrated in the separation of a 50 bp ladder in a 0.6 μm capillary shown in **Fig. 2.5**. Each fluorescent burst in the raw APD trace in **Fig. 2.5a** represents one molecule flowing through the detection region. Fluorescence of even a single 50 bp fragment is still well above the background. Thresholding analysis and single molecule counting is used to form the single molecule chromatogram shown in **Fig. 2.5b**. The raw single molecule chromatogram (black) is fit with a series of gaussian peaks (red) to determine the total quantity of molecules present in each size peak and to determine the retention time of each peak. Only nine molecules are present in the first separation peak (1.35 kbp), shown in the inset of **Fig. 2.5a**, but with the high mass detection efficiency, even this small quantity is sufficient for identification and separation analysis. This separation was performed with a sample plug <0.3 pL in volume, effectively performing analysis with near-zero sample consumption.

2.7 Wide Dynamic Range and Quantification

Single molecule detection and counting also improves detection sensitivity and quantification accuracy over bulk fluorescence analysis. In **Fig. 2.6**, λ *Hind*III digest is separated in a 2.1 μm diameter capillary. In **Fig. 2.6a** bulk fluorescence analysis, peak intensity decreases with DNA size such that the 100 bp peak is indistinguishable from background. However, by using highly sensitive single molecule detection, the relative brightness of molecules becomes irrelevant for quantification. In the single molecule chromatogram in **Fig. 2.6b**, peak area represents the total quantity of molecules, regardless of size. Gaussian peak fits (red) are used to determine the average retention time and quantify the molecules present of each fragment size. Due to the digestion process, one would expect each fragment size to be at equimolar concentration. With exception to the 0.1 kbp peak, which is slightly underrepresented due to low florescence and staining inefficiency, and the 4.4 kbp peak, which can hybridize to the 23 kbp peak to form the 27 kbp species, the average number of molecules present in each peak is 192 ±16 molecules (**Table 2.1**)

Moreover, this method achieves CE-like resolution over a broader size range within a single run. The same 2.1 μm diameter capillary with a length of 75 cm was used to separate both λ *Hind*III Digest (**Fig. 2.6**) and a 50 bp ladder (**Fig. 2.7a**), revealing that the same experimental conditions can successfully separate fragments as large as 23 vs. 27 kbp and as small as 50 bp vs. 100 bp.

The effect of capillary diameter is demonstrated in **Fig. 2.7** by testing the same 50 bp DNA ladder in both 2.1 μm (**Fig. 2.7a**) and 0.6 μm diameter (**Fig. 2.7b**) capillaries of the same length. The separation resolution of all DNA fragments within the ladder (1.35 kbp to 50 bp) were as much as 2.5 times better in the smaller diameter capillary. However, the smaller capillary diameter has higher flow resistance, requiring higher driving pressures to reach the same average flow velocity. Moreover, larger fragments can be better resolved in a larger diameter capillary.[47, 48, 55, 56] Thus, the capillary radius can be adjusted to increase separation resolution within a particular DNA size range.

2.8 Sizing DNA Fragments and Determining Basepair Resolution

The high separation resolution and sizing capabilities of the SML-FSHS platform was further tested with the separation of a 20bp DNA ladder (**Fig. 2.8a**). The same capillary was used as for **Fig. 2.5**. Gaussian peak fits to the single molecule chromatogram in **Fig. 2.8a** were used to determine the retention time of each fragment size. The model shown in equation 1 that relates DNA length and retention time was fit to the experimental data (**Fig. 2.8b**). The model fits the data well. Resolution in terms of base pairs was calculated using the fitted model and the FWHM of the fitted peaks from **Fig. 2.9** and was assessed to be between 7 and 9 base pairs for the four smallest DNA fragments. Applying the same model fit to the 50bp ladder separated in **Fig. 2.5**, we can see that the model fits with a high level of agreement over a DNA size range spanning at least 2 orders of magnitude (**Fig. 2.10**). FSHS DNA sizing over even wider ranges in a single run has been demonstrated elsewhere.[32, 47, 57]

2.9 Conclusion

This chapter has introduced the integrated Single Molecule Free Solution Hydrodynamic Separation (SML-FSHS) platform for length-based separation and sizing of DNA molecules. We introduced the separation mechanism, CICS single molecule detection, platform integration, and the data analysis methods incorporated in performing and interpreting the SML-FSHS separation data. We then demonstrated the utility of SML-FSHS in separation and sizing of dsDNA fragments by length. We have demonstrated that Single Molecule Hydrodynamic Separation can achieve DNA sizing resolution comparable to CE over a wider dynamic range with improved sensitivity and quantification. The application of CICS detection allows for higher mass detection efficiency and sensitivity, while the separation scheme eliminates the need for capillary preconditioning and the use of either polymeric gel matrices or mass tags to alter the relative DNA mobility.

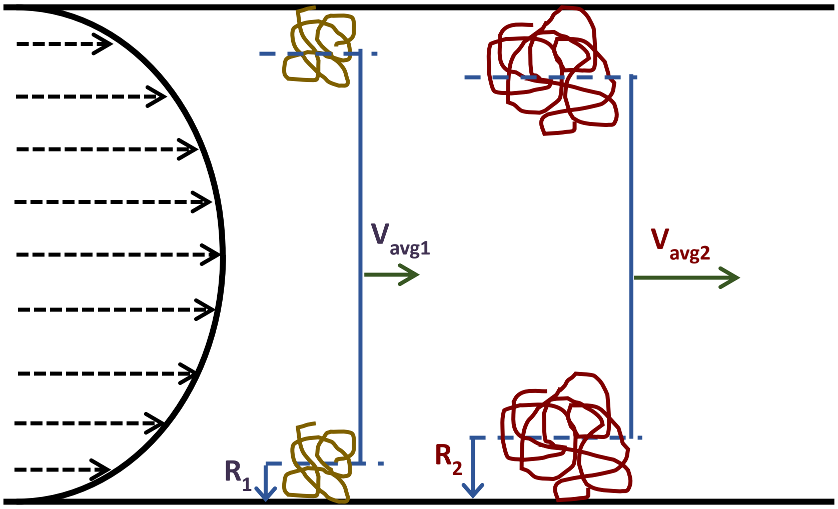
V_avg1
V_avg2
R_1
R_2

Figure 2.1. Schematic diagram of hydrodynamic separation principle

Adapted with permission from [48]. Copyright 2016 American Chemical Society.

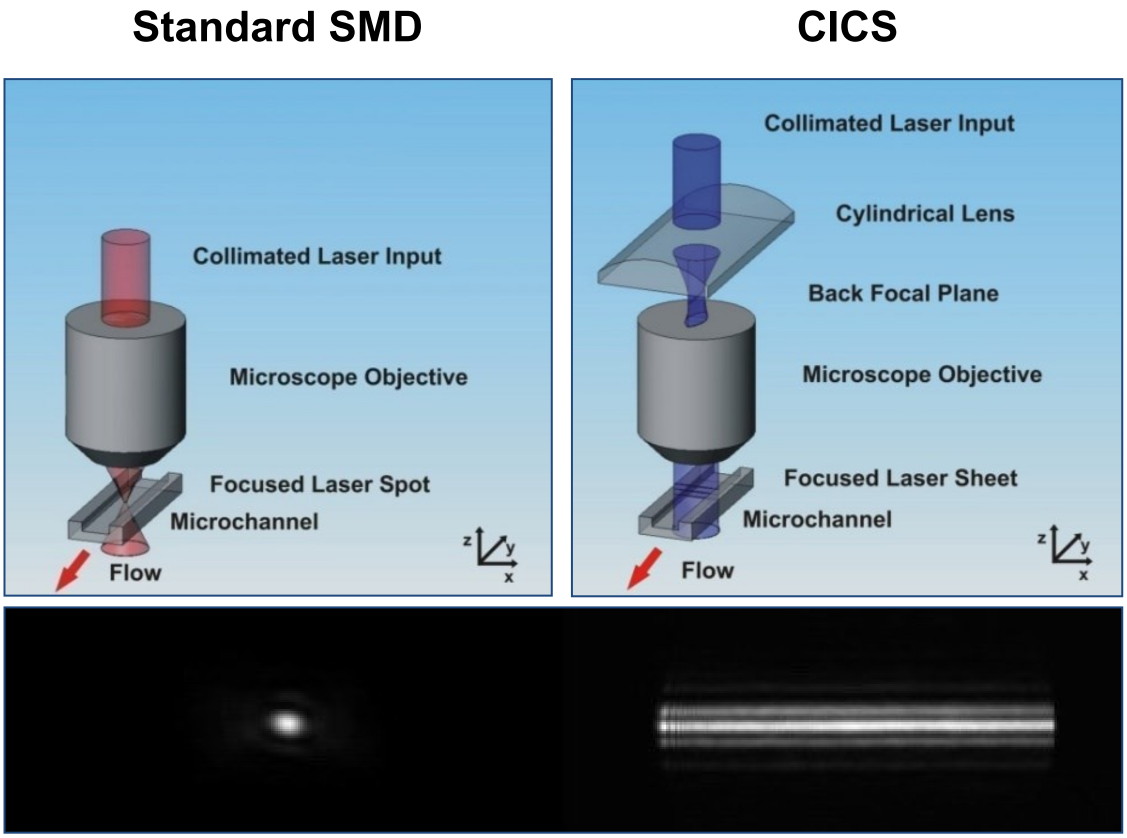
Standard SMD
CICS
Collimated Laser Input
Microscope Objective
Focused Laser Spot
Microchannel
Flow
z
y
x
Collimated Laser Input
Cylindrical Lens
Back Focal Plane
Microscope Objective
Focused Laser Sheet
Microchannel
Flow
z
y
x

Figure 2.2. Comparison of standard confocal SMD platforms with CICS sheet-like illumination

Adapted from reference [53] with permission.

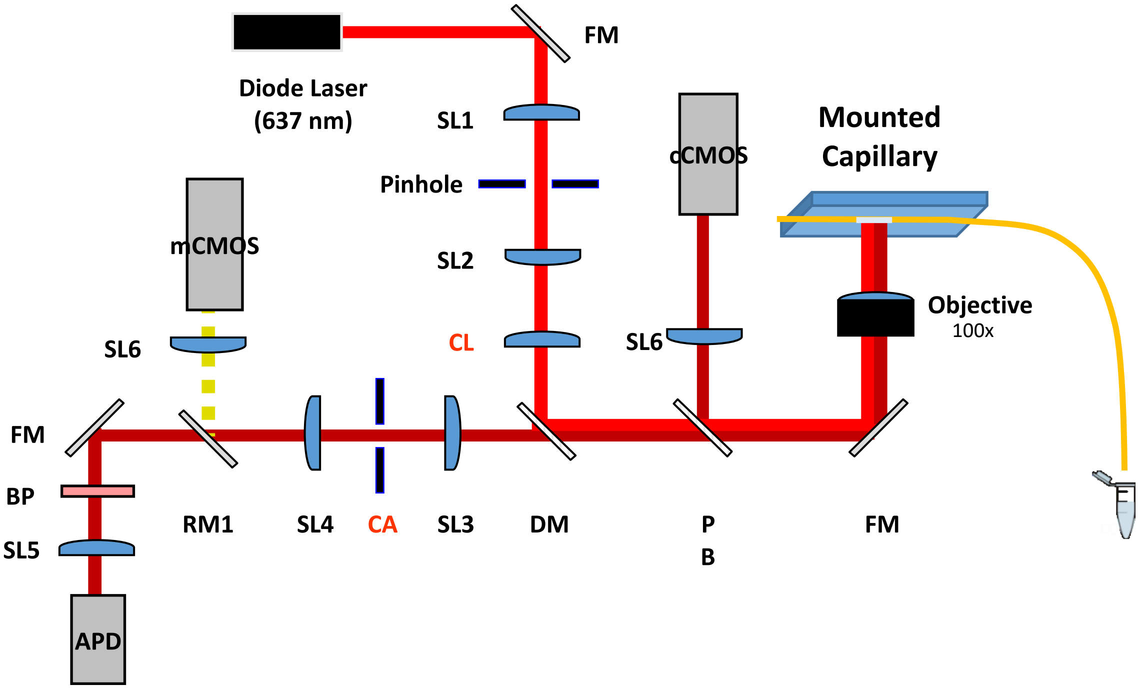
Diode Laser
(637 nm)
FM
SL1
Pinhole
SL2
CL
mCMOS
SL6
cCMOS
Mounted
Capillary
Objective
100x
SL6
FM
BP
SL5
APD
RM1
SL4
CA
SL3
DM
P
B
FM

Figure 2.3. Schematic of the SML-FSHS platform

Schematic of the CICS optical detection platform with the cylindrical lens (CL) providing the beam expansion over the burned viewing window of the mounted separation capillary. Adapted with permission from [48]. Copyright 2016 American Chemical Society.

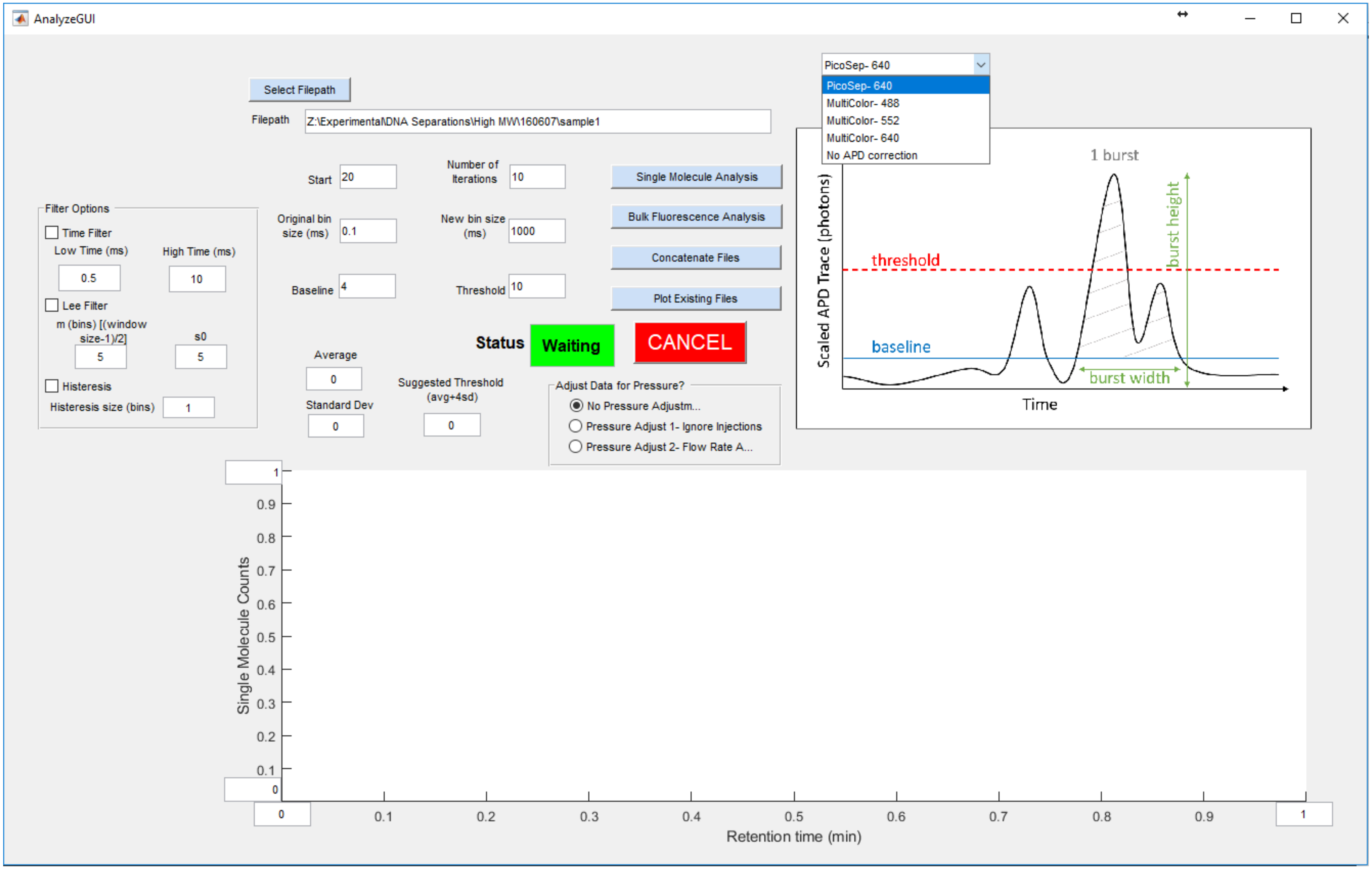
AnalyzeGUI

Filepath: Z:\Experimental\DNA Separations\High MW\160607\sample1

Start: 20

Number of Iterations: 10

Original bin size (ms): 0.1

New bin size (ms): 1000

Baseline: 4

Threshold: 10

Average: 0

Standard Dev: 0

Suggested Threshold (avg+4sd): 0

Status: Waiting

Filter Options

☐ Time Filter

Low Time (ms): 0.5

High Time (ms): 10

☐ Lee Filter

m (bins) [(window size-1)/2]: 5

s0: 5

☐ Histeresis

Histeresis size (bins): 1

Adjust Data for Pressure?

● No Pressure Adjustm...

○ Pressure Adjust 1- Ignore Injections

○ Pressure Adjust 2- Flow Rate A...

PicoSep- 640

Figure 2.4. Screen shot of data analysis MATLAB GUI

A GUI was written in MATLAB to identify and store single molecule burst characteristics from the raw APD data. The GUI is user friendly and enables modifications of important parameters between analysis, such as selecting the correct APD correction factor for the APD, choosing the file location and length of data trace, and changing the thresholding and filtering parameters.

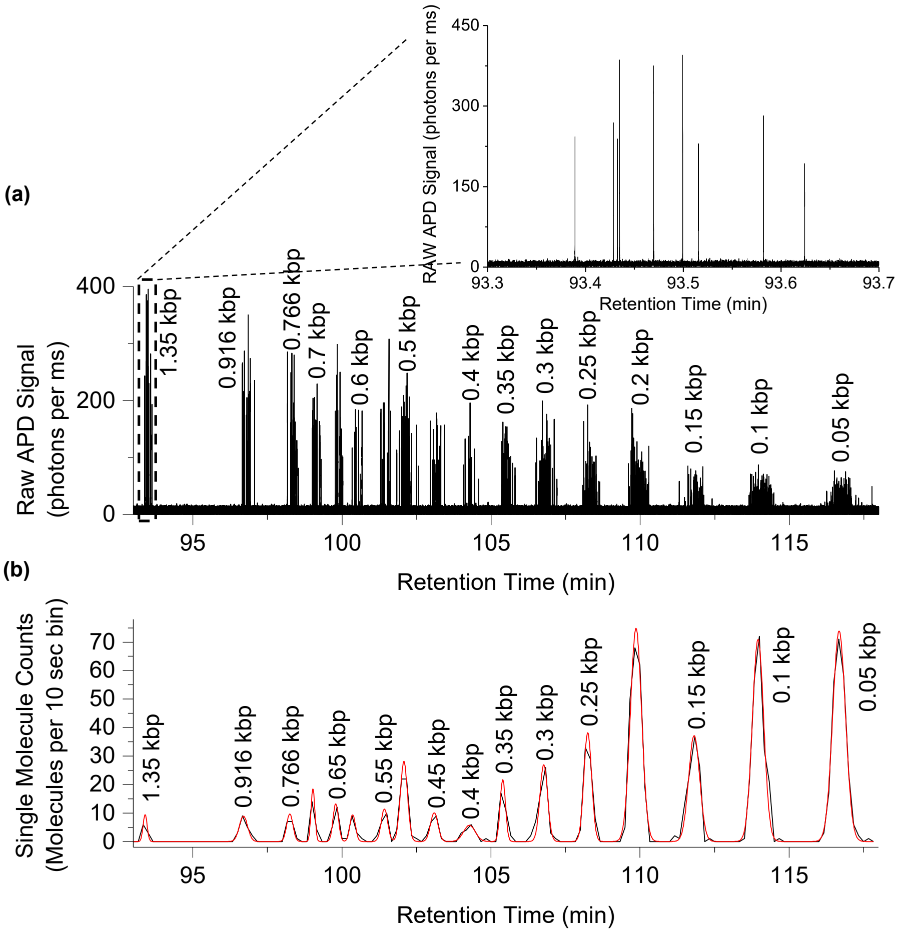
(a)
RAW APD Signal (photons per ms)
450
300
150
0
93.3
93.4
93.5
93.6
93.7
Retention Time (min)
Raw APD Signal (photons per ms)
400
200
0
1.35 kbp
0.916 kbp
0.766 kbp
0.7 kbp
0.6 kbp
0.5 kbp
0.4 kbp
0.35 kbp
0.3 kbp
0.25 kbp
0.2 kbp
0.15 kbp
0.1 kbp
0.05 kbp
95
100
105
110
115
Retention Time (min)
(b)
Single Molecule Counts (Molecules per 10 sec bin)
70
60
50
40
30
20
10
0
1.35 kbp
0.916 kbp
0.766 kbp
0.65 kbp
0.55 kbp
0.45 kbp
0.4 kbp
0.35 kbp
0.3 kbp
0.25 kbp
0.15 kbp
0.1 kbp
0.05 kbp
95
100
105
110
115
Retention Time (min)

Figure 2.5. Raw APD trace and single molecule chromatogram of 50bp DNA ladder

Separation of <0.3 pL of 1 ng/μL of a 50 bp DNA ladder was performed in a 0.6 μm diameter capillary with a 55 cm length at 490 psi. A thresholding algorithm was applied to the raw APD trace shown in (a) to generate (b) the single molecule counting trace. The inset of (a) shows the 9 detected molecules of the largest fragment size. Adapted with permission from [48]. Copyright 2016 American Chemical Society.

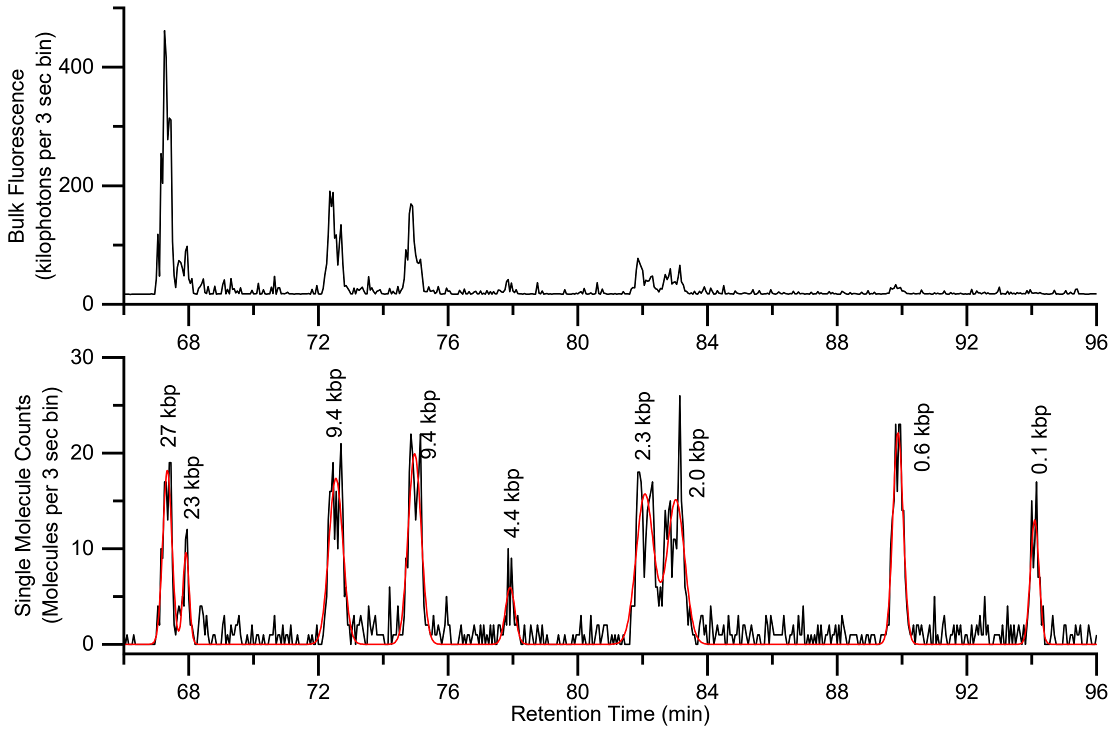
Bulk Fluorescence
(kilophotons per 3 sec bin)
0
200
400
68
72
76
80
84
88
92
96
Single Molecule Counts
(Molecules per 3 sec bin)
0
10
20
30
27 kbp
23 kbp
9.4 kbp
9.4 kbp
4.4 kbp
2.3 kbp
2.0 kbp
0.6 kbp
0.1 kbp
68
72
76
80
84
88
92
96
Retention Time (min)

Figure 2.6. Single molecule and bulk fluorescence chromatograms of wide dynamic range DNA separation

Separation of a 2 pL plug of ~330 yoctomoles of λ *Hind*III digest in a 2 μm diameter capillary with a 75 cm length at 100 psi with (a) bulk fluorescence analysis and (b) single molecule counting analysis. The raw data is shown in black. Gaussian peak fits are shown in red. **Table 2.1** shows the molecule counts and retention times generated from this gaussian fitting. Reprinted from ref [33].

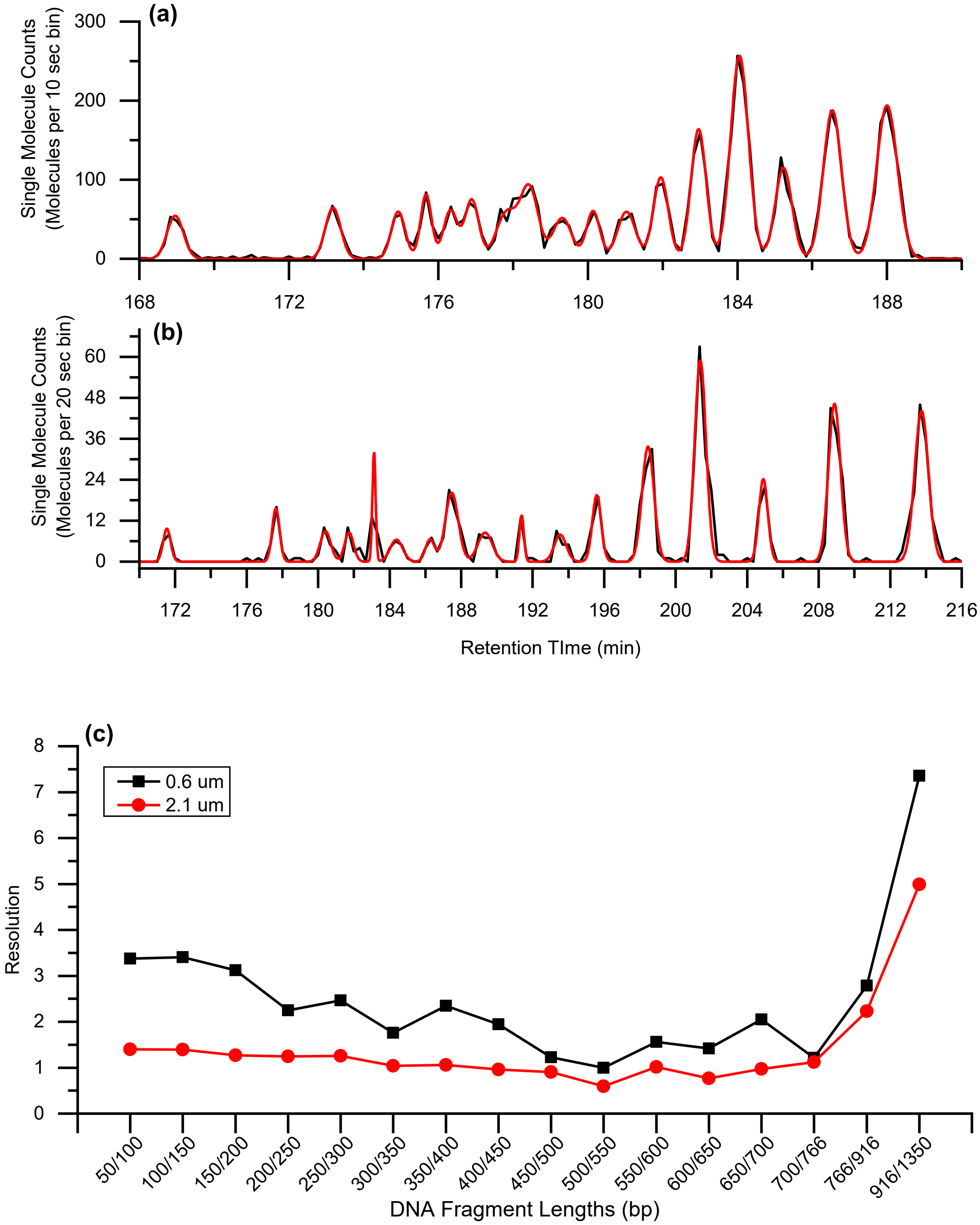
(a)
Single Molecule Counts
(Molecules per 10 sec bin)
0
100
200
300
168
172
176
180
184
188
(b)
Single Molecule Counts
(Molecules per 20 sec bin)
0
12
24
36
48
60
172
176
180
184
188
192
196
200
204
208
212
216
Retention TIme (min)
(c)
0.6 um
2.1 um
Resolution
0
1
2
3
4
5
6
7
8
50/100
100/150
150/200
200/250
250/300
300/350
350/400
400/450
450/500
500/550
550/600
600/650
650/700
700/766
766/916
916/1350
DNA Fragment Lengths (bp)

Figure 2.7. Comparison of separations in 0.6 and 2.1 μm diameter capillaries

A 50bp-ladder of 1 ng/μL is separated in a (a) a 2.1 μm diameter capillary at 50 psi and (b) a 600 nm diameter capillary at 490 psi. Both capillary lengths are 75 cm. (c) Peak-to-peak resolution comparison between the two capillary separations. Adapted from ref [33].

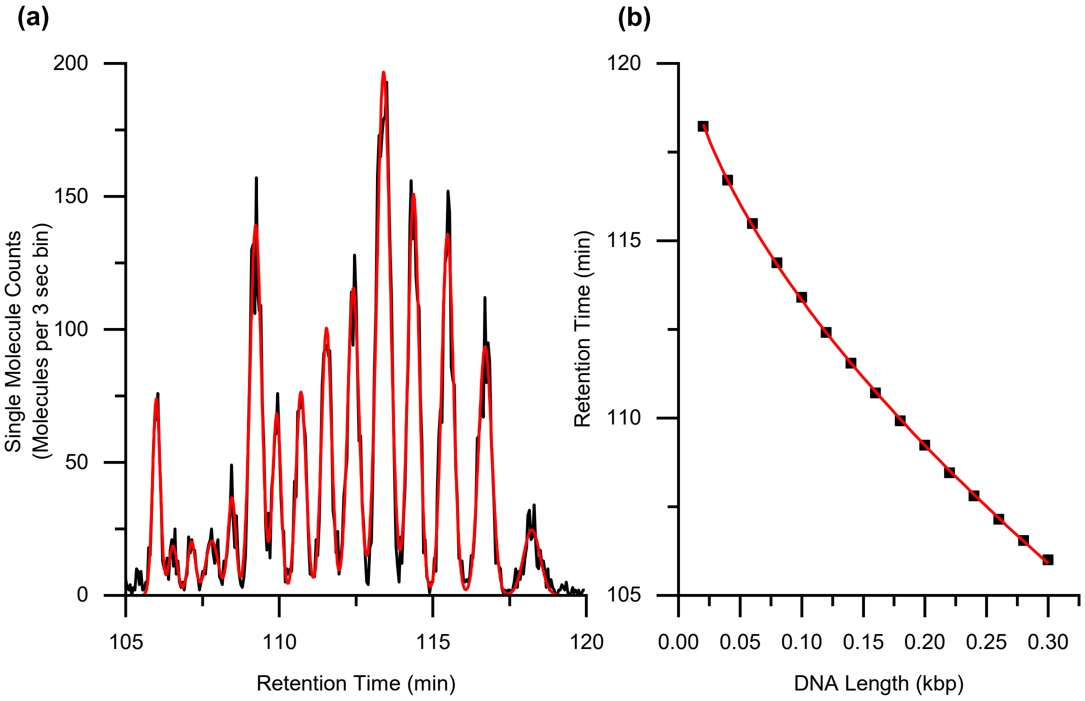
(a)
200
150
100
50
0
Single Molecule Counts
(Molecules per 3 sec bin)
105
110
115
120
Retention Time (min)
(b)
120
115
110
105
Retention Time (min)
0.00
0.05
0.10
0.15
0.20
0.25
0.30
DNA Length (kbp)

Figure 2.8. Fitting 20bp ladder separation to separation model

(a) Separation of a 20 bp DNA ladder (20ng/μL) at 490 psi is demonstrated in the same 0.6 μm capillary used in **Fig. 2.5**. The capillary length is 55 cm. (b) The elution time of each peak is fitted with the model that relates retention time t to DNA length L in kbp. Reprinted from ref [33].

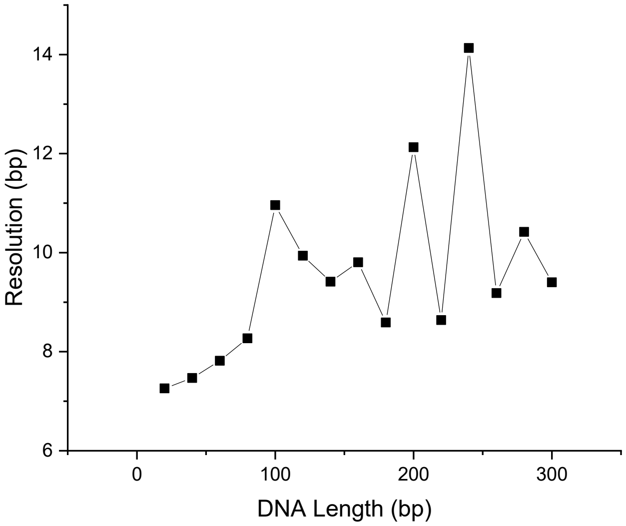
Resolution (bp)
14
12
10
8
6
0
100
200
300
DNA Length (bp)

Figure 2.9. Separation resolution for 20bp ladder separation

The fitting model was used to calculate the separation resolution at FWHM for DNA lengths ranging from 20bp to 300 bp. Under 100bp, the resolution is less than 10bp.

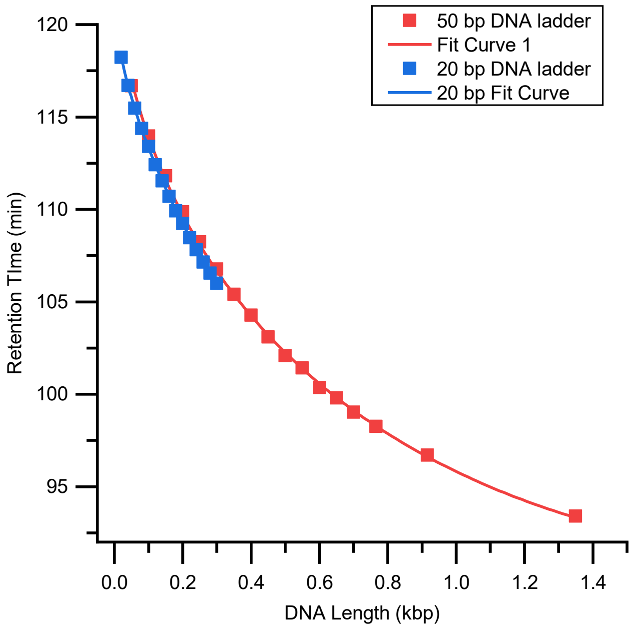
50 bp DNA ladder
Fit Curve 1
20 bp DNA ladder
20 bp Fit Curve
Retention TIme (min)
120
115
110
105
100
95
0.0
0.2
0.4
0.6
0.8
1.0
1.2
1.4
DNA Length (kbp)

Figure 2.10. Comparison of the separation model fitted to separations of 20bp and 50bp ladders

The same capillary was used to separate a 20 bp ladder (blue, **Fig. 2.9**) and 50bp ladder (red, **Fig. 2.5**) on different days. The separation model shows high agreement for DNA sizing over at least 2 orders of magnitude.

DNA Length (kbp)	Molecule Counts	Retention time (min)
*0.1	87	94.9
0.6	174	90.6
2	204	83.5
2.3	213	82.6
*4.4	44	78.6
6.6	200	75.6
9.4	188	73.2
**23	47	68.6
**27	127	68.1
23 + 27	174	--
average	192	--
stdev	16	--

Table 2.1: Quantification of mobility and molecule counts from λ *Hind*III digest separation

The separation chromatogram shown in Fig. 2.6b was fit with a series of gaussian peaks. The peak area was used to determine the number of molecules present in each fragment size. The peak center is used to determine the average retention time of each fragment size. The average and standard deviation of the molecule counts shows very high quantification capabilities. *0.1 and 4.4 kbp fragments were not included in the calculated molecular counts average due to underrepresentation due to staining inefficiencies and hybridization. **23 and 27 kbp fragments were not included in the molecule counts average because of 4.4kbp hybridization. Instead, these fragment species were added together for the most accurate representation.

Chapter 3

3. Analysis of Global DNA Conformational Changes

3.1 Background

In the previous chapter, we introduced our SML-FSHS platform and demonstrated its utility in separating and sizing DNA molecules by length. However, this is only one of the many properties of DNA molecules of potential interest and utility to researchers and clinicians (see Chapter 1). Moreover, single molecule detection was largely utilized as digital counting tool to increase detection sensitivity and quantification capabilities. While useful, this does not capture the richness and utility of the having individual burst signatures for each molecule to extract layered analysis of molecular properties and diversity. In this chapter, we aim to both expand the DNA assessment modalities of the integrated platform and further realize the capabilities of the single molecule detection to provide layered analysis of global DNA fragment conformations in free solution.[48]

Limited tools exist that are capable of monitoring nucleic acid conformations, fluctuations, and distributions in free solution environments. While electrophoretic methods can be used, electrophoretic mobility is a function of multiple underlying factors, making it difficult to relate electrophoretic mobility changes directly and quantitatively to size and conformational changes.[58] Crystallography has been used to determine precise molecular conformation, but the crystallization process itself can influence the observed conformation, often requires strict solution conditions, is complicated and time consuming, and only provides a population average conformation.[59, 60] Fluorescence Correlation Spectroscopy (FCS) provides an alternative method for detecting molecular concentration, hydrodynamic size, and mass change due to binding but the, size resolution is limited, and, like crystallography, FCS provides only a population average, making individual discrimination of multiple species difficult.[61] Single molecule fluorescence resonance energy transfer (smFRET) has emerged as a useful tool for analyzing population distributions of DNA conformational changes. However, design of the probes and protocol is nontrivial and often requires tethering to a surface, which can introduce discrepancies from a free solution environment, and the size measurement range is generally limited to ~1-10nm, making analysis of larger-scale conformational changes difficult.[62]

We propose that our SML-FSHS platform could serve as a useful tool to analyze larger-scale size and shape changes of DNA molecules in free solution. Whereas hydrodynamic separation can determine the average size of a molecule based on peak retention time, single molecule spectroscopy provides the opportunity to look at individual molecules within that ensemble. By examining the size and shape of each single molecule fluorescent burst, it is possible to determine molecular information regarding individual DNA conformations and distributions. The combination of these methods allows layered information regarding ensemble conformations and their underlying single molecule distributions. The high sensitivity and wide dynamic range of hydrodynamic separation and single molecule spectroscopy further enables concurrent analysis of rare and abundant species within a single sample.

In this chapter, SML-FSHS is used to probe global DNA conformational changes. Molecular properties are determined by layered analysis of single molecule fluorescent burst characteristics and hydrodynamic mobilities. First, we analyze single molecule fluorescent bursts to determine DNA conformation and define DNA packing density. We then show that DNA packing density and hydrodynamic mobility are related by investigating the effects of DNA topology and buffer monovalent and divalent salt concentration on DNA packing. We then utilize this analysis to investigate discrete, large-scale structural changes associated with trivalent cation-induced DNA condensation. Finally, we utilize SML-FSHS multiparametric analysis to simultaneously measure the effective radius, DNA content, and DNA packing density within the condensed DNA globules.

3.2 Experimental Details

3.2.1 Buffer Preparation

EACA (6-Aminocaproic acid) and Bis-tris were purchased from Sigma and dissolved in water to 500 mM stock concentrations. These stock solutions were used to generate the base 20 mM EACA/Bis-tris (EB) buffer at a final concentration of 10 mM EACA and 10 mM Bis-tris. Stock solutions of 5 M NaCl and 1 M $MgCl_2$ were used to create buffers with added salt. Spermidine trihydrochloride (SPD, Sigma-Aldrich) was dissolved in deionized water to a stock concentration of 500 mM and stored at -20 °C.

3.2.2 Sample Preparation

Lambda DNA, *Hind*III digested Lambda DNA, 1 kb DNA Ladder, and Supercoiled DNA Ladder (all from New England Biolabs, Inc.) were used as double stranded DNA samples. Staining was performed at 5 or 10 ng/μL total dsDNA concentration and 1 μM TOTO-3 Iodide (Life Technologies) for at least 1 hour in the dark. Single stranded DNA was purchased from IDT. Labeled oligos were ordered with either Alexa 647 or Cy5 covalently attached. The covalently labeled 25 bp DNA strand was synthesized and hybridized by IDT. Free Alexa was purchased as dry Alexa Fluor 647 NHS Ester (Life Technologies) and diluted in water. For a more detailed description of monovalent salt and topology separations, please refer to reference [48].

For SPD-condensation, the samples were stained at 10 ng/μL total dsDNA concentration and 1 μM TOTO-3 Iodide. After staining in the dark for at least one hour, the stained samples were further diluted to 5 ng/μL in 20 mM EB buffer (free-coiled) or 20 mM EB buffer + 100 μM SPD (condensed) for SML-FSHS analysis. The same staining protocol was followed for *Hind*III digested λ DNA (New England Biolabs).

3.2.3 Separations

All separations were performed at room temperature in fused silica capillaries purchased from PolyMicro (Molex), with inner diameters ranging from 1.6 μm (as measured by SEM) to 10 μm. Capillaries were cut to length and a short section of the polyimide coating was burned from the capillary to form a detection window. The capillary length L was measured as the distance between the capillary inlet and the center of the detection window. For a more detailed description of monovalent salt and topology separations, please refer to reference [48].

The SPD-condensation separations were performed in a 5 μm nominal inner diameter fused silica capillary with an effective length of 100 cm. The running buffer for each separation was chosen to match the composition of the sample buffer (e.g. 1× EB or 1× EB + 100 μm SPD). After the capillary was filled with the running buffer, sample plugs were injected for 10 s at 50 psi (free coiled) or 100 psi (condensed), and separation occurred at

400 psi. To minimize DNA-wall interactions with the addition of SPD, the capillary with 20 mM EB + 0.5% polyvinylpyrrolidone (PVP, molecular weight 360,000, Sigma-Aldrich) for about 1 hour prior to analysis of the SPD-condensed DNA samples. This single capillary treatment was sufficient for at least a day of use, with no obvious changes to the separation chromatogram observed over hours of use.

The same SML-FSHS platform was used as described in Section 2.3. Pressure was provided by compressed argon gas through an electronic dual valve pressure controller (Alicat Scientific) for differential pressures up to 500 psi. LabView software was designed to control and record the pressure provided by the valves for precise timing and pressure control. Photon counts were collected from the APD in 0.1 or 1 ms bins using a DAQ card (National Instruments) and software written in LabView (National Instruments). Labview software was also used to control the laser power (8mW) and the flipper mount that positioned the removable mirror (Thorlabs).

3.2.4 Relative Mobility Analysis

The raw APD traces were corrected for color and quantum yield before performing single molecule burst analysis. A threshold is used to identify a single molecule bursts, and a baseline is used to identify the beginning and end of each burst. A hysteresis value of 1 was also used to help remove edge effects on the single molecule burst determination for the SPD-concentration analysis.[63] For single molecule counting, the single molecule bursts were then summed into larger time bins to create the single molecule chromatograms against the retention time. Typically, the peaks were then fit to a series of gaussian peaks in OriginPro (OriginLab) to compute the average retention time (peak center, t_i), quantify the number of molecules (peak areas) and compute the separation resolution (using the peak standard deviations σ). The width of each fragment peak was calculated as 4 times the standard deviation (σ) of the fitted Gaussian peak and was used to determine the retention time range for each fragment size. The peak width is reported as error bars in plots of relative mobility. The relative mobility *m* of species *i* was calculated from the retention time of the free alexa dye marker:

$$m_i = \frac{v_i}{v_{dye}} = \frac{t_{dye}}{t_i} \tag{1}$$

where v_i and t_i are the average velocity and elution time of species i, respectively, and v_{dye} and t_{dye} are the average velocity and elution time of the free dye marker. For the DNA condensation study, we found that gaussian peaks did not well fit either the free-coiled or the condensed forms of the Lambda DNA, likely due to both nonuniformity in the samples as well as non-optimal conditions for the separation. For this reason, we chose to use a bigaussian fit to better capture the observed shape of the elution peaks with σ_1 being the standard deviation of the left side of the curve and σ_2 the standard deviation of the right side.

Relative mobility was also used to calculate the effective radius (r_i) of the eluted species:

$$m_i = 1 + \frac{2r_i}{R} + \left(\frac{r_i}{R}\right)^2 \tag{2}$$

where *R* is the radius of the inner lumen of the capillary.

3.2.5 Fluorescent Burst Analysis

The start and end for each separated species *i* were defined as the peak center ± two standard deviations:

$$t_{i-s} = t_i - 2 * \sigma_1 \tag{3}$$

$$t_{i-e} = t_i + 2 * \sigma_2 \tag{4}$$

These peak start and end times were normalized with the dye marker average elution time as in equation 1 above to find the relative mobility start and end for each species. For burst parameter analysis, the single molecule burst height, width, size, and retention time were stored for each single molecule burst. The ratio of the burst height h to burst width w was called the packing density PD and was used as a measure of the compaction of each single molecule burst:

$$PD = \frac{h}{w} \tag{5}$$

Single molecule bursts corresponding to a single species were defined by the chromatogram start and end times in equations 3 and 4**Error! Reference source not found.Error! Reference source not found.**. Any bursts detected between the start and end time points were considered a single species. For the topology and monovalaent and divalent salt studies, the mean packing density of each fragment size was calculated by averaging the packing densities of all single molecule bursts of molecules identified as that fragment size. For the SPD-condensation study, histograms of burst height and packing density for each species were plotted separately and fit to a lognormal distribution. The geometric mean (median) was used for comparison between separate species and between repeated experiments.

3.3 Direct Visualization of DNA Conformation via Single Molecule Fluorescence

The single molecule fluorescent bursts can be analyzed to give layered information regarding molecular distributions and provide insight into the properties of individual DNA molecules. For example, burst size or height can be used to determine the size of a DNA molecule[4] or the DNA mass content within a polymer/DNA complex[28]. By further analyzing the burst shapes[64], we are able to directly visualize DNA conformation while passing through the 1 μm long detection region. **Fig. 3.1** shows representative single molecule bursts arising from 23 kb DNA fragments in a separation of λ *Hind*III digest. The bursts display diverse shapes despite being generated by identical 23 kb DNA fragments. Highly condensed DNA molecules (**Fig. 3.1**, peak 4) show narrow burst widths and tall burst heights. Conversely, highly stretched or elongated molecules (**Fig. 3.1**, peak 1) show wide burst widths and short burst heights.

To quantify these conformational differences, we developed a metric called packing density, calculated as the ratio of burst height (photons per 0.1 ms bin) to burst width (ms). Condensed molecules result in high packing densities while elongated molecules result in low packing densities. When the single molecule bursts of all DNA corresponding to a single chromatogram peak are analyzed, a wide distribution of packing densities can be seen (**Fig. 3.2**). Furthermore, no obvious correlation is seen between packing density and retention time (i.e. temporal position within the peak). This diversity of burst shapes and lack of correlation between packing density and retention time imply that the DNA is likely in dynamic fluctuation between different conformations rather than fixed in a single conformation. These fluctuations are thermodynamically driven by molecular properties such as length and stiffness and separation conditions such as buffer properties and shear rate. A mean packing density for a single fragment size is found by taking the average packing density of all of the molecules identified as a single fragment size. Analysis of repeated separations demonstrate less than 6% variation in mean packing density for a single fragment size between three separation experiments (**Fig. 3.3** and **Table 3.1**).

3.4 Monitoring Perturbations on DNA Conformation via Mobility Shifts.

Perturbations in buffer ionic strength affect DNA packing densities, which are then reflected as changes in the relative mobility. In **Fig. 3.4a**, DNA separations were performed on λ *Hind*III digested DNA using a 1.6 μm ID capillary and either a low ionic strength 20 mM

EB elution buffer (top) or a high ionic strength 20 mM EB elution buffer with 25 mM NaCl added (bottom). The chromatograms are plotted as a function of relative mobility, which was calculated by normalizing retention time to the reference Alexa dye. In the low ionic strength buffer, the short DNA peaks (<0.6 kb) are well resolved while the long DNA peaks (>4.4 kb) are closely spaced. The 48 kb and 23 kb peaks cannot be individually resolved and appear as a single broad peak. However, when ionic strength is increased by the addition of 25 mM NaCl, the long DNA peaks (>4.4 kb) all become well resolved while the short DNA peaks (<0.1 kb) become closely spaced and unresolvable. Increasing the ionic strength creates perturbations in DNA conformation that affect large DNA quite differently than small DNA.

Single molecule burst analysis further supports the conclusions drawn from the relative mobility shifts. The single molecule chromatogram was used to identify the fluorescent bursts belonging to each fragment size in order to calculate the average packing density of each DNA fragment. In **Fig. 3.4b**, the change in DNA packing density due to 25 mM NaCl salt perturbation is plotted against the change in relative mobility. A strong correlation is seen between changes in packing density and relative mobility, indicating that the two measures are indeed related. The greater the change in packing density (i.e. the tighter the DNA condenses), the faster the DNA travels in high salt relative to low salt. Interestingly, we note that if the DNA undergoes no change in packing density, it travels slower in high salt than low salt. This suggests that conformational changes alone do not account for this shift in relative mobility, and factors such as spatial distribution and flow profile may be affected as well.

3.5 Effect of DNA Topology on Packing Density and Relative Mobility

To verify this analysis, we compared the packing densities and relative mobilities of DNA molecules with known conformational differences: supercoiled and linear DNA (**Fig. 3.5**). The supercoiled structure causes a DNA molecule to assume a more compacted conformation than a linear DNA molecule of the same length (bp) and under the same ionic strength buffer conditions. As expected, supercoiled DNA molecule have higher mean packing densities than the linear molecules of the same length (**Fig. 3.5**a). Relative mobility is also affected by the topology of the DNA fragments (**Fig. 3.5b**), verifying our assertion the both packing density and relative mobility can assess DNA conformational changes. The ratiometric plot of supercoiled to linear DNA also displays a positive correlation between mean relative mobility and mean packing density (**Fig. 3.5c**), in agreement with the salt-induced ratiometric analysis (**Fig. 3.4b**).

3.6 Effects of Monovalent and Divalent Cations on Relative Mobility

To measure a broader range of DNA conformation perturbations, we tested the effects of a range of monovalent (sodium) and divalent (magnesium) cation concentrations on relative mobility and packing density. Separations were performed on double stranded (**Fig. 3.6a**) and single stranded DNA (**Fig. 3.6b**) using the low ionic strength 20 mM EB buffer[65] with various amounts of added NaCl and $MgCl_2$. Increasing salt concentration generally resulted in decreasing relative mobilities for most ssDNA and dsDNA species. These cations interact with the DNA's negatively charged backbone to decrease electrostatic repulsion between nucleotides, reducing the effective radius of the DNA fragments and decreasing relative mobility. This is also supported by the higher average packing density displayed by the double stranded DNA fragments in high ionic strength buffer compared to low ionic strength buffer (**Fig. 3.7b** and **d**). Previous studies have further shown that the persistence length of both single stranded[66] and double stranded DNA[67] decreases with higher salt concentration. Moreover, even at the same ionic strength, magnesium cations had a greater effect on relative mobility than sodium cations. Magnesium has a higher affinity for DNA than sodium and results in a greater reduction in persistence length than an ionic strength equivalent concentration of sodium.[66-68]

In **Fig. 3.6**, all the DNA fragments exhibited a decrease in relative mobility with increased salt except for the large 23 kbp dsDNA fragment which behaved in the opposite manner. The average packing densities (**Fig. 3.7b**) also display opposing trends for large DNA fragments (23 and 48 kbp) compared to the rest of the smaller fragments. We attribute this behavior to the size-dependent effects of shear and weak confinement on the relatively compliant DNA molecules. Molecules with larger effective radii experience a larger velocity gradient, and thus shear gradient, across the molecule. As a result, the larger molecules begin to elongate along the capillary length.[69] This molecular deformation also results in a larger-than-anticipated depletion region near the capillary walls.[70-74] The crossover size at which large DNA and small DNA begin behaving differently appears to be the same (< 15 kbp) in both the packing density and relative mobility plots (**Fig. 3.7**), suggesting that both measures are sensitive to perturbations in DNA conformation. Interestingly, the topology-induced crossover size between supercoiled and linear DNA appears to be much smaller (< 5 kbp) than the salt-induced crossover size (**Fig. 3.5**), which could be due to differences in polymer properties between linear and supercoiled DNA, such as flexibility and elasticity, that affect the molecules' responses to shear.

The results shown in Figures 2 and 3 were performed in a 1.6 μm ID capillary, but similar trends were also observed in 5 μm and 10 μm ID capillaries (**Fig. 3.8**). One notable observation is that the crossover size, where increasing salt concentration leads to increasing relative mobility, increases with increasing capillary radius. Thus, it is not the absolute DNA size and compliance that results in increased mobility for large DNAs, but its size relative to the capillary diameter and compliance that is important.

3.7 Monitoring Discrete Large-Scale DNA Conformational Changes

The work presented thus far has focused on detection of relatively small, gradual shifts in DNA conformation. In this section, we expand our analytical capabilities to quantitatively characterize large-scale discrete structural transitions in DNA molecule conformations, using polycation-induced DNA condensation as a model system. In free solution, long DNA molecules typically exist in a free coiled state. The addition of relatively low concentrations of polycations, however, can induce a discrete size and volume change into highly condensed globules or torroids.[75] For this work, we utilize spermidine, a trivalent amine, to condense large lambda DNA molecules (48.6 kbp).

In **Fig. 3.9**, we show the single molecule chromatograms of the fluorescently stained lambda DNA separated in a 5 μm inner diameter capillary in (**a**) a low salt buffer (free-coiled state) and (**b**) with the addition of 100 μM of SPD. (condensed). The single molecule chromatogram of a free-coiled *Hind*III digested lambda DNA ladder is shown for size comparison (**Fig. 3.9c**). Single molecule counting is advantageous over bulk fluorescence detection due to increased sensitivity and quantification accuracy that is independent of any length- or conformation-related changes to fluorescence intensity (**Fig. 3.10**). The raw data (black) was fit (color) with a series of bigaussian (**a** and **b**) or gaussian (**c**) peaks. The peak centers define the average species mobility. Though the larger diameter capillary has inferior separation resolution compared to what we have demonstrated previously in smaller capillaries, the larger cross section more easily accommodates and facilitates sizing of the larger 48.5 kbp DNA molecules, enables faster flow rates for greatly accelerated separation speed (< 8 minutes), and utilizes larger sample plug volumes to enable analysis of more molecules per sample. Despite the low resolution, the separation chromatograms are highly repeatable (**Fig. 3.11**). The SPD-condensed lambda DNA have a significantly decreased mobility, indicating a substantial change in the effective radius. Indeed, the mobility of the SPD-condensed Lambda DNA molecules is comparable to free-coiled 600 bp DNA fragments (1.07 for condensed DNA in Figure 6b, and 1.06 for free-coiled 0.564 kbp DNA fragment in Figure 6c). The 600 kbp fragments are nearly 100-fold shorter than full length lambda DNA molecules and over 1000-fold smaller in average free-coiled volume.[47] In fact, we can use the hydrodynamic mobility of the SPD-condensed species to estimate its effective radius (Section 3.2.4, equation 2) ~80 nm. This size estimate aligns well with TEM measurements of SPD-condensed DNA globules (40 nm – 100 nm).[76-78]

3.8 Combinatorial Analysis to Resolve Size, Conformation, and DNA Content

Comparison of the single molecule chromatograms in **Fig. 3.9b** and **c** illustrates that relative mobility (i.e. effective hydrodynamic radius) is a function of both DNA length and DNA conformation. It is also clear that without prior knowledge of the sample content, relative mobility alone cannot distinguish freely coiled short DNA fragments (such as those produced through digestion or sample degradation) from condensed high molecular weight DNA globules. However, single molecule burst analysis can be used to further distinguish the physical properties of each of these DNA species. As in **Fig. 3.12a**, burst parameters such as burst size (total burst area), burst height, burst width, and packing density (burst height/width) can be used to extract information about molecule size and shape as it crosses the detection window.[4, 28, 48] Here, we focus on burst size to indicate total DNA content and packing density to indicate species shape.

The fitted chromatograms (**Fig 3.9**) were used to define the single molecule bursts belonging to a single species. All bursts located within 2 standard deviations of the peak center (shaded regions) were grouped as a single species and subjected for further single molecule burst analysis. More than 900 single molecule bursts were present within each defined subpopulation (**Fig. 3.12b**, **Table 3.2**). Within each of these populations, a wide distribution of both burst size (**Fig. 3.12c**) and packing density (**Fig. 3.12d**) was observed. Multiple factors may contribute to the source of this variation: non-uniform illumination in the z-dimension of the 5 μm capillary, the parabolic flow profile that results in non-uniform dwell times in the observation volume, and diversity within each sub-population (e.g. different conformations of free-coiled DNA and diversity in size and number of DNA in the condensed globules). These multiplicative effects result in the lognormal distributions observed within each species.[28, 79] However, these distributions were extremely consistent between repeated separations of the same samples (**Fig. 3.13** and **3.14**), suggesting that differences in the distributions between the three populations are unlikely due to measurement variation and can therefore be used to assess differences in molecular properties between the properties. For burst size (**Fig. 3.12c**), both free coiled lambda DNA (red) and the condensed lambda DNA globules (blue) show a larger fraction of large burst sizes than the shorter free coiled 0.564 DNA fragments (green). On the other hand, packing density distributions of both free coiled DNA species are smaller than that of the SPD-condensed DNA globules (**Fig. 3.12d**). As is evident in **Fig. 3.12c** and **d**, these distributions overlap to a large degree. This makes it difficult to characterize the state of any single molecule from its burst properties. However, the geometric mean of the population distributions can serve as a useful measure of population-level differences between the three DNA species.

We compare these average packing density, burst size, and relative mobility measures over three repeat separations of each species in **Fig. 3.15**. It is apparent that any one of these parameters only provides a partial characterization of each species. Relative mobility (**Fig. 3.15a**) easily distinguishes differences in general hydrodynamic size: large free coiled lambda DNA molecules have a significantly larger mobility than both short digested DNA fragments and condensed lambda DNA globules. However, hydrodynamic mobility alone cannot distinguish changes in conformation from changes in molecular weight. At the same time, burst size can identify differences in DNA content. Both free coiled lambda DNA and condensed DNA globules have significantly larger burst sizes than short fragments. However, conformational details cannot be differentiated from this factor alone. Finally, packing density distinguished the condensed globules from both short and long free coiled DNA molecules. Through the combinatorial analysis of these individual parameters, all measured within a single experiment, one can build the complex picture of hydrodynamic size, DNA content, and conformation.

This combinatorial analysis has only been utilized to compare the average property differences between separate populations. Ideally, one would be able to utilize the burst and mobility distributions to extract the distribution of sizes, shapes, and DNA content within a single sample. We did observe a weak correlation between burst size and relative mobility within the SPD-condensed globule population (pearson's R ~ 0.28, **Fig. 3.16**) This suggests that there is some size diversity within the population, likely caused by some condensed species consisting of multiple DNA molecules or with different swelling ratios. With further improvements on sizing resolution (e.g. using a smaller capillary diameter, longer capillary diameter, and/or optimized flow rate), and optimized single molecule analysis and deconvolution algorithms, we anticipate this analysis could be improved to stract such measures of subpopulation diversity.

3.9 Conclusion

In this chapter, we have demonstrated a unique capability of our SML-FSHS platform to assess changes in global DNA conformation and DNA interactions by coupling hydrodynamic mobility analysis with single molecule burst analysis. We relate the global conformation of stained dsDNA fragments in solution to both the shape of single molecule fluorescent bursts as well as the relative hydrodynamic mobility of the fragment. We validated this analysis with conformation perturbations by topology and salt concentrations. Finally, we expanded the analysis to distinguish and characterize the size, conformations, and total DNA content of free coiled and condensed globular DNA fragments. We anticipate utility of this quantitative multiparametric analytical technique for various such as evaluation of chromatin and chromosome structure and in the development and characterization of DNA delivery vectors for gene therapy.

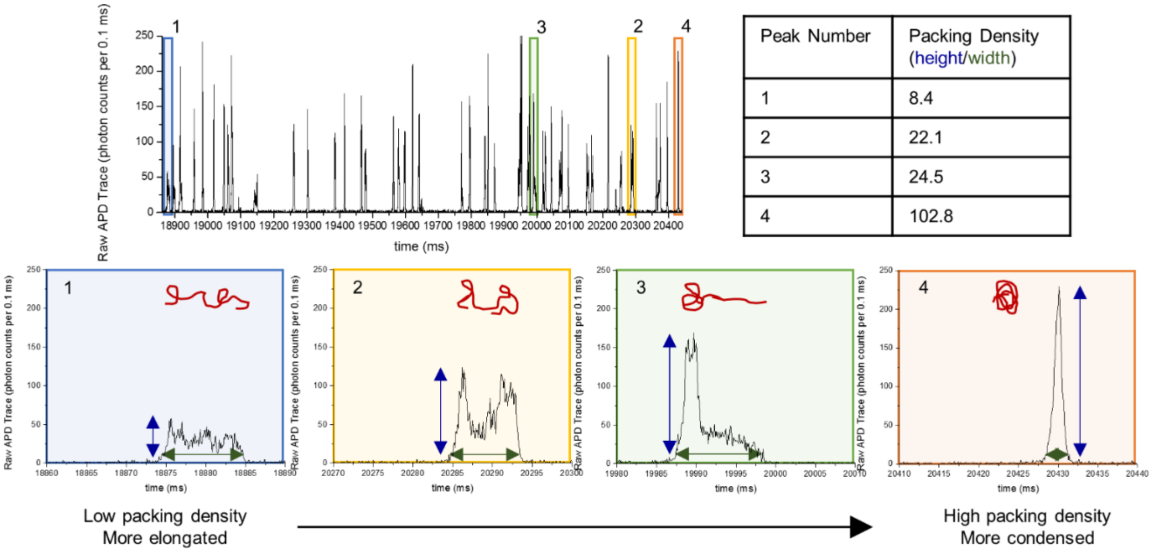

Peak Number	Packing Density (height/width)
1	8.4
2	22.1
3	24.5
4	102.8

Figure 3.1. Free coiled DNA Burst Shapes

Single molecule bursts of 23 kbp species separated in high salt conditions (25 mM NaCl) display a large variety in burst shapes ranging from stretched (1) to condensed (4), as characterized by the packing density (burst height divided by burst width). Reprinted with permission from [48]. Copyright 2016 American Chemical Society.

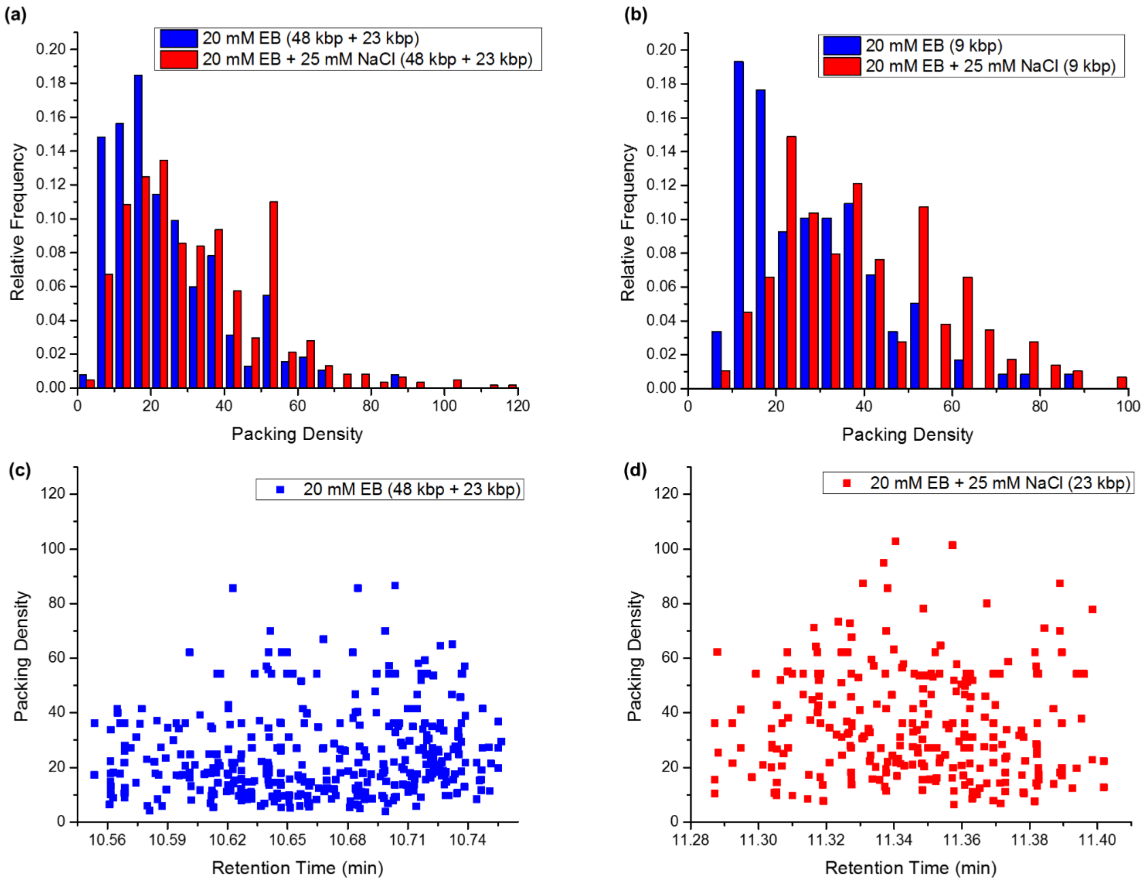
(a)
20 mM EB (48 kbp + 23 kbp)
20 mM EB + 25 mM NaCl (48 kbp + 23 kbp)
Relative Frequency
0.00
0.02
0.04
0.06
0.08
0.10
0.12
0.14
0.16
0.18
0.20
0
20
40
60
80
100
120
Packing Density
(b)
20 mM EB (9 kbp)
20 mM EB + 25 mM NaCl (9 kbp)
Relative Frequency
0.00
0.02
0.04
0.06
0.08
0.10
0.12
0.14
0.16
0.18
0.20
0
20
40
60
80
100
Packing Density
(c)
20 mM EB (48 kbp + 23 kbp)
Packing Density
0
20
40
60
80
100
120
10.56
10.59
10.62
10.65
10.68
10.71
10.74
Retention Time (min)
(d)
20 mM EB + 25 mM NaCl (23 kbp)
Packing Density
0
20
40
60
80
100
120
11.28
11.30
11.32
11.34
11.36
11.38
11.40
Retention Time (min)

Figure 3.2. Packing density distribution shift with added NaCl

The distribution of packing densities for the same length DNA fragments in different salt conditions. Histograms of the packing densities of (a) the two largest fragments – 48 kbp and 23 kbp and (b) the 9 kbp fragment in low salt (blue) and high salt (red). There exists a higher frequency of low packing densities in the low salt condition as compared to the high salt condition, and a higher frequency of high packing densities with higher ionic strength. We also investigate the relationship between packing density and retention time of the individual molecules. (c) The packing densities of the 48 and 23 kbp fragments against their retention time in the low salt buffer condition (20 mM EB). (d) Packing density vs retention time of the 23 kbp fragments in the high salt buffer condition (20 mM EB + 25 mM NaCl). The 48 and 23 kbp species are combined in the low salt condition because they could not be distinguished by their relative mobilities. These scatter plots show that molecules with both low and high packing densities elute at very similar retention times, without any obvious trends relating the two. This suggests that individual molecules are not constrained to one of the many possible conformations during the entire separation, but rather each molecule undergoes conformational fluctuation between the many conformations as it flows down the channel. It is possible that some molecules could be more constricted to some conformations (it may be difficult to transform out of some conformations), but more data would be required to discern underlying trends from this highly stochastic data. The number of molecules averaged for each DNA fragment is shown in **Table 3.3**. Reprinted with permission from [48]. Copyright 2016 American Chemical Society.

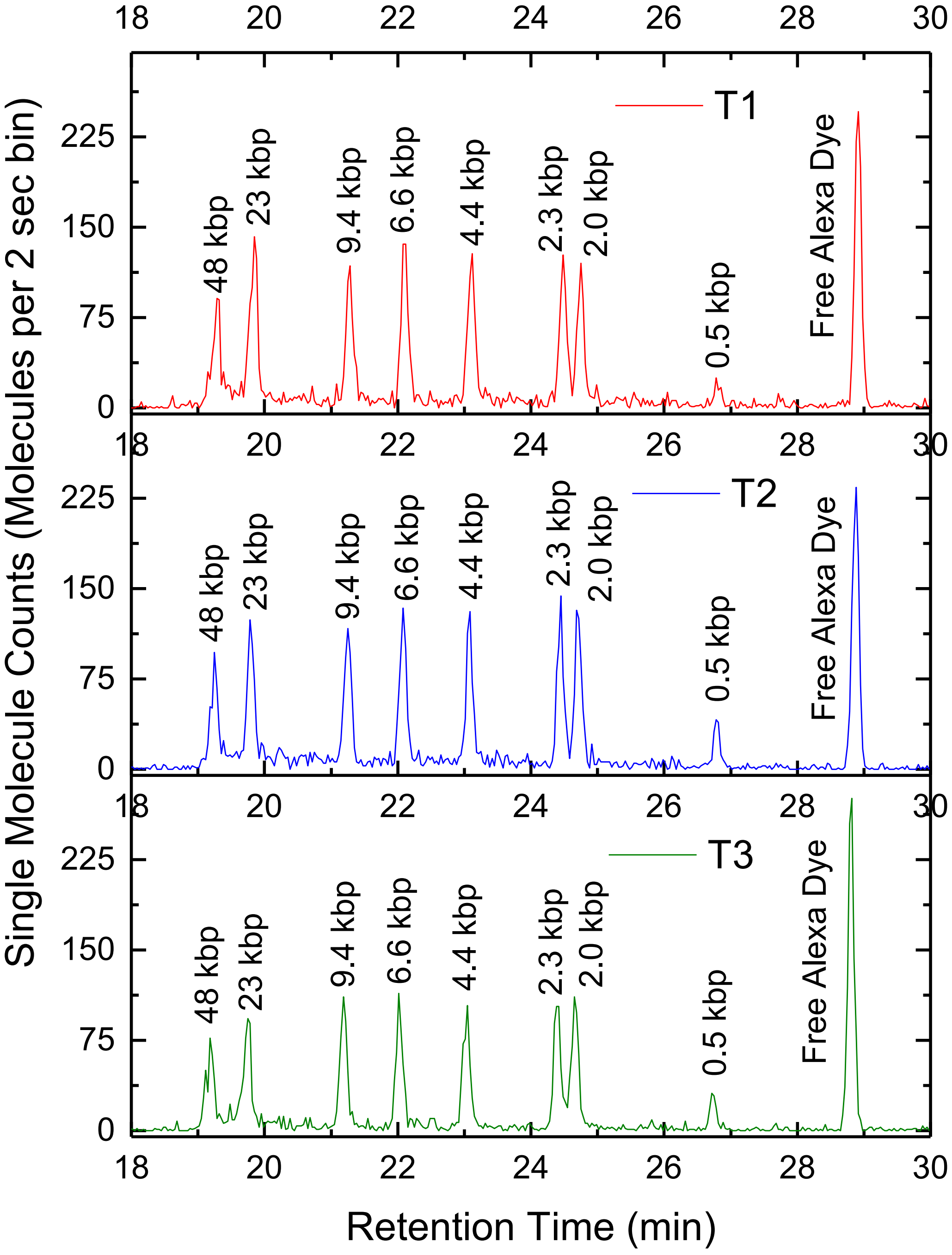

T1
T2
T3
48 kbp
23 kbp
9.4 kbp
6.6 kbp
4.4 kbp
2.3 kbp
2.0 kbp
0.5 kbp
Free Alexa Dye
Single Molecule Counts (Molecules per 2 sec bin)
Retention Time (min)
0
75
150
225
18
20
22
24
26
28
30

Figure 3.3. Repeatability of separation chromatograms.

The same sample was separated three subsequent times under the same injection and separation procedure. Each separation chromatogram (T1 - red, T2 - blue, and T3 - green) was then processed following the same data analysis procedure to assess the repeatability of the Relative Mobility, Number of Molecules, and Mean Packing Density data from each separation. These values from each fragment size of each separation are shown in **Table 3.1**, along with the average, standard deviation (SD), and coefficient of variation (CV) between the three separation runs. Under these separation and staining conditions, the single molecule fluorescence of 0.5 kbp species was close to the background, resulting in many of the molecules not being counted. For this reason, the packing density was not calculated for this species. Reprinted with permission from [48]. Copyright 2016 American Chemical Society.

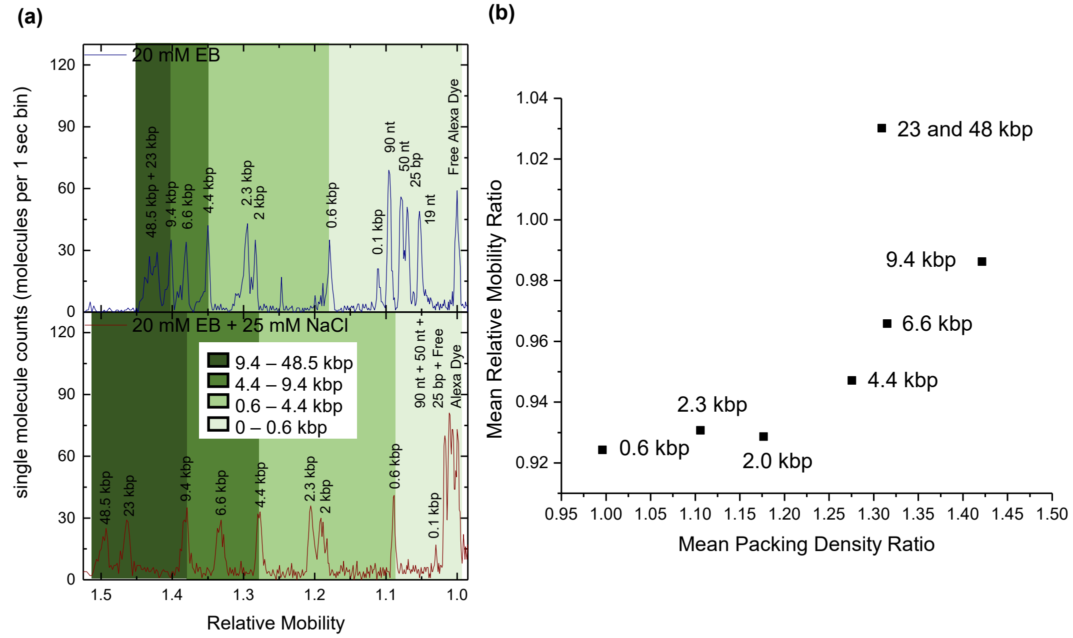
(a)
(b)
20 mM EB
20 mM EB + 25 mM NaCl
9.4 – 48.5 kbp
4.4 – 9.4 kbp
0.6 – 4.4 kbp
0 – 0.6 kbp
48.5 kbp + 23 kbp
9.4 kbp
6.6 kbp
4.4 kbp
2.3 kbp
2 kbp
0.6 kbp
0.1 kbp
90 nt
50 nt
25 bp
19 nt
Free Alexa Dye
48.5 kbp
23 kbp
9.4 kbp
6.6 kbp
4.4 kbp
2.3 kbp
2 kbp
0.6 kbp
0.1 kbp
90 nt + 50 nt + 25 bp + Free Alexa Dye
single molecule counts (molecules per 1 sec bin)
0
30
60
90
120
1.5
1.4
1.3
1.2
1.1
1.0
Relative Mobility
Mean Relative Mobility Ratio
0.92
0.94
0.96
0.98
1.00
1.02
1.04
23 and 48 kbp
9.4 kbp
6.6 kbp
4.4 kbp
2.3 kbp
2.0 kbp
0.6 kbp
0.95
1.00
1.05
1.10
1.15
1.20
1.25
1.30
1.35
1.40
1.45
1.50
Mean Packing Density Ratio

Figure 3.4. Correlation between mobility shifts and packing density

A sample comprised of 13 DNA fragments ranging in size from 19 nt to 48 kbp is separated in the same 1.6 μm diameter capillary under both low ionic strength (20 mM EB buffer) and high salt conditions (20 mM EB + 25 mM NaCl). (a) Single molecule chromatograms of both separation conditions reveal that adding salt to the separation buffer induces relative mobility changes for small and large fragments. (b) Comparison of the effect of the added salt on ratiometric changes in relative mobility and packing density of the dsDNA fragments suggests a positive correlation between the two metrics. The number of molecules averaged for each DNA fragment is shown in **Table 3.3**. Reprinted with permission from [48]. Copyright 2016 American Chemical Society.

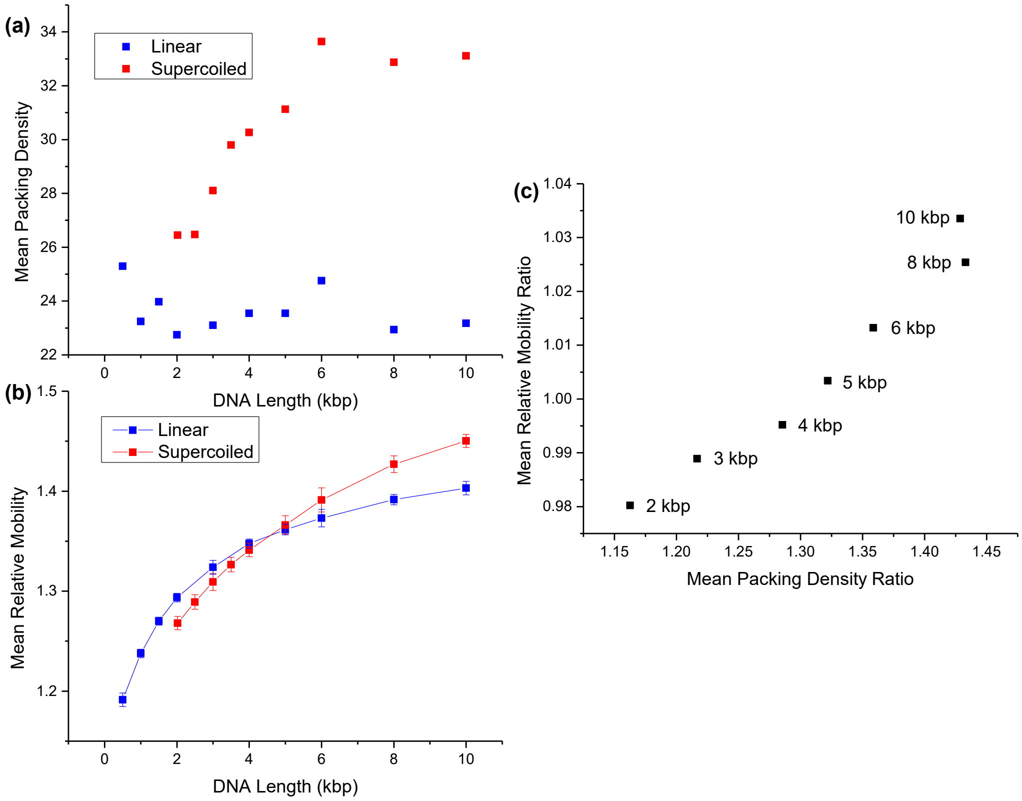
(a)
Linear
Supercoiled
Mean Packing Density
22
24
26
28
30
32
34
0
2
4
6
8
10
DNA Length (kbp)
(b)
Linear
Supercoiled
Mean Relative Mobility
1.2
1.3
1.4
1.5
0
2
4
6
8
10
DNA Length (kbp)
(c)
Mean Relative Mobility Ratio
0.98
0.99
1.00
1.01
1.02
1.03
1.04
1.15
1.20
1.25
1.30
1.35
1.40
1.45
Mean Packing Density Ratio
10 kbp
8 kbp
6 kbp
5 kbp
4 kbp
3 kbp
2 kbp

Figure 3.5. DNA topology distinguished by packing density and relative mobility
We compare the mean packing densities and mean relative mobilities of linear DNA fragments (blue) with supercoiled fragments (red) of similar lengths under the same low ionic strength separation conditions. (a) Mean packing density calculations suggest that under the same separation conditions, supercoiled fragments remain more tightly packed than their linear counterparts. (b) Supercoiled DNA fragments also travel with different relative mobilities than the linear fragments. Fragments larger than 5 kbp travel with a higher relative mobility in a supercoiled state, whereas smaller fragments appear to travel more quickly in a linear state. The error bars show the fitted width of the eluted fragment peak, which was calculated at 4 times the standard deviation. (c) The ratiometric comparison of mean relative mobility to mean packing density (supercoiled to linear) shows the same trend as Figure 3b of linear DNA under different salt conditions, where larger changes in packing density correspond to larger changes in mean relative mobility. The number of molecules averaged for each DNA fragment is shown in **Table 3.4**. Reprinted with permission from [48]. Copyright 2016 American Chemical Society.

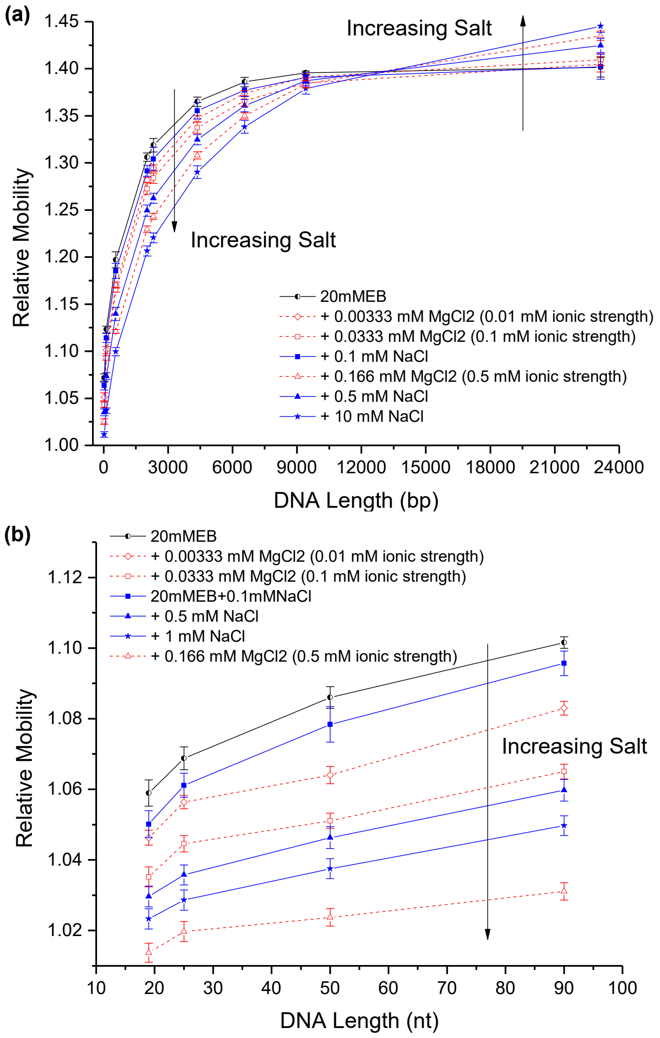
(a)
Increasing Salt
Increasing Salt
Relative Mobility
1.45
1.40
1.35
1.30
1.25
1.20
1.15
1.10
1.05
1.00
0
3000
6000
9000
12000
15000
18000
21000
24000
DNA Length (bp)
20mMEB
+ 0.00333 mM MgCl2 (0.01 mM ionic strength)
+ 0.0333 mM MgCl2 (0.1 mM ionic strength)
+ 0.1 mM NaCl
+ 0.166 mM MgCl2 (0.5 mM ionic strength)
+ 0.5 mM NaCl
+ 10 mM NaCl
(b)
20mMEB
+ 0.00333 mM MgCl2 (0.01 mM ionic strength)
+ 0.0333 mM MgCl2 (0.1 mM ionic strength)
20mMEB+0.1mMNaCl
+ 0.5 mM NaCl
+ 1 mM NaCl
+ 0.166 mM MgCl2 (0.5 mM ionic strength)
Increasing Salt
Relative Mobility
1.12
1.10
1.08
1.06
1.04
1.02
10
20
30
40
50
60
70
80
90
100
DNA Length (nt)

Figure 3.6. Monovalent and divalent salts induce biphasic mobility shifts

The effects of both sodium chloride (blue) and magnesium chloride (red) on the packing density of double stranded and single stranded DNA is probed by comparing their relative mobilities in the same 1.6 μm diameter capillary. (a) *Hind*III digested λ dsDNA is separated in a buffer with added ionic strengths of 0.01 mM (Diamond), 0.1 mM (square), 0.5 mM (triangle), and 10 (star). (b) ssDNA oligos (19 nt, 24 nt, 50 nt, and 90 nt) are separated in added ionic strengths of 0.01 mM (Diamond), 0.1 mM (square), 0.5 mM (triangle), and 1 mM (star). Error bars represent the width of each fragment's elution peak, which was calculated as 4 times the standard deviation of the fitted Gaussian peak. Adapted with permission from [48]. Copyright 2016 American Chemical Society.

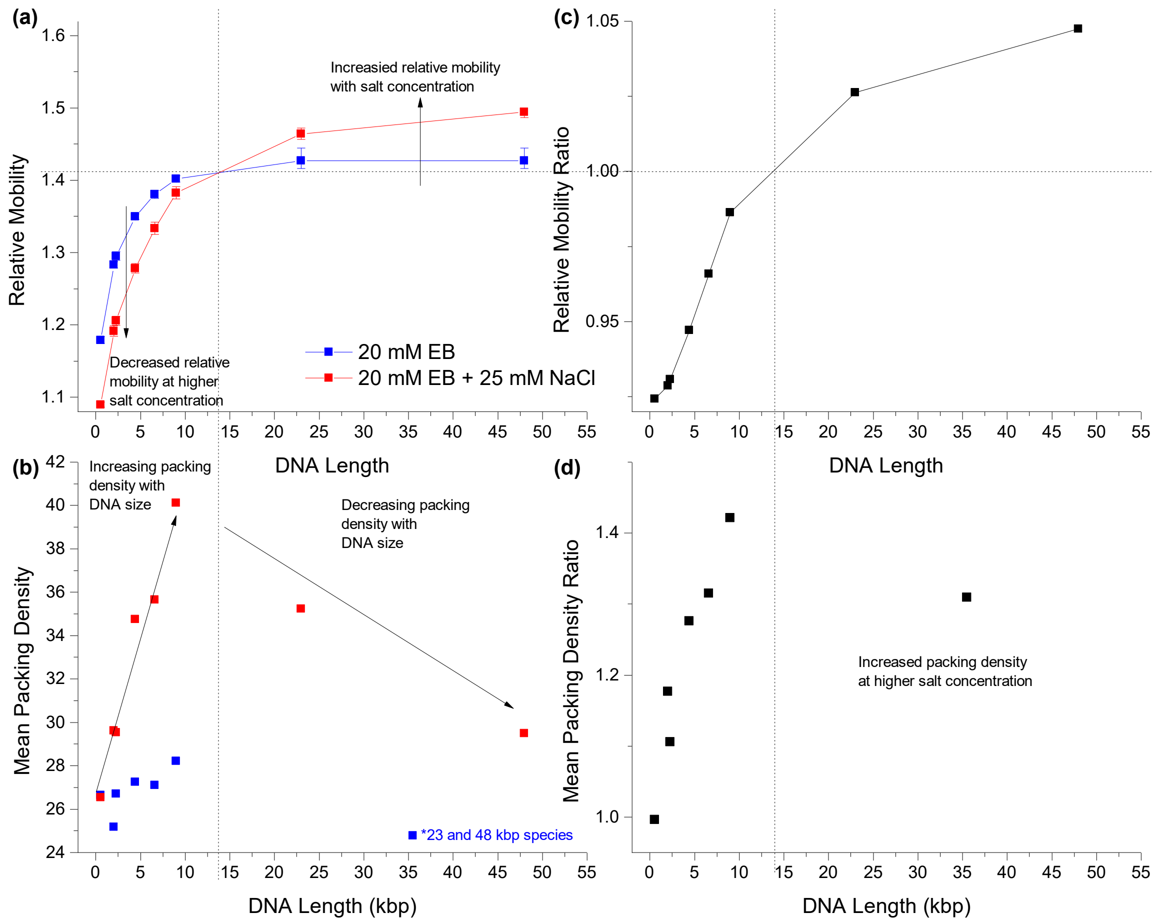
(a)
Relative Mobility
1.6
1.5
1.4
1.3
1.2
1.1
Increasied relative mobility
with salt concentration
Decreased relative
mobility at higher
salt concentration
20 mM EB
20 mM EB + 25 mM NaCl
0 5 10 15 20 25 30 35 40 45 50 55
DNA Length
(c)
Relative Mobility Ratio
1.05
1.00
0.95
0 5 10 15 20 25 30 35 40 45 50 55
DNA Length
(b)
Mean Packing Density
42
40
38
36
34
32
30
28
26
24
Increasing packing
density with
DNA size
Decreasing packing
density with
DNA size
*23 and 48 kbp species
0 5 10 15 20 25 30 35 40 45 50 55
DNA Length (kbp)
(d)
Mean Packing Density Ratio
1.4
1.2
1.0
Increased packing density
at higher salt concentration
0 5 10 15 20 25 30 35 40 45 50 55
DNA Length (kbp)

Figure 3.7. Effect of monovalent salt on packing density and relative mobility on DNA fragments.

The separations shown in **Fig. 3.4** are further analyzed in terms of relative mobility and packing density for each fragment size. (a) relative mobility and (b) packing density against DNA fragment length under low ionic strength (20 mM EB) and high ionic strength (20 mM EB + 25 mM NaCl) elution buffer conditions. For small fragment sizes relative to the capillary diameter, adding salt to the elution buffer decreases the relative mobility. In this range, too, we measure increasing packing density with DNA fragment size. This increase is more pronounced in high salt conditions compared to low salt, indicating that more DNA fragments are more compact in higher salt conditions. At fragment lengths above the crossover point, we see that relative mobility increases with the addition of salt to the elution buffer. This corresponds with a decrease in packing density with DNA size under both salt conditions (note that the 23 and 48 kbp species are averaged and reported together in the low salt condition). This indicates that these relatively large molecules are beginning to be deformed or stretched within the capillary. (c) Ratio in high salt to low salt separation conditions of relative mobility and (d) packing density against fragment length. The packing density ratio increases with DNA fragment size until we reach the crossover point, where the ratio change does not appear as drastic. This corresponds with the DNA fragments that are being deformed by the capillary size, limiting the conformations of these larger DNAs. Error bars represent the width of each fragment's elution peak, which was calculated as 4 times the standard deviation of the fitted Gaussian peak. The number of molecules averaged for each DNA fragment is shown in **Table 3.3**. Reprinted with permission from [48]. Copyright 2016 American Chemical Society.

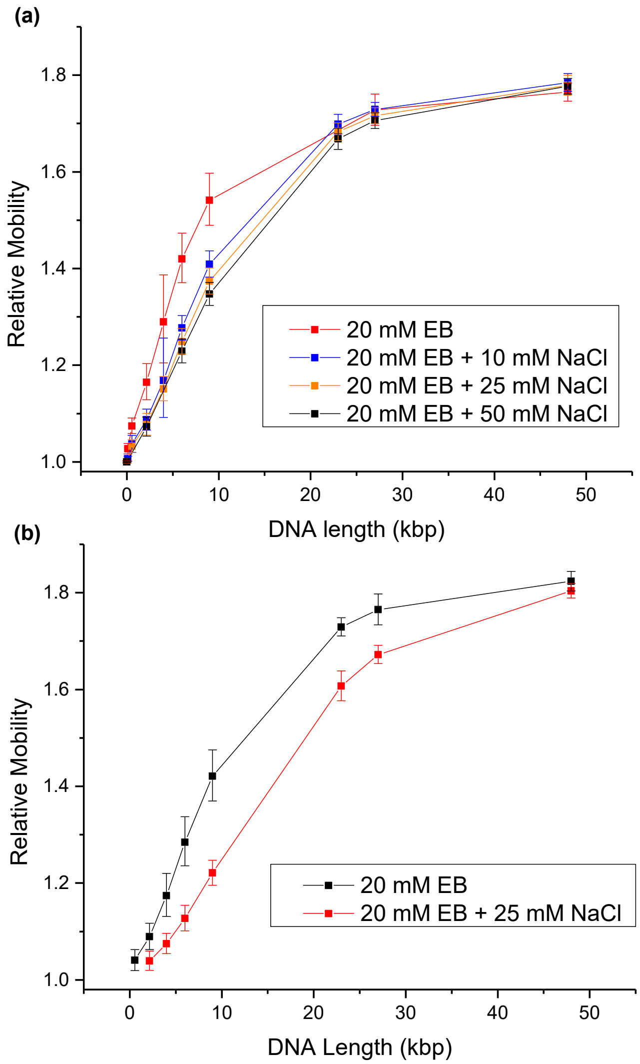
(a)
Relative Mobility
1.0
1.2
1.4
1.6
1.8
0
10
20
30
40
50
DNA length (kbp)
20 mM EB
20 mM EB + 10 mM NaCl
20 mM EB + 25 mM NaCl
20 mM EB + 50 mM NaCl
(b)
Relative Mobility
1.0
1.2
1.4
1.6
1.8
0
10
20
30
40
50
DNA Length (kbp)
20 mM EB
20 mM EB + 25 mM NaCl

Figure 3.8. Effect of capillary diameter on salt-induced relative mobility crossover Stained λ DNA and *Hind*III digested λ DNA is separated in capillaries with (a) 5 μm inner diameter and (b) 10 μm inner diameter. The separations are performed with various concentrations of sodium chloride added to the low ionic strength 20 mM EB buffer. Similar trends between salt concentration and relative mobility are seen as in the 1.6 μm ID capillary, except that with larger capillary diameters, larger DNA fragments continue to exhibit the decrease in relative mobility with increasing salt. Error bars represent the width of each fragment's elution peak, which was calculated as 4 times the standard deviation of the fitted Gaussian peak. Reprinted with permission from [48]. Copyright 2016 American Chemical Society.

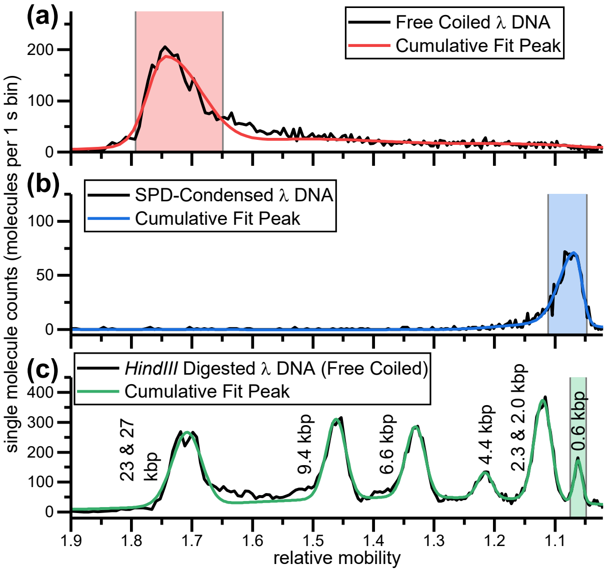
(a)
Free Coiled λ DNA
Cumulative Fit Peak
200
100
0
(b)
SPD-Condensed λ DNA
Cumulative Fit Peak
100
50
0
(c)
HindIII Digested λ DNA (Free Coiled)
Cumulative Fit Peak
400
300
200
100
0
23 & 27 kbp
9.4 kbp
6.6 kbp
4.4 kbp
2.3 & 2.0 kbp
0.6 kbp
1.9
1.8
1.7
1.6
1.5
1.4
1.3
1.2
1.1
single molecule counts (molecules per 1 s bin)
relative mobility

Figure 3.9. Chromatograms of free coiled and condensed globular DNA

Single molecule chromatograms demonstrate the effect of conformational changes on hydrodynamic separation. All three separations were performed in the same 5 μm diameter, 100 cm length capillary and were completed in less than 8 minutes. (a) Lambda DNA (48.5 kbp) is separated in a low ionic strength buffer (20 mM EB). The raw data (black) is fitted to a bigaussian peak (blue). (b) In the presence of 100 μM SPD, the mobility of Lambda DNA is significantly decreased (black is raw data and red is fitted). (c) The separation of *Hind*III digested Lambda DNA ladder in 20 mM EB is shown for comparison (black is raw data, green is fitted). The mobility of the smallest fragment (564 bp) most closely overlaps with the mobility of the condensed Lambda DNA in the presence of SPD. All chromatograms were fitted to a series of gaussian or bigaussian peaks and normalized by the free dye elution time (see Methods). The shaded region around each peak center defines 95% of the species separated peak (±2 σ).

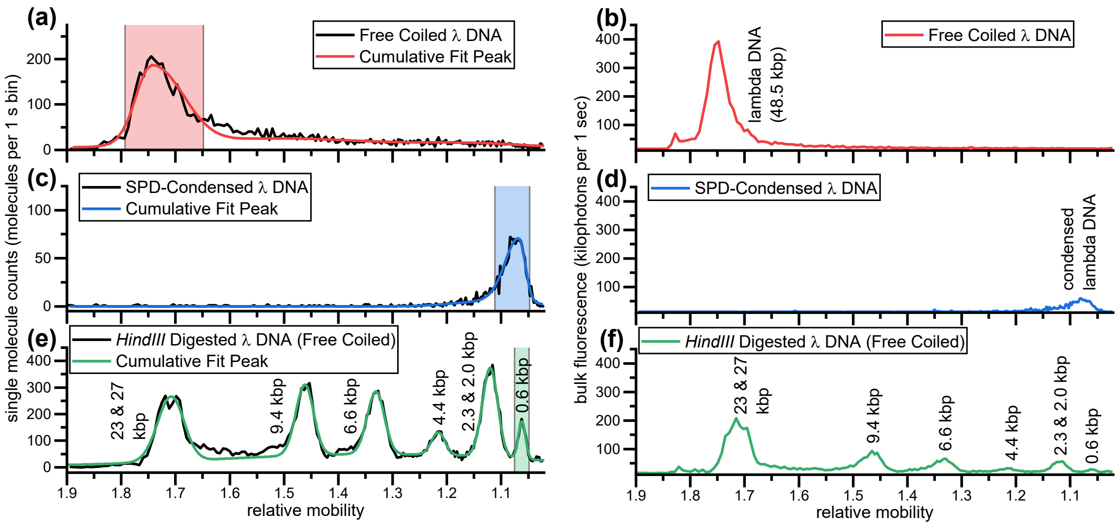
(a)
Free Coiled λ DNA
Cumulative Fit Peak
(b)
Free Coiled λ DNA
lambda DNA (48.5 kbp)
(c)
SPD-Condensed λ DNA
Cumulative Fit Peak
(d)
SPD-Condensed λ DNA
condensed lambda DNA
(e)
HindIII Digested λ DNA (Free Coiled)
Cumulative Fit Peak
23 & 27 kbp
9.4 kbp
6.6 kbp
4.4 kbp
2.3 & 2.0 kbp
0.6 kbp
(f)
HindIII Digested λ DNA (Free Coiled)
23 & 27 kbp
9.4 kbp
6.6 kbp
4.4 kbp
2.3 & 2.0 kbp
0.6 kbp
single molecule counts (molecules per 1 s bin)
bulk fluorescence (kilophotons per 1 sec)
0
100
200
50
300
400
1.9
1.8
1.7
1.6
1.5
1.4
1.3
1.2
1.1
relative mobility

Figure 3.10. Comparison of single molecule counting and bulk fluorescence analysis Single molecule chromatograms show higher sensitivity and quantification capabilities compared to total fluorescence. (a) Single molecule chromatogram of a free coiled lambda DNA separation. (b) The same separation is instead plotted as total fluorescence. (c) Single molecule chromatogram of SPD-condensed lambda DNA. (d) SPD-condensed lambda DNA separation plotted at total fluorescence. (e) Single molecule chromatogram of *Hind*III digested lambda DNA ladder separation. (f) The same separation as (e) plotted as total fluorescence. Single molecule chromatograms reveal the total molecule count regardless of molecule size, whereas bulk fluorescence displays a molecular mass dependence. This is most apparent in the *Hind*III digested lambda DNA ladder separation (compare (e) and (f)).

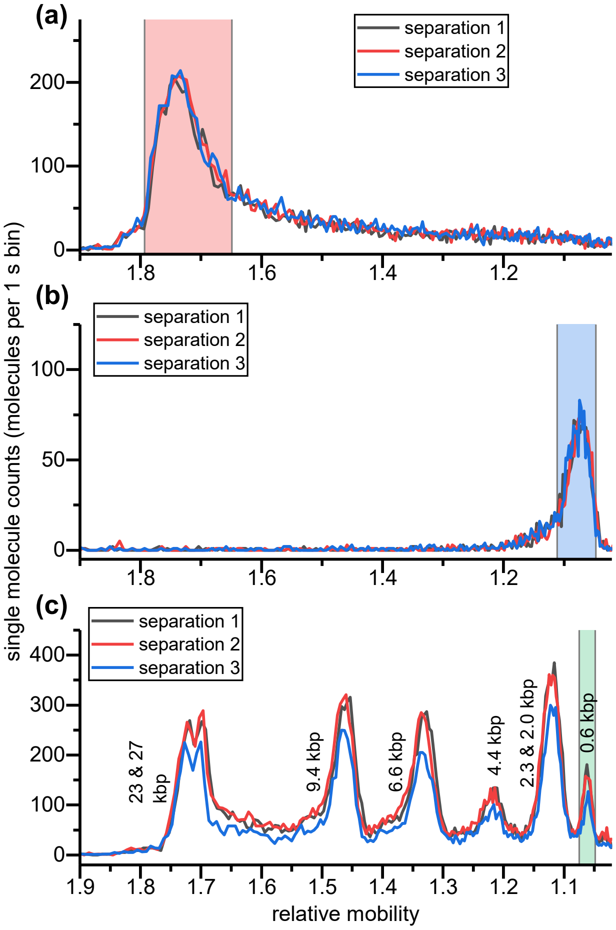
(a)
separation 1
separation 2
separation 3
200
100
0
1.8
1.6
1.4
1.2
(b)
separation 1
separation 2
separation 3
100
50
0
1.8
1.6
1.4
1.2
(c)
separation 1
separation 2
separation 3
400
300
200
100
0
23 & 27 kbp
9.4 kbp
6.6 kbp
4.4 kbp
2.3 & 2.0 kbp
0.6 kbp
1.9
1.8
1.7
1.6
1.5
1.4
1.3
1.2
1.1
single molecule counts (molecules per 1 s bin)
relative mobility

Figure 3.11. Repeatability of separations of free coiled and condensed DNA fragments.

SML-FSHS separations and single molecule are highly repeatable. The same samples were separated three times. (a) The same free coiled lambda DNA is separated three times in 20 mM EB. The red shading shows the 95% mobility range of the free coiled species averaged over the three runs. (b) The same SPD-condensed lambda DNA sample is separated three times in 20 mM EB + 100 μM SPD. The blue shading shows the 95% mobility range of the SPD-condensed species averaged over the three runs. (c) The same *Hind*III digested lambda DNA sample is separated three times in 20 mM EB. The green shading shows the 95% mobility range of the 0.564 fragment averaged over the three runs.

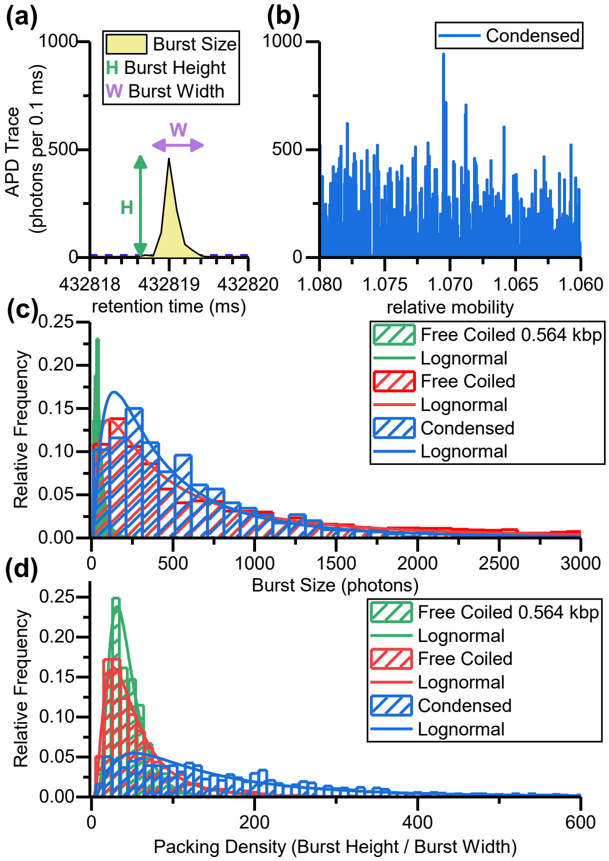
(a)
1000
500
0
APD Trace (photons per 0.1 ms)
Burst Size
H Burst Height
W Burst Width
W
H
432818
432819
432820
retention time (ms)
(b)
Condensed
1000
500
0
1.080
1.075
1.070
1.065
1.060
relative mobility
(c)
0.25
0.20
0.15
0.10
0.05
0.00
Relative Frequency
Free Coiled 0.564 kbp
Lognormal
Free Coiled
Lognormal
Condensed
Lognormal
0
500
1000
1500
2000
2500
3000
Burst Size (photons)
(d)
0.25
0.20
0.15
0.10
0.05
0.00
Relative Frequency
Free Coiled 0.564 kbp
Lognormal
Free Coiled
Lognormal
Condensed
Lognormal
0
200
400
600
Packing Density (Burst Height / Burst Width)

Figure 3.12. Single molecule burst distributions of free coiled and globular DNA fragments

Single molecule burst shapes provide further insight into molecular properties of free coiled and condensed DNA. (a) Each single molecule burst is characterized by its size (burst area) and packing density (ratio of burst height to burst width). (b) Raw data trace of hundreds of single molecule bursts detected during the separation of the condensed lambda DNA in 100 μM SPD. (c) Burst size frequency histograms fit a lognormal distribution with free coiled lambda DNA (red), SPD-condensed DNA (blue) maintaining a larger frequency of large burst sizes than free coiled 0.564 kbp fragments (green). (d) Packing density histograms also exhibit a lognormal distribution with both free-coiled species (red and green) averaging smaller packing densities than the SPD-condensed lambda DNA (blue).

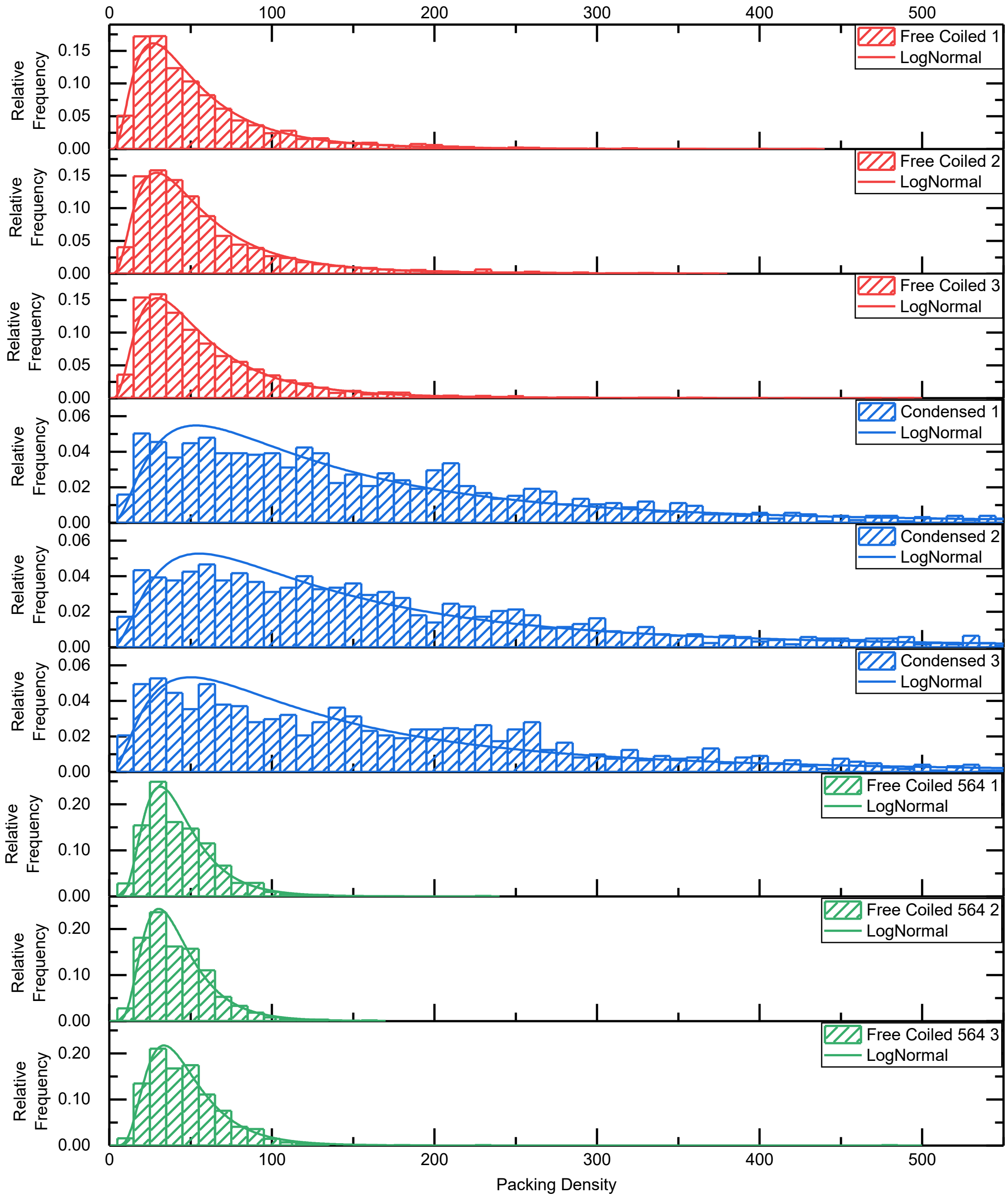
0
100
200
300
400
500
Relative Frequency
0.00
0.05
0.10
0.15
0.02
0.04
0.06
0.20
Free Coiled 1
LogNormal
Free Coiled 2
LogNormal
Free Coiled 3
LogNormal
Condensed 1
LogNormal
Condensed 2
LogNormal
Condensed 3
LogNormal
Free Coiled 564 1
LogNormal
Free Coiled 564 2
LogNormal
Free Coiled 564 3
LogNormal
Packing Density

Figure 3.13. Packing density distribution repeatability for condensation study

Histograms and lognormal fittings of repeat separations of packing densities of free coiled lambda DNA in 20 mM EB buffer (red), condensed lambda DNA in 20 mM EB buffer (blue) and free coiled 0.564 kbp DNA fragment (green).

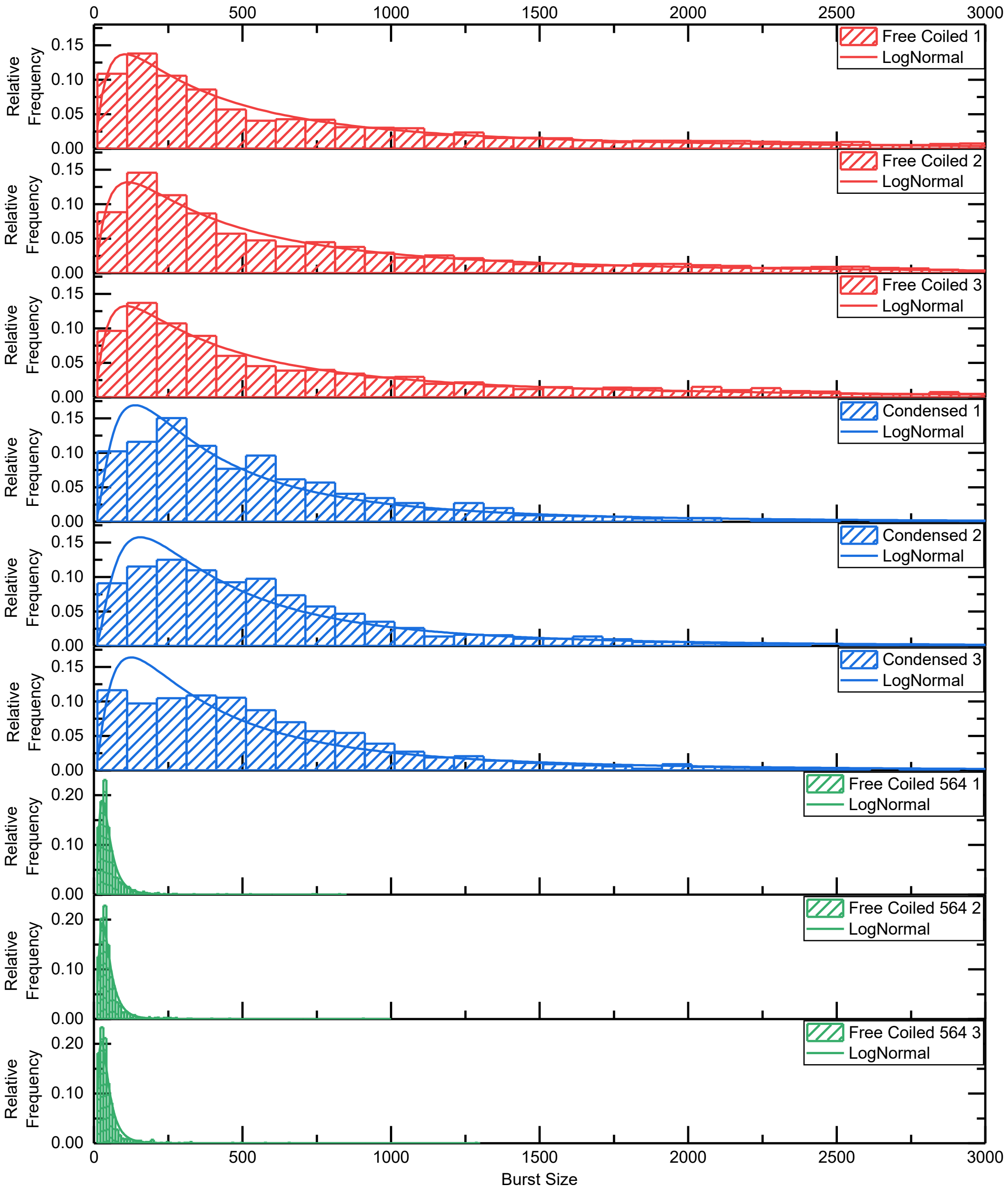
0
500
1000
1500
2000
2500
3000
Relative Frequency
0.15
0.10
0.05
0.00
0.20
Free Coiled 1
LogNormal
Free Coiled 2
LogNormal
Free Coiled 3
LogNormal
Condensed 1
LogNormal
Condensed 2
LogNormal
Condensed 3
LogNormal
Free Coiled 564 1
LogNormal
Free Coiled 564 2
LogNormal
Free Coiled 564 3
LogNormal
Burst Size

Figure 3.14. Burst size distribution repeatability for condensation study

Histograms and lognormal fittings of repeat separations of burst sizes of free coiled lambda DNA in 20 mM EB buffer (red), condensed lambda DNA in 20 mM EB buffer (blue) and free coiled 0.564 kbp DNA fragment (green).

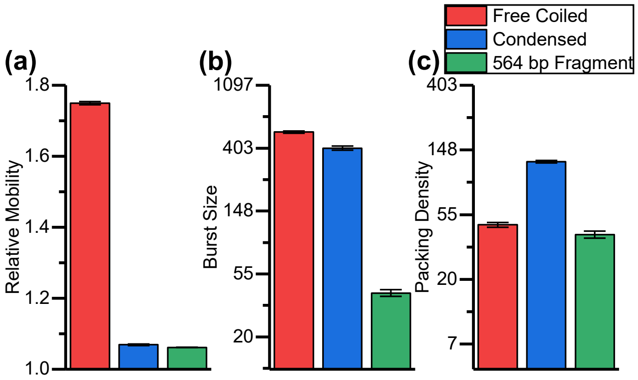
Free Coiled
Condensed
564 bp Fragment
(a)
(b)
(c)
Relative Mobility
1.8
1.6
1.4
1.2
1.0
Burst Size
1097
403
148
55
20
Packing Density
403
148
55
20
7

Figure 3.15. Multiparametric mobility and burst analysis of DNA populations

Average species mobility and single molecule burst parameters can distinguish fragment size and conformation. Bar value is average value of three separation data sets and errors bars are ± 1 standard deviation. (a) The average peak mobility of free coiled 48.5 kbp lambda DNA (red), is significantly reduced with SPD-induced condensation (red), which more closely resembles the mobility of a free coiled 0.564 kbp fragment (red). (b) The burst size geometric mean is larger for both 48.5 lambda DNA in free coiled (red) and condensed conformations, while the short 0.564 kbp fragment has the smallest burst size. (c) The packing density geometric mean is smaller for both the large 48.5 kbp free coiled DNA (red) and the short free coiled 0.564 kbp fragment and is larger for the 48.5 kbp condensed DNA species.

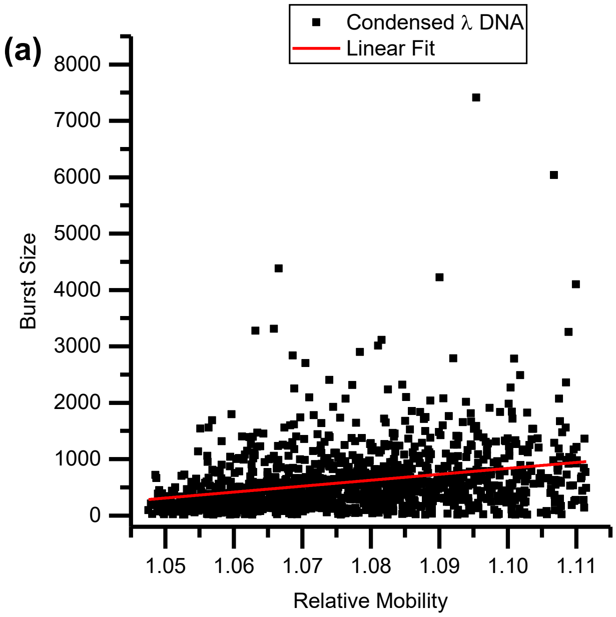

(b)

Equation	y = a + b*x
Intercept	-10729.82058 ± 1086.57804
Slope	10513.78987 ± 1008.95567
Residual Sum of Squares	3.85897E8
Pearson's r	0.28271
R-Square(COD)	0.07993
Adj. R-Square	0.07919

Figure 3.16. Relationship between burst size and relative mobility for SPD-condensed globules

Within the SPD-condensed DNA peak Single molecule burst parameters Burst size and relative mobility suggest that SPD-condensed DNA is non-uniform. (a) Single molecule burst size is plotted against single molecule relative mobility. A simple regression analysis (red) reveals some correlation between burst size and mobility. (b) Linear fit and correlation parameters. The correlation between burst size and mobility suggests that the condensed sample likely contains a small range of sizes of condensed DNA particles that contributes to the asymmetric gaussian shape. The linear regression was performed in OriginPro.

DNA Fragment Size (kbp)	Injection	Mean Relative Mobility	Number of Molecules (Fitted)	Mean Packing Density
48	T1	1.50	337	20.08
	T2	1.50	313	22.30
	T3	1.50	303	21.99
	Average	1.50	317.69	21.46
	SD	0.0011	17.279	1.199
	CV	0.07%	5%	6%
23	T1	1.46	560	19.81
	T2	1.46	443	20.75
	T3	1.46	371	20.12
	Average	1.46	457.83	20.23
	SD	0.0008	95.466	0.481
	CV	0.06%	21%	2%
9.4	T1	1.36	411	25.74
	T2	1.36	437	24.68
	T3	1.36	380	25.43
	Average	1.36	409.13	25.28
	SD	0.0004	28.423	0.545
	CV	0.03%	7%	2%
6.6	T1	1.31	467	23.64
	T2	1.31	462	22.88
	T3	1.31	378	22.85
	Average	1.31	435.62	23.12
	SD	0.0002	50.400	0.447
	CV	0.01%	12%	2%
4.4	T1	1.25	449	23.12
	T2	1.25	396	22.86
	T3	1.25	381	24.14
	Average	1.25	408.42	23.38
	SD	0.0003	35.468	0.674
	CV	0.02%	9%	3%
2.3	T1	1.18	450	23.59
	T2	1.18	457	23.01
	T3	1.18	411	22.77
	Average	1.18	439.63	23.12
	SD	0.0003	24.705	0.423
	CV	0.03%	6%	2%
2	T1	1.17	411	21.50
	T2	1.17	482	23.12
	T3	1.17	416	22.62
	Average	1.17	436.35	22.41
	SD	0.0003	39.676	0.828
	CV	0.02%	9%	4%
0.567	T1	1.08	67	--
	T2	1.08	114	--
	T3	1.08	94	--
	Average	1.08	91.50	--
	SD	0.0006	23.564	--
	CV	0.06%	26%	--

Table 3.1. Repeatability of separation and packing density data

Colors correspond to separation chromatograms T1, T2, and T3 shown in **Fig. 3.3**.

	Run 1	Run 2	Run 3
Free coiled λ	2780	3010	3036
SPD-condensed λ	1252	1223	1214
564 bp fragment	1201	1231	832

Table 3.2. Number of molecules averaged for DNA condensation analysis

Number of molecules averaged for packing density, burst size, and relative mobility comparison of free coiled and condensed globule DNA shown in **Fig. 3.11**, **3.13**, **3.14**, and **3.15**.

	48 kbp	23 kbp	9 kbp	6 kbp	4 kbp	2.3 kbp	2 kbp	0.6 kbp
20 mM EB + 25 mM NaCl	272	263	289	269	235	344	333	256
20 mM EB	384		119	152	148	243	134	172

Table 3.3. Number of molecules averaged for NaCl conformation analysis

Number of molecules averaged for packing density and relative mobility comparison of DNA with and without addition of 25 mM NaCl shown in **Fig. 3.2**, **3.4**, and **3.7**. Reprinted with permission from [48]. Copyright 2016 American Chemical Society.

	10 kbp	8 kbp	6 kbp	5 kbp	4 kbp	3.5 kbp	3 kbp	2.5 kbp	2 kbp	1.5 kbp	1 kbp	0.5 kbp
Linear	194	177	503	372	283	--	1109	--	564	627	888	1886
Super-coiled	150	138	275	629	251	319	403	339	496	--	--	--

Table 3.4. Number of molecules averaged for DNA topology conformational analysis

Number of molecules averaged for packing density and relative mobility comparison of linear and supercoiled DNA shown in **Fig. 3.5**. Reprinted with permission from [48]. Copyright 2016 American Chemical Society.

Chapter 4

4. DNA/Biomolecule Interaction Analysis

4.1 Background

In the last two chapters, we demonstrated the utility of SML-FSHS analysis for DNA fragment length and conformation analysis. In this chapter, we analyze intermolecular interactions including DNA-DNA hybridization and denaturation, and DNA-protein binding characterization. Quantitative and sensitive analysis of DNA-biomolecule interactions is fundamental in biological research, diagnostics, and therapeutic development. These interactions can be highly diverse due to the wide size range of DNA molecules and the various interacting partners, the variety and complexity of the intermolecular structures, and the assortment of binding mechanisms and forces involved. This diversity leads to a wide dynamic range in the binding properties (stoichiometry, affinity, kinetics) and the structure of the intermolecular complex (conformation, size). Efforts to develop highly sensitive and quantitative analysis methods for such a broad range of properties has led to the development of a number of individual platforms to characterize specific binding properties or types of interactions.[80-83]

However, methods based on electrophoretic mobility and separation remain widely used due to the prevalence, simplicity, and convenience of commercial gel and capillary electrophoresis platforms.[58, 84, 85] Southern blotting (or RNA hybridization in Northern blotting) utilize electrophoretic mobility and DNA hybridization to detect specific DNA sequences.[86, 87] Affinity electrophoresis methods utilize electrophoretic mobility differences between free DNA and DNA-biomolecule complexes to assess binding properties. These methods can be performed in a slab-gel; however, these techniques are labor and time intensive, expensive, and require large sample volumes. Higher speed, sensitivity, and resolution is achieved in Capillary Electrophoresis (CE) platforms. Affinity capillary electrophoresis (ACE) can be used to assess affinity and stoichiometry for a wide array of interactions (DNA-protein, DNA-DNA, DNA-small molecule) by measuring the shift in electrophoretic mobility with increasing concentrations of the interacting species the running buffer.[84, 85, 88] The electrophoretic mobility shift assay (EMSA) utilizes separation and quantification of the bound and free components to measure affinity and stoichiometry, typically for DNA-protein interaction analysis.[58, 89] Kinetic analysis of DNA-protein interactions has been demonstrated with Kinetic Capillary Electrophoresis (KCE) methods, which utilize the shapes the electrophoretograms to extract the on- and off-rates of the interaction.[90] Despite the popularity of CE-based methods, there are limitations. The use of a gel matrix to induce mobility differences in species with similar charge/mass ratios can affect the stability of intermolecular interactions.[58] Moreover, electrophoretic mobility is a function of multiple underlying factors, making it difficult to determine the molecular weight or size of an interspecies complex from the mobility shift alone.[91]

We propose SML-FSHS to be an attractive alternative. The use of hydrodynamic chromatography enables separation by size independent of charge and allows for studies of molecular interactions in native environments without a gel matrix. Additional advantages include (1) ultralow sample consumption (picoliters), (2) wide dynamic sizing range in a single run, and (3) the quantifiable relationship between elution time and effective radius.[32, 47] The sizing range and resolution is also tunable through changes in capillary dimensions, temperature, and elution buffer.[46-48] Previously, we demonstrated our SML-FSHS platform could perform highly sensitive and quantitative analysis using as few as 9 molecules of DNA in a single band.[33, 48] This high sensitivity and quantitative capability is unmatched by bulk fluorescence methods, and can enable concurrent analysis of rare and abundant species as well as quantitative analysis of a wide dynamic range of binding affinities and stoichiometries. Therefore, we anticipate that SML-FSHS can analyze DNA-biomolecule binding interactions with low reagent consumption, absolute analysis of binding-associated size and shape changes, and highly quantitative analysis of binding properties over a wide dynamic sizing and quantification range.

In this chapter, we perform single molecule free solution hydrodynamic separation to probe intermolecular binding interactions. First, we demonstrate the ability to monitor hybridization thermodynamics and binding interactions under different denaturing conditions. Next, we demonstrate that hybridization-induced mobility shifts are a function of target ssDNA oligo length and hybridization bond strength. We show that we can identify and quantify multiple hybridization events within a single sample, enabling accurate calculation of the hybridization efficiency. We also demonstrate the dynamic range to detect rare species despite excess concentrations of background molecules. We then further extend the functionality of our SML-FSHS platform to analyze DNA-protein interactions. Using *e. coli* single stranded binding protein SSB and fluorescently-labeled polyT ssDNA oligos serve as our model DNA-protein interaction, we show that single molecule detection enables quantitative analysis of the SSB-bound and free DNA oligos, and a stacked injection operating modality enables higher throughput analysis to generate a binding curve that can reveal binding stoichiometry, affinity, and cooperativity. We introduce an alternative SML-FSHS operating mode to facilitate controlled mixing within the capillary, reducing the need for cumbersome pipetting steps and further reducing reagent usage. Finally, we demonstrate direct analysis of competitive SSB-ssDNA binding to verify differences in binding mechanism and affinity.

4.2 Experimental Details

4.2.1 Buffer Preparation

EACA (6-Aminocaproic acid) and Bis-tris were purchased from Sigma and dissolved in water to 500 mM stock concentrations. It was prepared and stored at a 200 mM stock concentration (100 mM EACA and 100 mM Bis-Tris) and diluted with deionized water to 20 mM or 40 mM working concentration. Stock solutions of 5 M NaCl and 1 M $MgCl_2$ were used to create buffers with added salt. 1 M NaOH was used as stock solution for denaturation experiments. Tween-20 buffers were prepared fresh on the day of use from Tween-20 stock (Sigma-Aldrich) at 0.05% v/v.

4.2.2 Sample and Reagent Preparation

Single stranded DNA was purchased from IDT. Labeled oligos were ordered with either Alexa 647 or Cy5 covalently attached. The covalently labeled 25 bp DNA strand was synthesized and hybridized by IDT. Cy5 was covalently attached to one 24 nt long strand, which was hybridized to an unlabeled complementary strand, 26 nt long. Stocks were prepared at 100 µM and stored in -20°C for long term. For short term storage, a 1 µM stock was stored at 4C and diluted to 100 nM for each day. *E. coli* Single Stranded Binding Protein (SSB, Sigma-Aldrich) was stored at the purchased stock concentration at -20C. Before each experiment, the stock was diluted to a working concentration of 100nM in 1X or 2X EB buffer using LoBind protein tubes (Eppindorf, Sigma-Aldrich) and used to make each SSB-DNA sample. Free Alexa was purchased as dry Alexa Fluor 647 NHS Ester (Life

Technologies) and diluted in water and stored at 1 μM at 4C. It was added to all samples at 1 nM concentration to serve as the free dye marker in all separations.

4.2.3 Denaturation

Denaturation by heat and low ionic strength: DNA samples were prepared in 20 mM EB buffer and heated to 95 °C for 10 minutes before cooling to 20 °C (room temperature). Separations were performed in 20 mM EB buffer in 1.6 μm inner diameter capillary with a length of 40 cm.

Denaturation by pH: The DNA samples were prepared in 10 mM NaOH (pH 12). This was allowed to sit for at least 5 minutes before diluting the sample ten-fold in water to a final concentration of 1 mM NaOH. The separation was performed in 1 mM NaOH buffers in 1.6 μm inner diameter capillary with a length of 80 cm.

For a more detailed description of DNA denaturation and hybridization samples, please refer to reference [48].

4.2.4 Hybridization

DNA samples were prepared at 100X concentration in 100 mM NaCl, heated to 95 °C for 10 minutes, then cooled to 20 °C (room temperature) for at least 2 minutes, and then diluted 100-fold into 20 mM EB buffer. The final sample buffer contained 20 mM EB + 1 mM NaCl. The separations were performed in 20 mM EB with 1 mM NaCl buffer in a 1.6 μm inner diameter capillary with a length of 40 cm. For a more detailed description of DNA denaturation and hybridization samples, please refer to reference [48].

4.2.5 SSB-ssDNA Binding

For SSB-DNA samples, 1 nM DNA and 1 nM Alexa dye were mixed with a range of concentrations of SSB. All samples were mixed at room temperature (20-25°C) at the same time prior to beginning SML-FSHS. For plug-plug samples, a sample of 1 nM Dna and 1 nM alexa was mixed separately from various concentrations of diluted SSB and injected in series. Unless otherwise indicated, 40 mM EB buffer was used as the sample and running buffer for all samples and separations in a 2 μm inner diameter capillary with a length of 120 cm unless otherwise noted.

4.2.6 Separations

All separations were performed at room temperature in fused silica capillaries purchased from PolyMicro (Molex), with 1.6 or 2 μm inner diameters. Capillaries were cut to length and a short section of the polyimide coating was burned from the capillary to form a detection window. The capillary length L was measured as the distance between the capillary inlet and the center of the detection window. For a more detailed description of DNA denaturation and hybridization separations, please refer to reference [48].

The same SML-FSHS platform was used as described in Chapter 2. Pressure was provided by compressed argon gas through an electronic dual valve pressure controller (Alicat Scientific) for differential pressures up to 500 psi. LabView software was designed to control and record the pressure provided by the valves for precise timing and pressure control. Photon counts were collected from the APD in 0.1 or 1 ms bins using a DAQ card (National Instruments) and software written in LabView (National Instruments). Labview software was also used to control the laser power (8mW) and the flipper mount that positioned the removable mirror (Thorlabs).

DNA hybridization and denaturation separations were completed following a standard injection and separation protocol outlined in reference [48]. For stacked analysis, the capillary filled with running buffer was injected with a fresh spacer plug of running buffer for 8 minutes at 500 psi followed by a sample plug injection for 10 seconds at 300 psi (unless otherwise noted). This sequence was repeated until all samples were injected (as many as 30 sequentially stacked injections). The last sample was followed by a continuous 500 psi injection of running buffer until the last free dye peak reached the detector (~80 minutes later). For plug-plug separations, the injection step (10 seconds at 300 psi) was performed twice (once for the DNA sample and once for the protein sample) between the 8 minute running buffer spacers. Unless otherwise noted, a spacing of 8 minutes between each sample injection was used for all stacked injection experiments, although we did test a range of spacings as short as 2 minutes and 45 seconds to optimize throughput. The minimum spacing for a sample set is determined by the separation between the first and last species in each sample, which depends on the separation conditions (capillary properties, buffer, flow rate) as well as the sample contents.

4.2.7. Data Analysis

To enable continuous operation for stacked injections, APD photon counts collected when the separations were not occurring during sample switching were removed prior to further analysis. This was achieved by storing the current pressure data along with the collected APD data in a single file. Any data points that were collected with the pressure < 280 psi were discarded, and the remaining data points stitched together. This flow correction was not needed for standard separations.

The raw APD traces were corrected for color and quantum yield before performing single molecule burst analysis. Thresholding was used to detect single molecule fluorescent bursts above the background and were analyzed into 1 or 2 second bins to create the single molecule chromatograms against the retention time. OriginPro (OriginLab) was used to fit the chromatograms to a set of Gaussian peaks to compute the average retention time (peak center, t_i), quantify the number of molecules (peak areas) and compute the separation resolution (using the peak standard deviations). The relative mobility m of species i was calculated from the retention time of the free alexa dye marker:

$$m_i = \frac{v_i}{v_{dye}} = \frac{t_{dye}}{t_i} \tag{1}$$

where v_i and t_i are the average velocity and elution time of species I, respectively, and v_{dye} and t_{dye} are the average velocity and elution time of the free dye marker. The width of each fragment peak was calculated as 4 times the standard deviation (σ) of the fitted Gaussian peak and was used to determine the retention time range for each fragment size. The peak width is reported as error bars in plots of relative mobility. Relative mobility was also used to calculate the effective radius (r_i) of the eluted species:

$$m_i = 1 + \frac{2r_i}{R} + \left(\frac{r_i}{R}\right)^2 \tag{2}$$

where R is the radius of the inner lumen of the capillary. For SSB-DNA separations, the change in effective radius (Δr) was used to estimate the size effect of SSB-binding by finding the difference in effective radius of the bound complex (r_b) and the free DNA species (r_f).

$$\Delta r = r_b - r_f \tag{3}$$

4.2.8 SSB-DNA Binding Models:

For SSB-DNA binding studies, the gaussian-fitted peak areas from the single molecule chromatogram were used to quantify the DNA fraction bound (F_b) for each sample:

$$F_b = \frac{A_b}{A_b + A_f} \tag{4}$$

where A_f and A_b are the areas of the free DNA oligo and SSB-DNA complex peaks, respectively. For a protein binding experiment containing a single oligo, the DNA oligo D binds to the SSB protein B according to the following equation:

$$D + P \rightleftharpoons DP \tag{5}$$

$$K_d = \frac{[D][P]}{[DP]} \tag{6}$$

where [D], [P], and [DP] are the concentrations of free DNA, free protein, and bound protein-DNA complex, respectively, and K_d is the dissociation constant defining the stability of the complex at equilibrium. Using conservation of mass, equation 6 can be written in terms of the input DNA and protein concentrations (D_t and P_t, respectively), and F_b:

$$K_d = \frac{(1-F_b)(P_t - D_tF_b)}{F_b} \tag{7}$$

When each DNA binds to more than one protein molecule, equations 5-7 become:

$$D + nP \rightleftharpoons DP_n \tag{8}$$

$$K_d{}^n = \frac{[D][P]^n}{[DP_n]} \tag{9}$$

$$K_d{}^n = \frac{(1-F_b)(P_t - nD_tF_b)^n}{F_b} \tag{10}$$

where n indicates the number of protein molecules that bind to a single DNA molecule, assuming complete cooperativity.

In competition, two DNA oligos compete for binding to a single protein species:

$$D_1 + nP \rightleftharpoons D_1P_n, \qquad D_2 + mP \rightleftharpoons D_2P_m \tag{11}$$

This pair of interactions is described by a system of equations:

$$K_{d1}{}^n = \frac{(1-F_{b1})(P_t - nD_{t1}F_{b1} - mD_{t2}F_{b2})^n}{F_{b1}}$$

$$K_{d2}{}^m = \frac{(1-F_{b2})(P_t - nD_{t1}F_{b1} - mD_{t2}F_{b2})^m}{F_{b2}} \tag{12}$$

where K_{d1}, F_{b1}, D_{t1}, and n describe the interaction with DNA species 1, and K_{d2}, F_{b2}, D_{t2}, and m describe DNA species 2.

Fitting was performed in OriginPro using the Nonlinear Implicit Curve Fit function using Orthogonal Distance Regression. Multiple fits to a single data set were performed individually and best fit was evaluated using the Compare Models function. Both Akaike's Information Criterion Test (AIC) and Bayesian Information Criterion Test (BIC) were used to determine the best fit.

4.3 Monitoring DNA Hybridization and Denaturation

Hybridization and denaturation events result in mass and structural changes that induce hydrodynamic mobility shifts. As seen in **Fig. 4.1a**, heat was used to denature a DNA duplex into its single stranded components: a 24 nt fluorophore-labeled oligo and a 26 nt unlabeled oligo that cannot be seen. The resulting 24 nt peak has a longer retention time than the original duplex peak due to the decreased rigidity of ssDNA and its smaller effective radius. By calculating the relative mobilities (**Fig. 4.1b**), it can be seen that only the double stranded species exhibits a mobility shift due to the heating step; the mobilities of the single stranded species (90, 50, and 19 nt) remain unchanged. Such perturbations can also be made using pH. In **Fig. 4.1c**, separations were performed using 1 mM NaOH and 10 mM NaOH to denature the DNA. Using 1 mM NaOH (pH ~11), both single stranded and double stranded species were seen, suggesting that the sample was only partially denatured. When 10 mM NaOH (pH ~12) was used instead, only the single-stranded 24 nt peak was seen, indicating full denaturation. No mobility shifts were seen in the single stranded 90 nt and 19 nt DNA species.

4.4 Measuring Hybridization Efficiency and Binding Strength

Making use of mobility shifts to separate species and single molecule counting for quantification, we then examined hybridization efficiency under competitive binding conditions. In **Fig. 4.2a**, separations were performed on a sample containing a 22 nt Cy5 labeled probe and four unlabeled oligos ranging in length from 22 nt to 160 nt. Each oligo contained an identical 22 nt complementary region at the 5' end. All five of the expected species could be clearly resolved in the separation chromatogram, including the 22 bp duplex species and the 22 nt single stranded probe. Binding of an unlabeled complement to the 22 nt probe resulted in a mobility shift proportional to the length of the complementary strand. As the chromatogram is generated by direct single molecule counting, the exact number of molecules contained in each of these peaks can be easily and accurately quantified (**Fig. 4.2b**). Although the complementary regions on each oligo were identical in sequence and expected to have identical enthalpic binding contributions, the number of detected assemblies for each complement was not equal and generally decreased with length. This decrease in hybridization efficiency with length suggests an underlying entropic folding effect despite the oligos being designed to have minimal stable secondary structures.

In the previous experiment, the probe and complementary oligos were input at similar concentrations. However, in many assays and separations, molecules are often present at widely varying levels. In **Fig. 4.2c** and **d**, separation was performed on a mixture containing 1 μM 22 nt Cy5 labeled probe and 500 pM 160 nt unlabeled complement oligo. Despite this large mismatch in concentration, we could easily count 670 molecules of the hybridized assembly while simultaneously detecting a 2000-fold excess of unhybridized probes. By leveraging single molecule sensitivity and bulk fluorescence, we are able to quantify DNA across wide dynamic ranges, unmatched by other highly sensitive binding characterization methods such Fluorescence Correlation Spectroscopy (FCS).[92]

4.5 Detecting Hybridization Mismatches

Finally, we investigated the effect of hybridization mismatches on relative mobility shifts. Separations were performed on sample mixtures containing 22 nt Cy5-labeled DNA probes, mimicking the sequence of either microRNA let-7g (g) or let-7i (i), and various perfect match, 2 bp mismatch, and 3 bp mismatch oligos (**Fig. 4.3a**). As shown in Figure 7b, when probe i is hybridized to a mixture containing 160 nt and 100 nt perfect match oligos (P and N, respectively), three sharp peaks are seen in the chromatogram (**Fig. 4.3b**). If the experiment is repeated by swapping oligo N (perfect match) for oligo O, which is the same length but possesses a 3 nt mismatch, binding stability is greatly reduced and the 100 nt peak entirely vanishes (**Fig. 4.3c**). When oligo M, which is 73 nt oligo and contains a 2 nt mismatch, is swapped in, a broad smear, indicative of partial or weak hybridization, is seen (**Fig. 4.3d**). In all cases, sharp peaks corresponding to the 160 nt perfect match complement and 22 nt free probe i are unaffected (**Fig. 4.3b-d**). The same trend can be seen in Figure 7e when probe g is mixed with a 73 nt perfect match and a 160 nt oligo containing 2 bp mismatch (oligos M and P, respectively). Whereas the perfect match pair results in stable binding over the duration of a separation and appears as a sharp peak, the 2 bp mismatch pair results in weak hybridization that dynamically fluctuates over the duration of a separation and appears as a broad smear. 3 bp mismatch pairs result in binding that is too weak to be detected.

4.6 Stacked Sample Injections for DNA-Protein Binding Analysis

SML-FSHS analysis of DNA-protein binding is demonstrated with a model interaction between *E. coli* SSB and fluorescently-labeled poly(dT) ssDNA oligos (**Fig. 4.4**). A small sample plug containing an equilibrium sample of SSB and ssDNA oligo is injected in the capillary inlet. As pressure-driven flow drives the sample through the length of capillary, the larger species SSB-DNA complex, can freely access the fast flow streams near the center of the channel but are excluded from the slow flow regimes near the wall. The smaller free DNA oligo can access more of these slow flow streams, resulting in a lower average velocity. Over a long length of capillary, the two species separate by size with the larger bound SSB-DNA complex eluting first. Individual molecules are detected as unique fluorescent bursts as they pass through the detection window. A thresholding algorithm identifies and counts single molecule bursts to produce a single molecule chromatogram. This raw data is fit with gaussian curves to quantify the fraction of DNA molecules bound to SSB and to determine the average mobility and size differences between the two species.

To build a binding curve, this SML-FSHS measurement is repeated over a range of SSB:DNA concentration ratios. This is achieved by titrating SSB against a constant DNA concentration. To increase the SML-FSHS sample measurement throughput, we developed a stacked injection scheme that minimizes down time at the detector and enables concurrent sample injection and data collection (**Fig. 4.4**). Rather than waiting for a sample to pass the detector before performing the next separation, separate samples are injected in regularly spaced intervals much shorter than the total elution time. This scheme is viable for FSHS because it does not require capillary cleaning or priming between separations and both sample injection and separation are performed hydrodynamically with computer-control. We optimized the injection spacing to maintain sample differentiation with maximized throughput and verified that the stacking scheme did not reduce the quantification efficiency or separation resolution of DNA oligos (**Fig. 4.5**). The resulting binding curve can be fit to a model to reveal and quantify critical binding properties such as affinity and cooperativity.

4.7 Measuring DNA-Protein Equilibrium Binding Properties

The *E. coli* SSB protein and its interactions has been the focus of numerous studies and reviews.[93-95] Importantly, SSB forms a tetramer in solution that can bind to ssDNA in a highly salt dependent manner.[96, 97] In low salt concentrations, an SSB tetramer interacts with 35nt of ssDNA, and multiple tetramers bind to longer ssDNA strands with nearly "unlimited" cooperativity.[95] In this $(SSB)_{35}$ binding mode, SSB binds with high affinity and very low off-rates (less than 10^{-3} s^{-1}),[90, 98] particularly to poly(dT) DNA oligos, requiring very high sensitivity methods in order to be able to analyze the binding.[99-102] Thus, this low salt binding mode provides the opportunity to evaluate high binding affinity, stoichiometry, and cooperativity as a function of DNA oligo length. An ultralow ionic strength 40 mM EB buffer is used as both the binding and separation running buffers for SSB-binding analysis to 35nt and 70nt poly(dT) oligos.

First, we characterized the SSB-35nt poly(dT) interaction (**Fig. 4.6**). A series of samples are prepared with a constant 1 nM DNA concentration, and a SSB concentration range varying from 2nM to 40 nM. The sample preparation and binding conditions were optimized for separation resolution and repeatability (**Fig. 4.7-4.10**). Stacked SML-FSHS of the protein-DNA complex was performed in a 2 μm inner diameter capillary. The long continuous trace of stacked sample separations is shown in **Fig. 4.6a**. Separation of a single sample would take 80 minutes to reach the detector; stacking the injections at 8-minute intervals increases sample throughput 10-fold. As the concentration of SSB increases, a second, faster elution peak emerges before the free 35nt peak, corresponds to the SSB-DNA complex (**Fig. 4.6b**). As the SSB concentration increases, the size of the bound complex peak increases while the free DNA peak size decreases (**Fig. 4.6c**) until the DNA reaches the fully bound state. Fitting the single molecule chromatograms (black) to a series of gaussians (red) enables a highly quantitative analysis of the number of DNA molecules present in the bound and free states. This single molecule counting analysis is used to verify DNA stability (i.e. no significant DNA loss or aggregation occurs with the addition of SSB) and to calculate the fraction bound (**Fig. 4.6d**).

We fit this fraction bound plot to a binding model to evaluate the stoichiometry, affinity, and cooperativity. Typically, the $(SSB)_{35}$ binding mode is modeled as the binding of one SSB tetramer to one 35nt ssDNA. Surprisingly, this binding model did not seem to describe our data well (**Fig. 4.11a**) and attempts to adjust the model to account for protein losses (nonspecific binding, aggregation, or surface interactions) did not rectify the disparity between our results and the single-site tetramer binding model. However, our results were consistent across multiple experiments (**Fig. 4.10**). Instead, we found our data was better fit by a cooperative binding model that treats SSB as individual monomers (Section 4.2.8, equation 10). When the cooperativity parameter n was left free in the fitting procedure, it fit to $n = 3.9 \pm 0.6$ (**Fig. 4.6d**, red curve). This is consistent with the assumed binding stoichiometry: 4 SSB monomers (i.e. 1 SSB tetramer) bind to each 35nt poly(dT) oligo. In fact, a comparison of binding models found fixing $n = 4$ to be the best fitting model (**Fig. 4.11b** and **e**). Thus, our results indicate the expected binding stoichiometry, but the cooperative model suggests that SSB tetramer formation could occur upon binding to ssDNA. This unexpected outcome is likely due to the buffer composition, since SSB binding is very sensitive to cation and anion types and concentrations[95], as well as the low concentrations of protein and DNA used[103] (**Fig. 4.12**). The average dissociation constant K_D from our fitted cooperative binding model (10.0 ± 0.5 nM) is within the same order of magnitude as the low nM values reported elsewhere under similar low salt conditions, despite the difference in binding mechanism.[90, 93, 104, 105]

Next, we used the SML-FSHS platform to analyze SSB binding to a 70nt poly(dT) oligo in the same conditions. In the low salt $(SSB)_{35}$ binding mode, two SSB tetramers cooperatively bind to this longer oligo.[95] Stacked separations of a SSB titration series with the 70nt poly(dT) oligo produced the binding curve shown in **Fig. 4.13**. Again, the binding curve is better fit by considering SSB as cooperative monomers rather than tetramers (**Fig. 4.11c** and **d**). In contrast to the 35nt binding curve, the 70nt binding curve is better fit with n = 8 (**Fig. 4.11f**), in agreement with a 2 tetramer (8 monomer) binding stoichiometry. The binding affinity (K_D = 21.7 ± 0.2 nM) is slightly lower than the SSB-35nt interaction. Previous studies have described the opposite effect of oligo length on binding affinity in the high salt $(SSB)_{65}$ binding mode.[95, 101, 106] However, this dependence has not previously been reported for the low salt $(SSB)_{35}$ binding mode, possibly due to the difficulty of measuring high affinity interactions.

4.8 Non-Equilibrium Plug-Plug Analysis

In the previous section, we demonstrated the utility of a single EMSA-like operating mode to analyze the equilibrium binding properties of an isolated DNA-protein interaction. Next, we explore the utility of alternative operating modes to increase the versatility and functionality of SML-FSHS DNA-protein binding analysis. First, we demonstrate the capability to perform in-capillary binding using a plug-plug injection scheme. Rather than injecting equilibrated SSB-DNA samples, separate plugs of the DNA oligo and SSB protein are injected in series. The difference in mobility between the free DNA and SSB species enables mixing and binding during the pressure-driven separation. When an SSB plug is injected before a 35nt DNA plug, the bound complex is observed (**Fig. 4.14a**). When the plug order is reversed, however, no binding peak is observed (**Fig. 4.14b**). The same plug order dependence was also observed for the 70nt poly(dT) oligo (**Fig. 4.15**). This suggests that free SSB has a lower hydrodynamic mobility than the either free DNA oligo. The increase in mobility observed upon binding can therefore be attributed to the larger size of the SSB-DNA complex relative to either of the individual components. Plug-plug analysis could be used to minimize time consuming sample preparation steps, to control the mixing time, and to test a single sample against a variety of conditions. We used this plug-plug analysis to generate binding curves of each oligo from a single sample by varying the concentration of the SSB plug (**Fig. 4.16**). However, these binding curves are considerable right-shifted compared to the equilibrium separations (**Fig. 4.6** and **4.13**). We suspect that this shift could be used to extract reaction kinetics in a method analogous to KCE.[105]

4.9 Competitive Binding Analysis

Competitive binding analysis can also be achieved using the SML-FSHS platform. Each free oligo and SSB-ssDNA complex has a unique hydrodynamic mobility, enabling separation and quantitation of both bound factions within a single equilibrated sample (**Fig. 4.17**). As expected, no more than four species are detected for any one sample, corresponding to free 35nt, SSB-35nt complex, free 70nt, SSB-70nt complex (**Fig. 4.17b**). This suggests that no new complexes are formed under competitive binding conditions. The SSB-35nt oligo complex is formed at lower SSB concentrations than the SSB-70nt complex (**Fig. 4.17c**), in agreement with the results of the individual binding experiments. Both binding curves are fit simultaneously (Section 4.2.8, equation 12) with $n = 4$ for 35nt and $n = 8$ for 70nt. The dissociation constants determined through competitive binding analysis (11.7 ± 0.6 nM for 35nt and 22.1 ± 1.5 nM for 70nt) are consistent with the individually determined values. Moreover, the differences in mobility between the free poly(dT) oligos and the SSB-bound species can be used to estimate the size change upon binding (Section 4.2.8, equations 2 and 3).[55] The effective radius of the SSB complex was found to be ~3 nm larger for both species (3.0 ± 0.4 and 3.0 ± 0.2 for 35 and 70nt respectively), slightly smaller than stokes radius of one SSB tetramer (3.8-3.9 nm).[107, 108] Thus, SML-FSHS can effectively identify and characterize nanometer-scale size changes.

4.10. Conclusion

This chapter has demonstrated quantitative analysis of various intermolecular interactions including DNA hybridization and denaturation, and DNA-protein binding. We demonstrated the high resolution necessary to separate and distinguish single and double stranded species, enabling classification and quantification of hybridization interactions. Not only could we quantify the competitive hybridization efficiency to different length targets, but we could also distinguish the strong bond of a perfectly complementary sequence from weak binding due to sequence mismatches. Assay development requires careful and time-consuming testing and optimization, to some extent because theoretical hybridization efficiencies can differ from experimental results. This platform is capable of quantifying hybridization under experimental conditions, distinguishing false-positives from true-positives, and has the wide dynamic range to detect large concentration ranges, suggesting its utility in both assay optimization as well as end detection for multiplexed analysis.

We also demonstrated further versatility in the platform for DNA-protein binding analysis. A stacked analysis method achieved 10-fold higher throughput to analyze multiple equilibrium samples and generate a binding curve. Simple binding model fitting was used to evaluate binding affinity, cooperativity, stoichiometry, and the difference in size between the free DNA oligo and the DNA-protein complex. We also demonstrated capabilities of direct analysis of competitive binding interactions and non-equilibrium plug-plug analysis to remove excess pipetting steps. Using only pL of sample per injection and total computer control, this method has the potential for full automation and extremely low reagent usage to save time and money in an industrial analytical setting. The high sensitivity and quantitative nature of single molecule detection would also allow for detection and analysis of interactions that are difficult to study with current methods, such as rare hybrid species as well as very strong and very weak interactions.

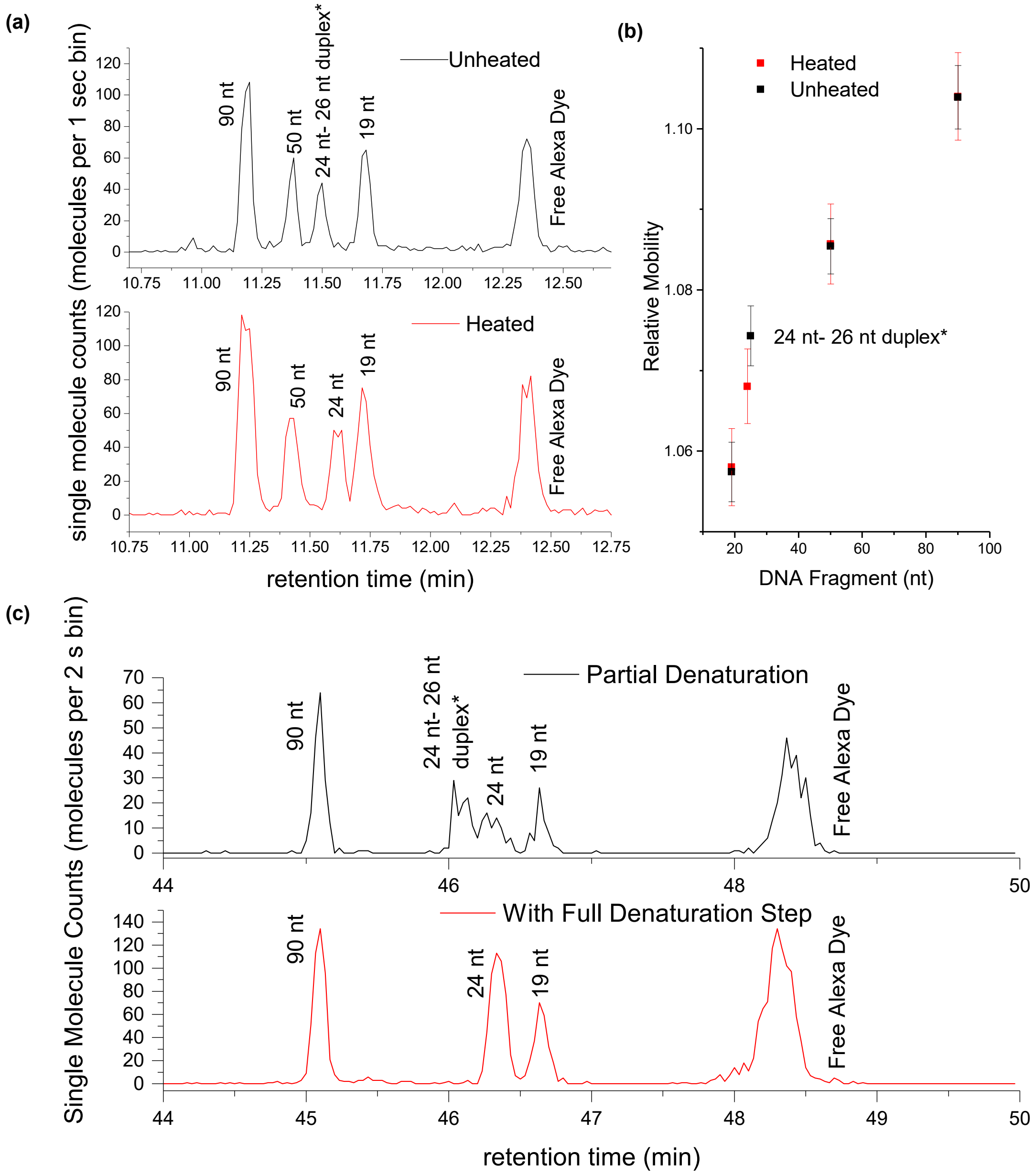
(a)
single molecule counts (molecules per 1 sec bin)
Unheated
90 nt
50 nt
24 nt- 26 nt duplex*
19 nt
Free Alexa Dye
0
20
40
60
80
100
120
10.75
11.00
11.25
11.50
11.75
12.00
12.25
12.50
Heated
90 nt
50 nt
24 nt
19 nt
Free Alexa Dye
12.75
retention time (min)
(b)
Heated
Unheated
Relative Mobility
1.06
1.08
1.10
24 nt- 26 nt duplex*
20
40
60
80
100
DNA Fragment (nt)
(c)
Single Molecule Counts (molecules per 2 s bin)
Partial Denaturation
90 nt
24 nt- 26 nt duplex*
24 nt
19 nt
Free Alexa Dye
0
10
20
30
40
50
60
70
44
46
48
50
With Full Denaturation Step
90 nt
24 nt
19 nt
Free Alexa Dye
140
45
47
49
retention time (min)

Figure 4.1. Analysis of DNA denaturation.

Denaturation of a double stranded DNA duplex into single strands results in a relative mobility shift. (a) A sample consisting of three single stranded species (19 nt, 50 nt, and 90 nt) and one double stranded species (24 nt – 26 nt duplex*) is separated in a 1.6 μm capillary at room temperature (top) and after heating the sample to 95 C for 5-10 min (bottom). (b) The average relative mobilities from the chromatograms in (a) is plotted against species size to illustrate that only the duplex mobility is affected by heating. (c) High pH environments (top – 1 mM NaOH; bottom 10 mM NaOH) also exhibit denaturation-induced mobility shifts for the duplex species only. Error bars represent the width of each fragment's elution peak, which was calculated as 4 times the standard deviation of the fitted Gaussian peak. Adapted with permission from [48]. Copyright 2016 American Chemical Society.

(a)

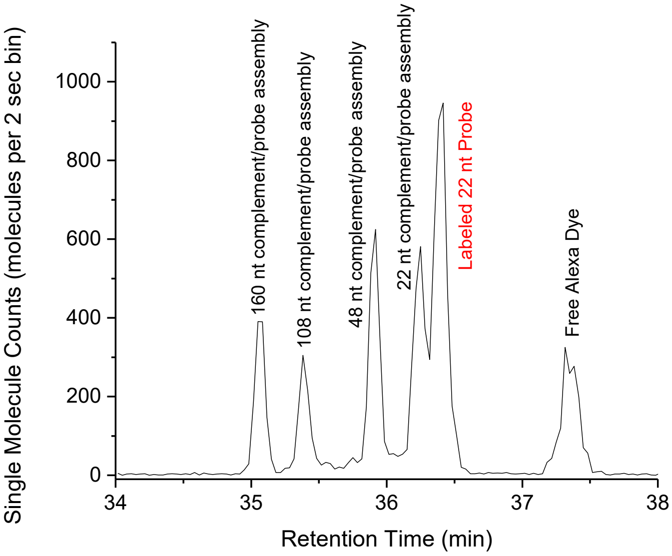

(b)

Species	Detected Assemblies	Predicted Assemblies	Hybridization Efficiency
22 nt complement assembly	1620	1670	0.97
48 nt complement assembly	1560	1670	0.93
108 nt complement assembly	810	1670	0.48
160 nt complement assembly	1160	1670	0.70

(c)

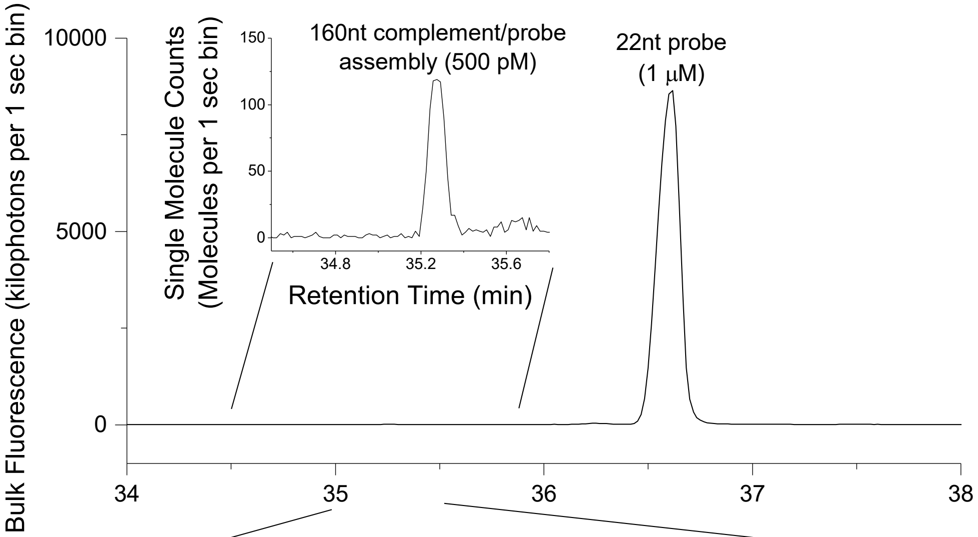

(d)

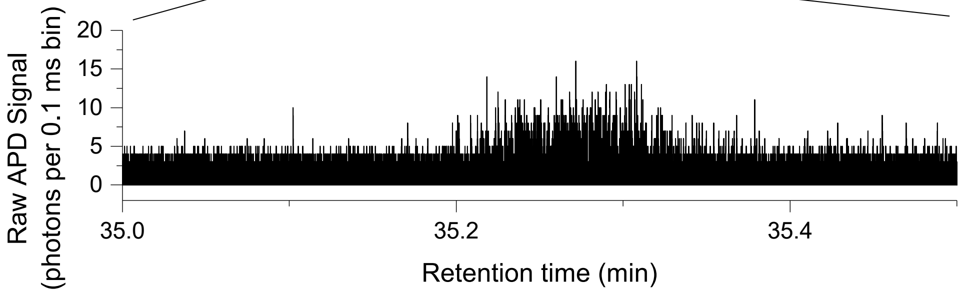

Figure 4.2. Multiplexed and high sensitivity hybridization analysis.

Hybridization of a fluorescently tagged single stranded probe to a complementary oligo is accompanied by a relative mobility shift. (a) Equal ratios of four complementary targets (lengths 22 nt, 48 nt, 108 nt, and 160 nt) are combined with a 22 nt ssDNA probe at five-times higher concentration and separated. (b) The hybridization efficiency of the competing hybridization reactions in (a) is calculated by comparing the quantity of a detected assemblies (determined by single molecule counting) with the number predicted (determined from the input ratios and the total number of fluorescent molecules present). (c) Separation and detection of the 160 nt complement/probe assembly (inset) in 2000-fold excess concentration of labeled probe. (d) The raw APD trace of the single fluorophore bursts that correspond to the hybridized 160 nt complement/probe assembly. Adapted with permission from [48]. Copyright 2016 American Chemical Society.

(a)

Oligo Complement \ Tagged Oligo Probe	i (22nt)	g (22nt)
M (73 nt)	2-nt mismatch	Perfect match
N (100 nt)	Perfect match	--
O (100 nt)	3-nt mismatch	--
P (160 nt)	Perfect match	2-nt mismatch

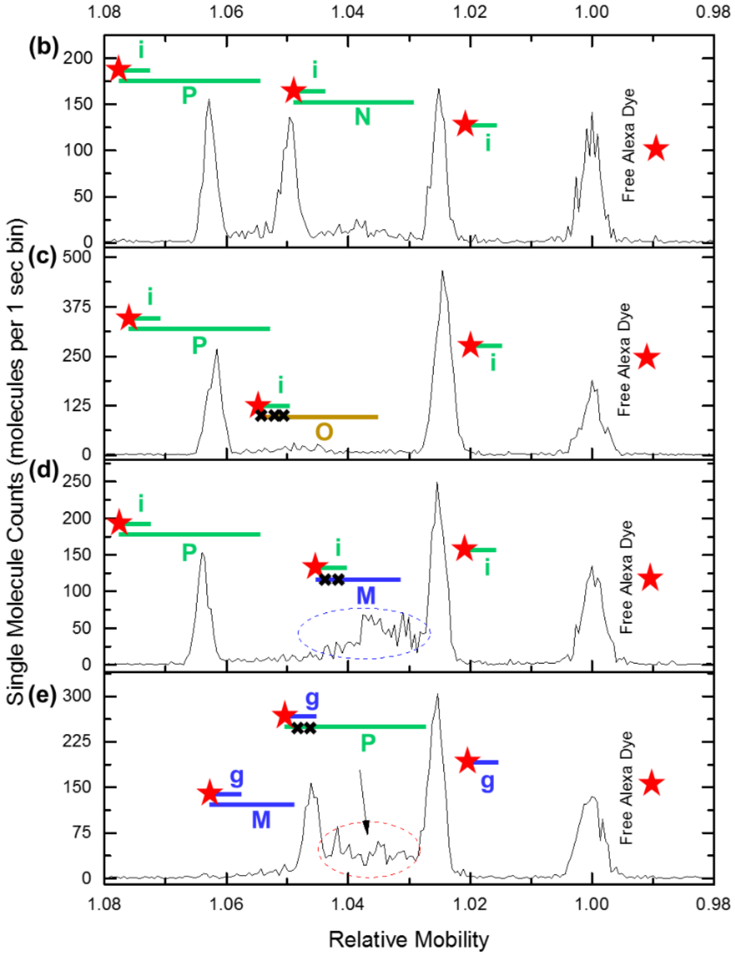

Figure 4.3. Sequence sensitivity for hybridization analysis.

Mimic sequences from the Let-7 microRNA family are used to investigate the sensitivity of hybridization-induced mobility shifted peaks to sequence complementarity and bond stability. (a) The length and complementarity of the oligo combinations used in the separations shown in (b)-(e) are listed: i and g are fluorescently tagged mimics of Let-7i and Let-7g respectively; M, N, O, and P are unlabeled oligos of varying complementarity. The species present in the chromatograms shown in (b)-(e) are labeled pictorially with probe i and its complementary oligos in green, probe g and its complements in blue, and oligo O, which does not have a fully complementary probe, in gold. Red stars designate the fluorescently labeled species: probes i and g and the free alexa dye. (b) Separation chromatogram of probe i combined with perfectly complementary oligos P (160 nt) and N (100 nt) shows distinct mobility shifted peaks for each complementary oligo. (c) No 100 nt peak is observed in the separation chromatogram when oligo P is replaced with oligo O (3 bp mismatch). (d) Separation chromatogram of probe i combined with oligos P (perfect complement) and M (73 nt oligo with 2 bp mismatch). (e) Separation chromatogram of probe g with the same M and P oligos used in (d), making M a perfect complement and P a 2 bp mismatch. Reprinted with permission from [48]. Copyright 2016 American Chemical Society.

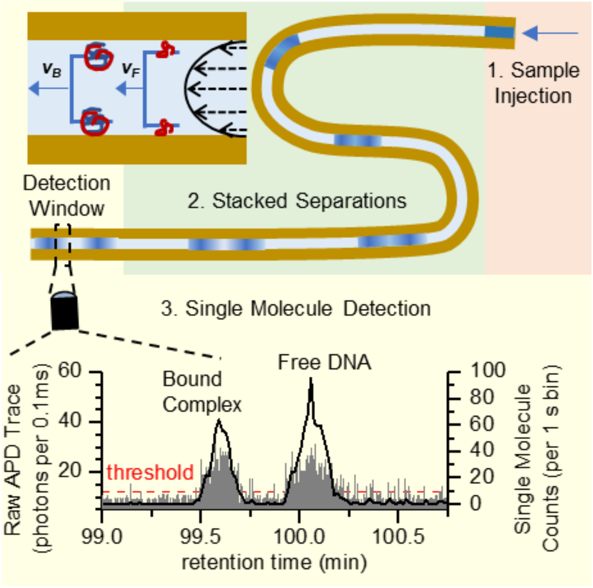

1. Sample Injection
2. Stacked Separations
Detection Window
v_B
v_F
3. Single Molecule Detection
Bound Complex
Free DNA
threshold
Raw APD Trace (photons per 0.1ms)
60
40
20
Single Molecule Counts (per 1 s bin)
100
80
60
40
20
0
99.0
99.5
100.0
100.5
retention time (min)

Figure 4.4. Stacked SML-FSHS high throughput analysis

Schematic demonstrating principal of stacked sample injection, hydrodynamic separation, and CICS-enabled single molecule counting of free DNA and bound protein-DNA complexes. Hydrodynamic Separation (inset) is achieved by applying a pressure-driven flow across a long microcapillary. Larger molecules and multi-molecular complexes exhibit a faster average velocity than smaller molecules, which can sample more slow-flow streams near the capillary walls. A short sample plug is injected at the capillary inlet (1, orange). Subsequent samples are injected before the first plug reaches the detector to increase throughput (2, green). Separated bound DNA complexes and free DNA species are detected using Cylindrical Illumination Confocal Spectroscopy (3, yellow). Individual molecule bursts (grey) are identified using a thresholding algorithm (red) and summed to generate a quantitative single molecule chromatogram (black).

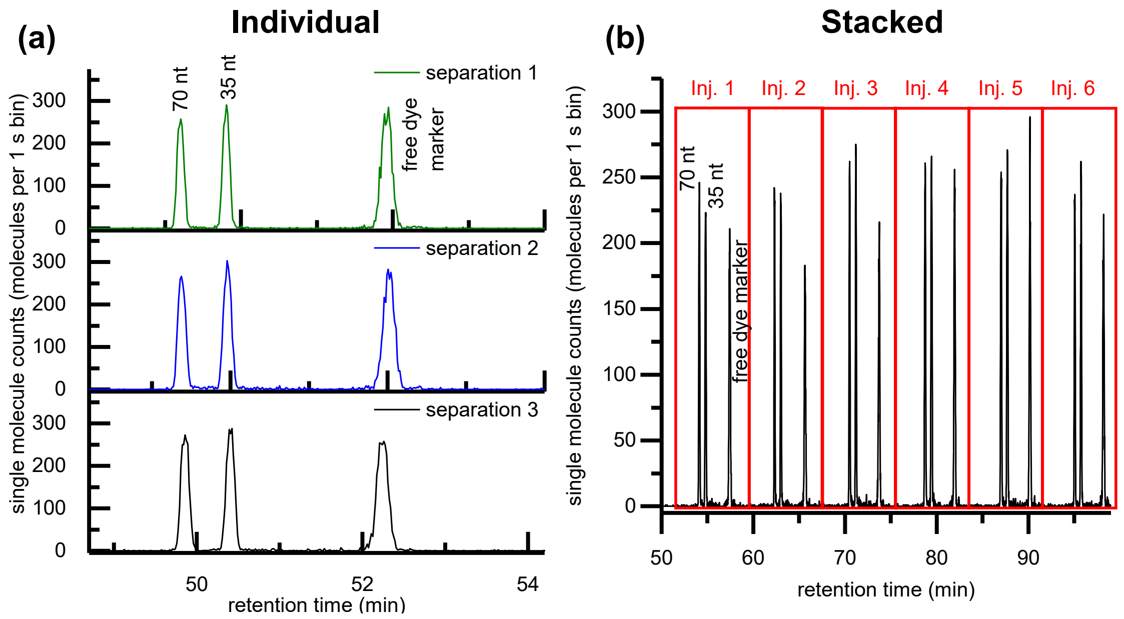

(c)

	Total Number counted (sd, cv)		Percent of Total DNA counts		Dt (from alexa)	
	Individual	Stacked	Individual	Stacked	Individual	Stacked
70 nt	1920 (140, 7%)	1930 (220, 11%)	48% (1%, 2%)	49% (1%, 2%)	2.58 (0.17, 7%)	3.22 (0.08, 2%)
35 nt	2050 (160, 8%)	2030 (270, 13%)	52% (1%, 2%)	51% (1%, 2%)	2.00 (0.15, 7%)	2.54 (0.08, 3%)

Figure 4.5. Comparison of stacked and individual separation performance

Comparison of molecule counts and resolution of stacked injections compared to standard individual separations. (a) Three repeated individual separations of 70nt polyT oligo, 35nt polyT oligo, and free Alexa 647 dye. (b) Six injections of the same sample are stacked 8 minutes apart. (c) Comparison of average molecule counts, fractions, and separation from alexa dye. Standard deviation and cv are shown in parenthesis. While there is variation in injection size, as evidenced by the ~7-13% variation in molecule counts in both individual and stacked separations, when normalized to the total amount of DNA in the injection (percent of total DNA counts), the cv decreases to only 2%, demonstrating high repeatability. Interestingly, the stacked injections showed a larger mobility change from the alexa dye than the individual injections as well as a lower cv, demonstrating that the stacked injections did not have a negative effect on the resolution of the separations.

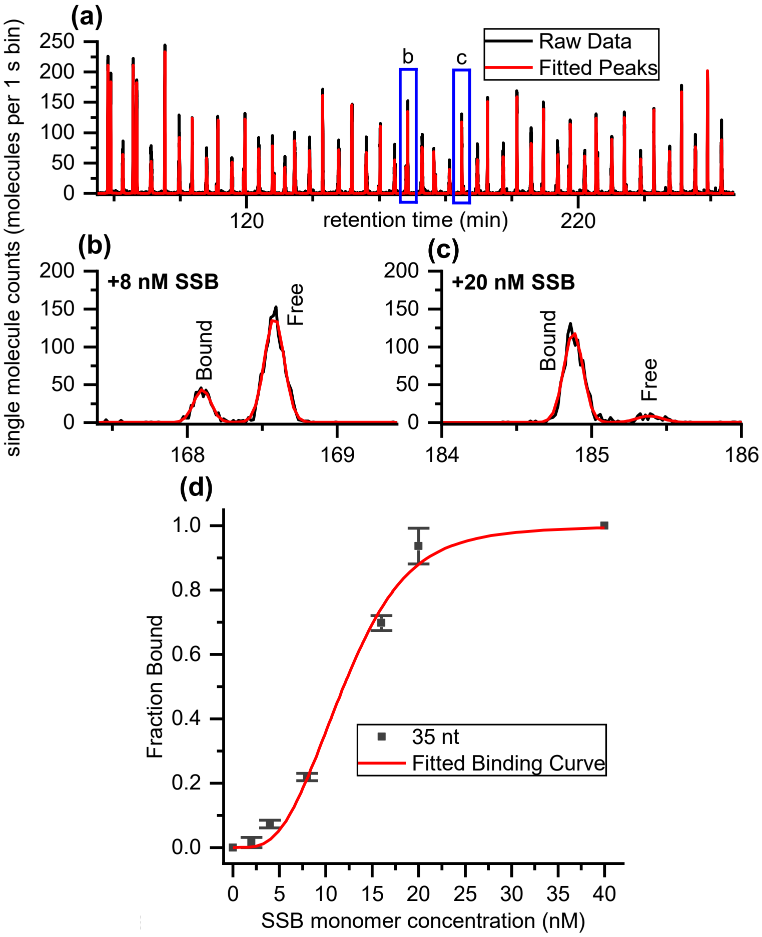
(a)
Raw Data
Fitted Peaks
b
c
250
200
150
100
50
0
120
retention time (min)
220
single molecule counts (molecules per 1 s bin)
(b)
+8 nM SSB
Bound
Free
200
150
100
50
0
168
169
(c)
+20 nM SSB
Bound
Free
184
185
186
(d)
1.0
0.8
0.6
0.4
0.2
0.0
Fraction Bound
35 nt
Fitted Binding Curve
0
5
10
15
20
25
30
35
40
SSB monomer concentration (nM)

Figure 4.6. Analysis of 35nt poly(dT) DNA oligo interaction with *E. coli* SSB protein. (a) More than 20 stacked injections of samples containing 1 nM DNA and various concentrations of SSB are separated in a 2 µm diameter microcapillary with effective length 120 cm. (b) Enlarged chromatogram from a single sample containing 8 nM SSB shows the presence of two separated species: a bound SSB-DNA complex which elutes faster than the free DNA peak. (c) The bound fraction increases when the SSB concentration is raised to 20 nM. (d) A binding curve is developed from the single set of stacked injections and fit with a cooperative binding model with n = 3.93 ± 0.6 and kD = 10.0 ± 0.5 nM.

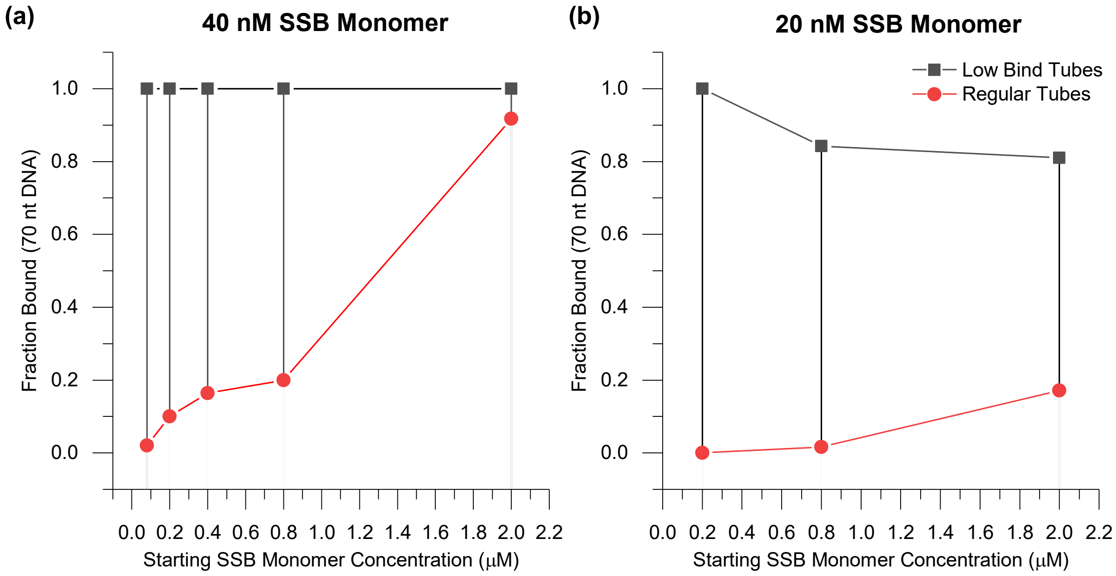
(a)
40 nM SSB Monomer
Fraction Bound (70 nt DNA)
0.0
0.2
0.4
0.6
0.8
1.0
0.0 0.2 0.4 0.6 0.8 1.0 1.2 1.4 1.6 1.8 2.0 2.2
Starting SSB Monomer Concentration (μM)
(b)
20 nM SSB Monomer
Low Bind Tubes
Regular Tubes
Fraction Bound (70 nt DNA)
0.0
0.2
0.4
0.6
0.8
1.0
0.0 0.2 0.4 0.6 0.8 1.0 1.2 1.4 1.6 1.8 2.0 2.2
Starting SSB Monomer Concentration (μM)

Figure 4.7. Optimization of sample tubes

The use of protein Low Binding tubes and pipet tips were necessary to minimize protein loss and improve sample-to-sample repeatability. Samples were prepared with the same final concentration of DNA (1nM) and final SSB concentration ((a) 40 nM SSB monomer and (b) 20 nM SSB monomer) using different starting concentrations of SSB. When using regular PCR tubes (red circles), the DNA fraction bound appeared to be a function of the starting SSB concentration. The more dilute the starting SSB concentration (y-axis), the smaller the fraction DNA bound in the final samples. When low binding tubes were used for the SSB dilutions and DNA-SSB samples (black squares), the fraction DNA bound was larger and more stable. This indicated that protein loss during sample preparation could cause significant error and instability in measurements. Low binding protein tubes and tips were used for all solutions containing SSB to minimize this effect.

(a)

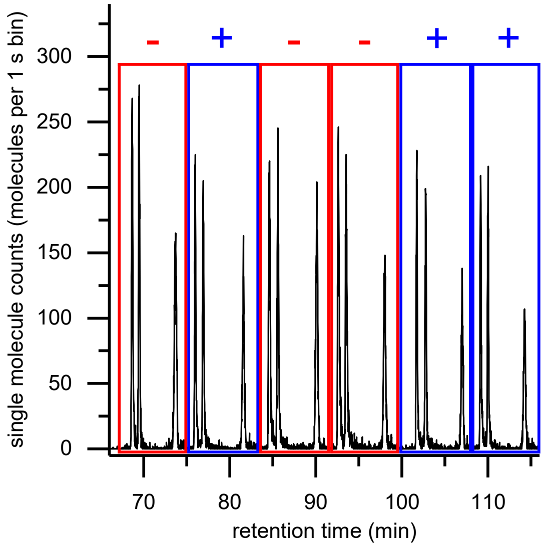

(b)

	Dt (from alexa)		Resolution (4 sigma)	
	No Tween20	+ .05% Tween20	No Tween20	+ .05% Tween20
70 nt	5.30 (0.24, 5%)	5.33 (0.25, 5%)	2.85 (0.18, 6%)	3.62 (0.24, 7%)
35 nt	4.40 (0.15, 3%)	4.38 (0.25, 6%)	11.28 (0.12, 1%)	12.68 (0.51, 4%)

Figure 4.8. Effect of Tween-20 on DNA separations

Addition of 0.05% Tween-20 did not significantly affect the resolution of DNA-only separations. (a) Stacked separation of 70nt DNA and 35nt DNA containing no added tween-20 (red) and the same DNA sample containing 0.05% tween-20 (blue). (b) Comparison of the average separation time and resolution between the following peak. Standard deviation and cv are in parenthesis. Neither the mobility or the resolution were negatively affected by the addition of tween-20. Any effects on DNA mobility were negligible. Interestingly, the resolution improved slightly with the addition of tween-20, but such a small increase without a change in mobility would not have much significance in practice.

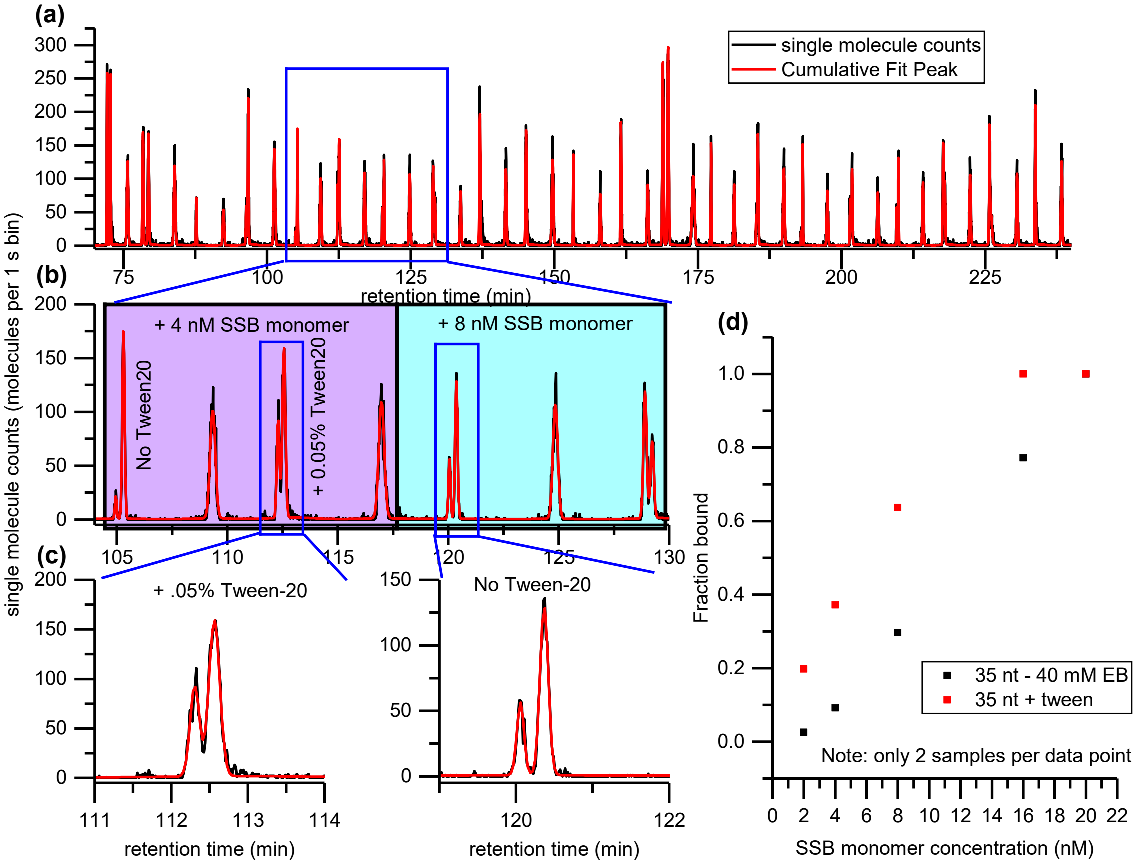
(a)
single molecule counts
Cumulative Fit Peak
300
250
200
150
100
50
0
75
100
125
150
175
200
225
retention time (min)
single molecule counts (molecules per 1 s bin)
(b)
200
150
100
50
0
+ 4 nM SSB monomer
+ 8 nM SSB monomer
No Tween20
+ 0.05% Tween20
105
110
115
120
125
130
(c)
200
150
100
50
0
+ .05% Tween-20
111
112
113
114
retention time (min)
150
100
50
0
No Tween-20
120
122
retention time (min)
(d)
1.0
0.8
0.6
0.4
0.2
0.0
Fraction bound
35 nt - 40 mM EB
35 nt + tween
Note: only 2 samples per data point
0
2
4
6
8
10
12
14
16
18
20
22
SSB monomer concentration (nM)

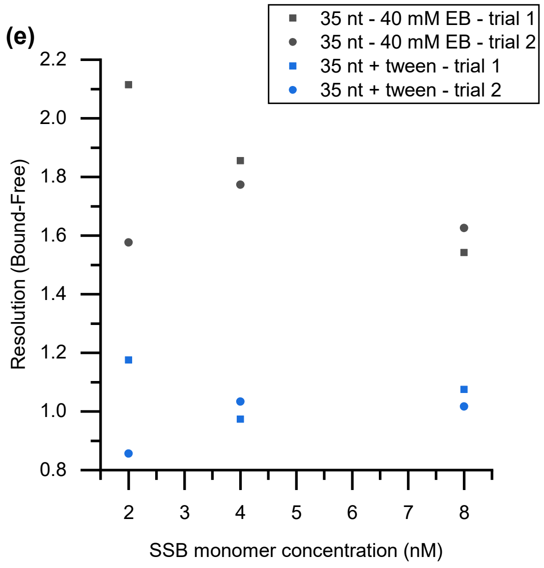
(e)
35 nt - 40 mM EB - trial 1
35 nt - 40 mM EB - trial 2
35 nt + tween - trial 1
35 nt + tween - trial 2
2.2
2.0
1.8
1.6
1.4
1.2
1.0
0.8
Resolution (Bound-Free)
2
3
4
5
6
7
8
SSB monomer concentration (nM)

Figure 4.9. Effect of Tween-20 on SSB-DNA separations

The addition of tween-20 to SSB-DNA samples affects DNA fraction bound and separation resolution between free DNA and DNA-SSB complex. Identical sets of 35nt DNA-SSB samples are prepared in with and without the addition of 0.05% tween-20. The SSB monomer concentration ranges from 2-20 nM. (a) All samples are evaluated in a single stacked separation. (b) At the same concentration of SSB, the tween-20 samples show a larger bound fraction. (c) The free and bound peaks are less resolved in tween-20 samples. (d) Fraction bound curves for both sets of samples. Tween-20 samples (red squares) bind more efficiently than those without (black circles). (e) Resolution between the bound and free peaks for two separate samples at three SSB concentrations. The loss in resolution with the addition of tween-20 could decrease quantification accuracy. The change in binding shape and decrease in separation resolution led us to believe that tween-20 could affect the binding kinetics and stability. For these reason, we chose not to include tween-20 in our separations.

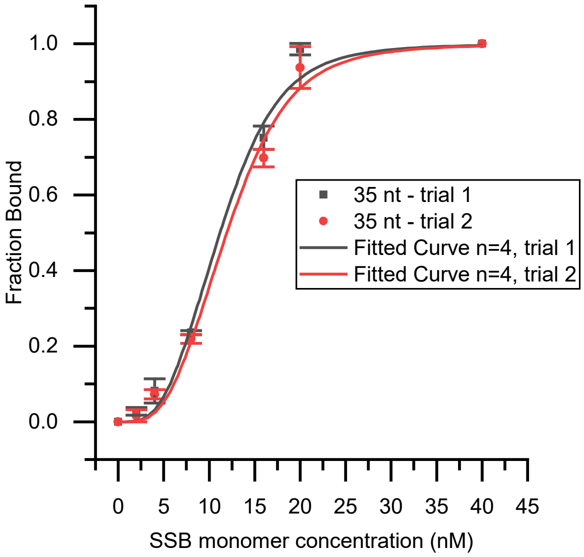
Fraction Bound
1.0
0.8
0.6
0.4
0.2
0.0
0
5
10
15
20
25
30
35
40
45
SSB monomer concentration (nM)
35 nt - trial 1
35 nt - trial 2
Fitted Curve n=4, trial 1
Fitted Curve n=4, trial 2

Figure 4.10. Day-to-day variability of protein binding curve analysis

SSB-DNA binding and separation experiments were repeated on separate days (six days apart). Very high repeatability between measurements and fitting was observed. Both data sets were fit with the cooperative binding model, n = 4. The K_D fit to 9.2 ± 0.5 and 10.0 ± 0.4 nM for trials 1 and 2, respectively.

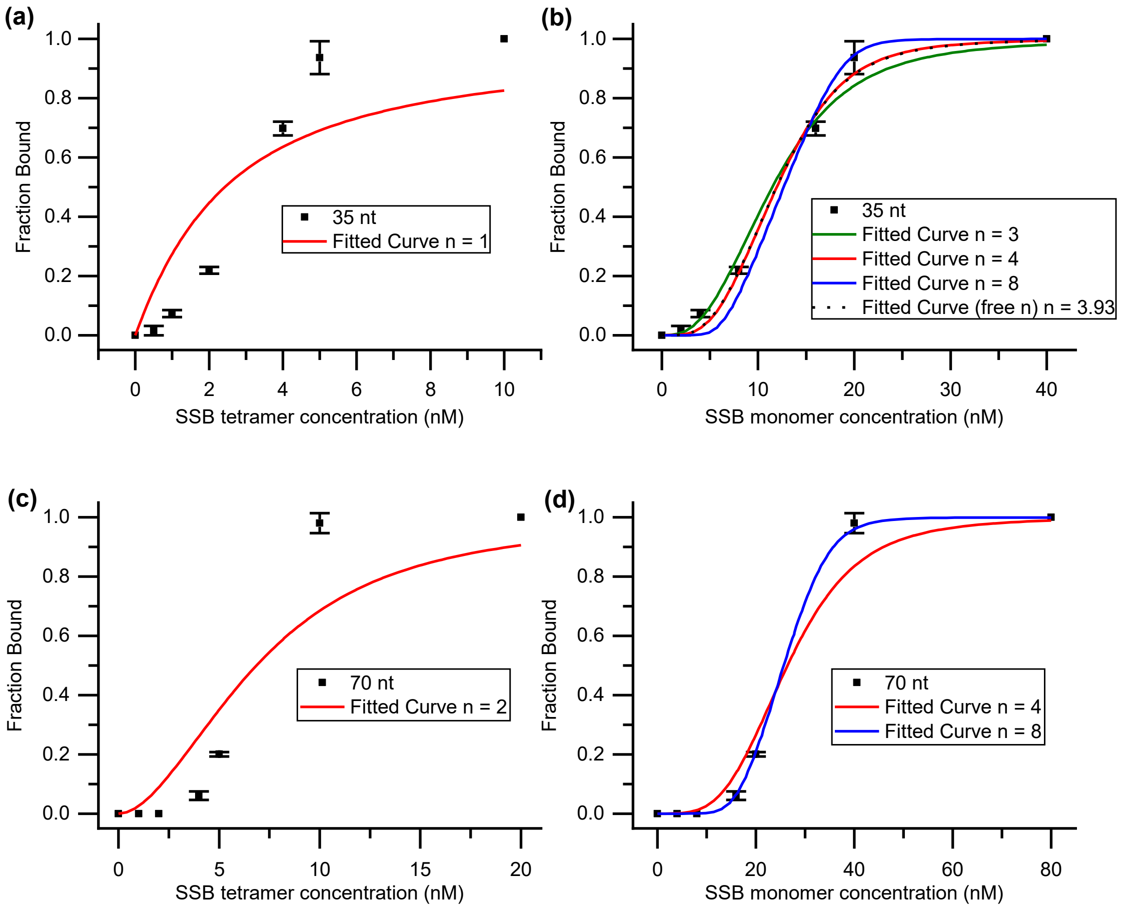

(e)

35 nt	n=1	n=free (3.93)	n=3	n=4	n=8	Best Fit
AIC	-17.84848	-33.43253	-36.90107	-40.41918	-36.02616	n=4
BIC	-20.95666	-41.5948	-40.00925	-43.52736	-39.13434	n=4

(f)

70 nt	n=2	n=4	n=8	Best Fit
AIC	-19.16321	-30.81588	-60.43239	n=8
BIC	-22.27139	-33.92406	-63.54057	n=8

Figure 4.11. Binding model fit comparisons

The binding curves were fit to various binding models to determine the best fit. These cooperative binding models treat SSB as tetramers ((a) and (c)) or individual monomers ((b) and (d)). (a) 35nt DNA binding is not well described with an SSB tetramer binding model (n = 1). (b) 35nt DNA binding is fit by treating SSB as individual monomers with binding cooperativity. Free n (dotted) fits to n = 3.93. Curves are also generated with n fixed at 3 (green), 4 (red) and 8 (blue). (c) 70nt DNA binding is not well described as cooperative binding of 2 SSB tetramers. (b) 70nt DNA binding curve is fit by binding of SSB monomers with cooperativity fixed at n = 4 (red) and n = 8 (blue). (e) and (f)The best fits were determined to be n = 4 for 35nt (b, red) and n = 8 for 70nt (d, blue) by both Akaike's Information Criterion Test (AIC) and Bayesian Information Criterion Test (BIC).

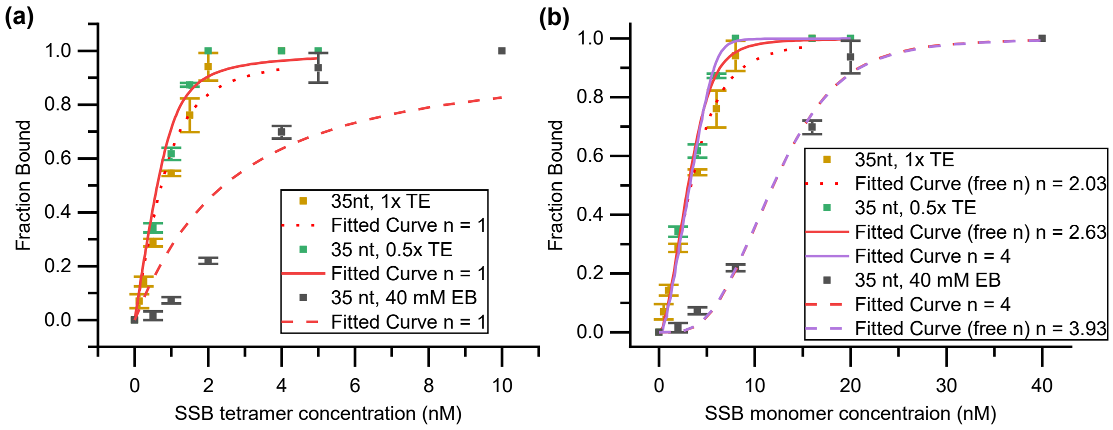
(a)
Fraction Bound
0.0
0.2
0.4
0.6
0.8
1.0
0
2
4
6
8
10
SSB tetramer concentration (nM)
35nt, 1x TE
Fitted Curve n = 1
35 nt, 0.5x TE
Fitted Curve n = 1
35 nt, 40 mM EB
Fitted Curve n = 1
(b)
Fraction Bound
0.0
0.2
0.4
0.6
0.8
1.0
0
10
20
30
40
SSB monomer concentraion (nM)
35nt, 1x TE
Fitted Curve (free n) n = 2.03
35 nt, 0.5x TE
Fitted Curve (free n) n = 2.63
Fitted Curve n = 4
35 nt, 40 mM EB
Fitted Curve n = 4
Fitted Curve (free n) n = 3.93

Figure 4.12. Effect of buffer composition on 35nt-SSB binding curve

Buffer components can greatly affect the shape of the binding curve. Binding curves for SSB-35nt interaction are completed in EB and TE (Tris-EDTA) buffer systems treating SSB (a) as tetramers and (b) as monomers. 1X TE buffer (10 mM Tris, 1 mM EDTA, titrated with HCl to pH 8.0) is significantly better fit by a simple 1:1 tetramer binding model. The 1X TE binding curve is also significantly left-shifted compared to the 40 mM EB buffer, suggesting an increase in binding affinity. Decreasing the TE buffer concentration to 0.5X results in a slightly further left-shift. This agrees with literature where decreasing the ionic strength results in an increase in the binding affinity. This suggests that buffer contents can significantly affect the binding curve shape and underlying mechanism.

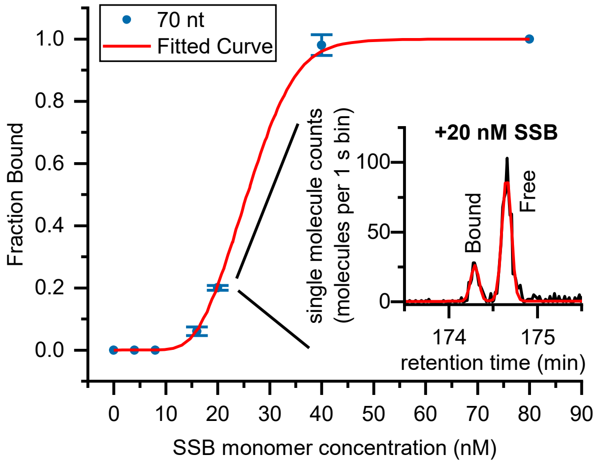
70 nt
Fitted Curve
Fraction Bound
1.0
0.8
0.6
0.4
0.2
0.0
0
10
20
30
40
50
60
70
80
90
SSB monomer concentration (nM)
+20 nM SSB
single molecule counts
(molecules per 1 s bin)
100
50
0
Bound
Free
174
175
retention time (min)

Figure 4.13. Analysis of 70nt poly(dT) DNA oligo interaction with SSB.

The same capillary and separation conditions are used as in Fig. 2. A binding curve is produced from a single set of stacked injections and fitted with a cooperative binding model with fixed n=8. The interaction fits with a lower affinity (kD = 21.7 ± 0.2 nM) than binding to 35nt poly(dT) DNA. The inset shows one chromatogram from the stack from a sample containing 1 nM 70nt poly(dT) DNA and 20 nM SSB. The bound SSB-DNA complex elutes before the free DNA species.

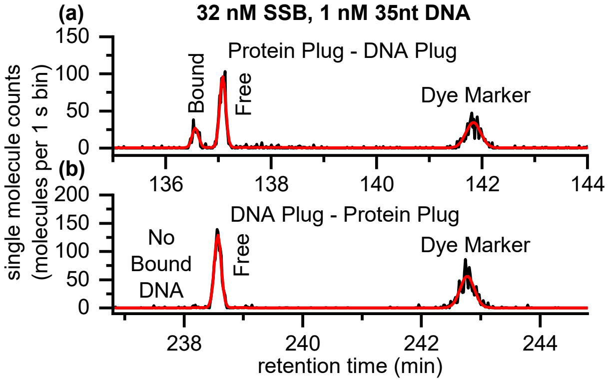
(a)
32 nM SSB, 1 nM 35nt DNA
Protein Plug - DNA Plug
Bound
Free
Dye Marker
150
100
50
0
136
138
140
142
144
(b)
DNA Plug - Protein Plug
No Bound DNA
Free
Dye Marker
200
150
100
50
0
238
240
242
244
single molecule counts (molecules per 1 s bin)
retention time (min)

Figure 4.14. Plug-plug analysis of 35nt-SSB interactions

Separate DNA and protein plugs injected in series is used to investigate binding and separation within the capillary. (a) When a plug of 32nM SSB is injected before a plug of 1 nM of 35nt DNA, a bound species is formed during separation. (b) When the DNA plug is injected before the same concentration of SSB, no binding is observed. The same capillary is used as in Fig. 2.

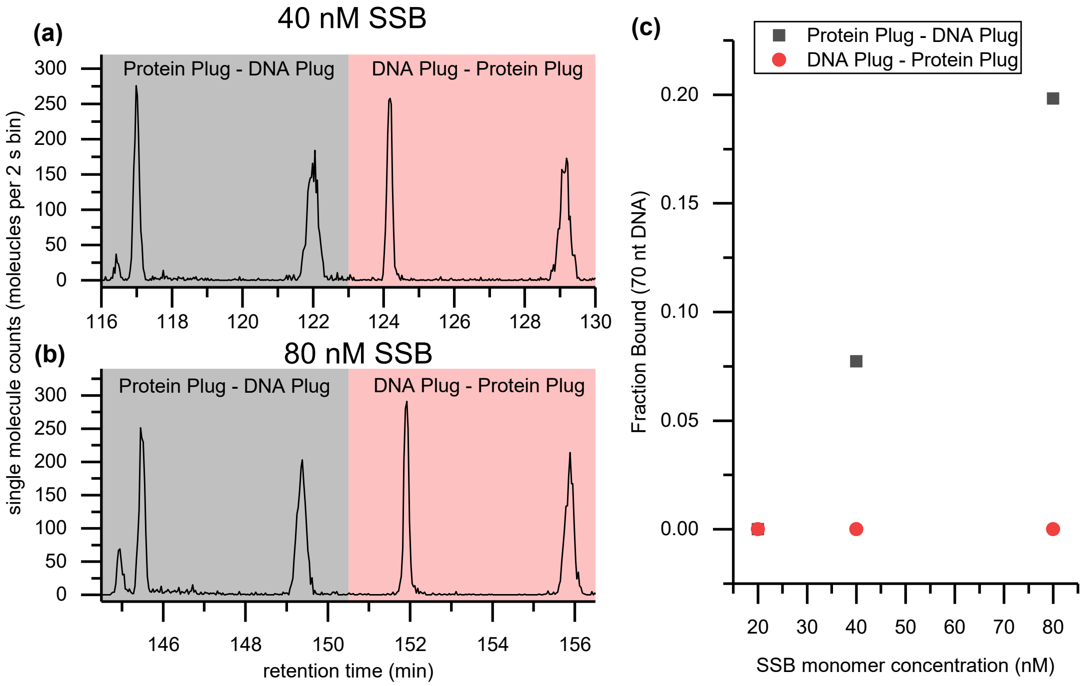
(a)
40 nM SSB
Protein Plug - DNA Plug
DNA Plug - Protein Plug
300
250
200
150
100
50
0
116
118
120
122
124
126
128
130
(b)
80 nM SSB
Protein Plug - DNA Plug
DNA Plug - Protein Plug
single molecule counts (molecules per 2 s bin)
146
148
150
152
154
156
retention time (min)
(c)
■ Protein Plug - DNA Plug
● DNA Plug - Protein Plug
Fraction Bound (70 nt DNA)
0.20
0.15
0.10
0.05
0.00
20
30
40
50
60
70
80
SSB monomer concentration (nM)

Figure 4.15. Plug-plug analysis of 70nt-SSB interaction

Plug-plug separations of 70nt DNA and SSB also only exhibited binding when the protein plug was injected before the DNA plug. (a) When a 40 nM SSB plug is injected before a 1 nM plug of 70nt DNA (grey), a bound peak is observed. Only a single free DNA peak is observed when the DNA plug is injected before the protein plug (red). (b) When the protein plug concentration is raised to 80 nM, a larger bound peak is observed when the protein plug is injected before the DNA plug (grey). Again, when the DNA plug is injected first, no bound fraction is observed (red). (c) The fraction of DNA bound to SSB increases with increasing SSB plug concentration when the protein plug is injected first. These experiments were performed in 20 mM EB. These results agree with those observed for plug-plug injections of 35nt DNA (**Fig. 4.14**).

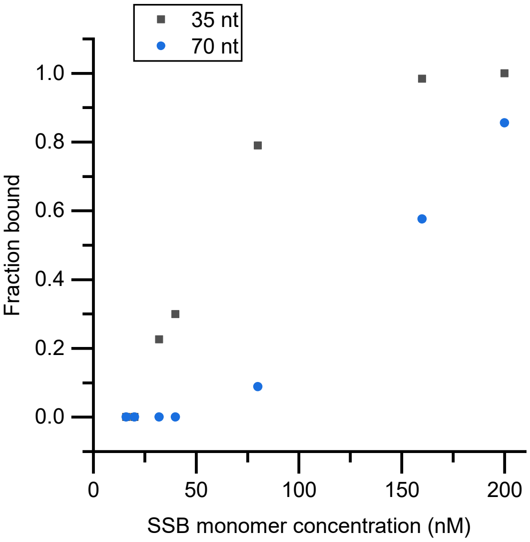

■ 35 nt
● 70 nt
Fraction bound
1.0
0.8
0.6
0.4
0.2
0.0
0
50
100
150
200
SSB monomer concentration (nM)

Figure 4.16. Plug-plug generated binding curves

Binding curves generated from plug-plug stacked separations. Each separation consisted of injection of an SSB plug (of varying concentration) followed by a 1 nM DNA plug (either 35nt, grey, or 70nt, blue). Both DNA oligos have a faster mobility than he SSB plug, enabling sample mixing during separation. SSB-DNA complexes are thus formed during the separation. Both 35nt and 70nt curves are right shifted compared to the equilibrium sample analysis (Figures 2 and 3, main text), possibly because the binding reactions do not reach equilibrium during the separation. This could provide a pathway to expand SML-FSHS binding analysis to enable kinetic analysis of the binding interactions.

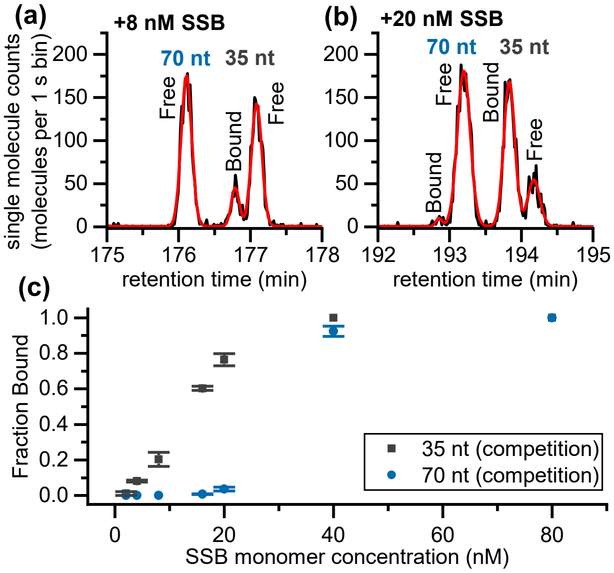
(a)
+8 nM SSB
70 nt
35 nt
Free
Bound
Free
single molecule counts (molecules per 1 s bin)
0
50
100
150
200
175
176
177
178
retention time (min)
(b)
+20 nM SSB
70 nt
35 nt
Bound
Free
Bound
Free
0
50
100
150
200
192
193
194
195
retention time (min)
(c)
Fraction Bound
0.0
0.2
0.4
0.6
0.8
1.0
0
20
40
60
80
SSB monomer concentration (nM)
35 nt (competition)
70 nt (competition)

Figure 4.17. Competitive binding analysis

Stacked SML-FSHS enables direct analysis of competitive binding between 70nt poly(dT) DNA and 35nt poly(dT) DNA for SSB. (a) In the presence of 8 nM SSB, only the 35nt DNA binds to SSB. Capillary separation conditions are the same as Fig. 2. (b) With 20 nM SSB, both DNA oligos bind to SSB, but 35nt DNA exhibits a larger bound fraction. (c) Fraction bound plot of direct competition supports the differences in binding affinity and cooperativity suggested by the individual binding experiments.

Chapter 5

5. Molecular Rheotaxis: Pressure-Driven In-Line DNA Preconcentration

5.1 Background

In the previous chapters, we have demonstrated the versatility and quantitative capabilities of our SML-FSHS separation and single molecule detection. Despite the high mass sensitivity of SML-FSHS, the extremely small sample volumes ultimately limits the concentration sensitivity. One solution to further increase sensitivity in microfluidic systems is to preconcentrate the target prior to analysis. Evaporation and solid phase extraction based concentration methods have both been demonstrated in microfluidic devices,[109-112] but electrokinetic methods are the most common and have demonstrated the highest nucleic acid concentration factors.[113, 114] Isotachophoresis (ITP) and field amplified sample stacking (FASS) are routinely used in capillary electrophoresis (CE)[115] and can achieve nucleic acid concentration factors as high as 1,000 to 10,000 fold.[116, 117] Despite the popularity of these electrokinetic methods, there remain several challenges to their implementation in microfluidic devices: namely the requirements of embedded electrodes, external power supplies, microchannel wall conditioning and treatment to reduce electroosmotic flow,[39, 40] and design considerations that avoid electric-field induced DNA aggregation and degradation.[41]

It was during the development of an electrokinetic concentration method for capillary sampling that we observed that certain conditions spontaneously triggered dilute DNA to collect into a highly concentrated bolus even without an applied electric field. Under further study we found that driving buffer flow out of the capillary actually caused DNA to migrate against the flow and gather even more quickly at the capillary inlet. We have termed the phenomenon Molecular Rheotaxis (MRT), inspired by the biological rheotaxis, alignment and migration against a flow current, of fish,[118] bacteria,[119, 120] and sperm cells,[121] and the "artificial" rheotaxis of engineered anisotropic particles[122, 123]. As this system does not require electrodes or wall coatings and uses simple buffer systems, it can be incorporated into nearly any microfluidic system or analytical chemistry platform (CE, high-pressure liquid chromatography, hydrodynamic chromatography, etc.), providing an elegant electrode-free method for DNA preconcentration.

In this chapter, we explore the underlying mechanism and concentration enhancement capabilities of this simple microfluidic preconcentration method through complementary experimental and numerical simulation approaches.[54, 124] First, a numerical model is used to pinpoint the critical experimental conditions and forces involved in the MRT concentration mechanism. Next, we investigate the effects of flow rate, time, and buffer conditions in order to further refine the mechanism and optimize the concentration enhancement. To simultaneously quantify the concentration enhancement over a wide range of DNA sizes, we couple MRT to our SML-FSHS platform. Since SML-FSHS is performed using only a buffer-filled microchannel without sieving matrices or drag-tag conjugates to modulate mobility, wall coatings, or applied electric fields,[32, 48] interfacing with MRT provides a truly electrode-free platform for highly sensitive and quantitative DNA preconcentration, size separation, and single molecule detection. Both experimental and simulation results indicate the technique is capable of effective DNA preconcentration with minimal size-dependent bias, demonstrating future applicability to a wide range of nucleic acid samples, assays, and applications. Finally, using optimized conditions with the fully integrated preconcentration and separation platform, we demonstrate concentration factors exceeding 10,000 fold with *Hind*III digested λ DNA from a starting concentration as low as 150 aM.

5.2 Experimental Details

5.2.1. Mathematical Model

In order to test the hypothesis that focusing of dsDNA is caused by a diffusion-induced electric field, a mathematical model was prepared including a 120-centimeter long capillary with a 5 micron-diameter lumen and a ζ-potential in the range, $-60\text{mV}<\zeta<0\text{mV}$, which opens abruptly into a 5 μL reservoir containing a very dilute solution, $< 5\times10^{-5}$ μg/μL, of dsDNA. Both the capillary and the sample reservoir are initially filled with a low conductivity sample buffer and, at t=0, a higher conductivity solution is pumped through the capillary toward the reservoir.

COMSOL Multiphysics® is a commercial finite element software program that allows the simultaneous simulation of multiple, coupled transient transport equations in a geometry fabricated in 0-, 1-, 2- or 3-dimensions. We started building our model in COMSOL by choosing a 2D-axisymmetric coordinate system, then assembling the geometry to which we would apply our model equations (**Fig. 5.1**), adding information regarding the properties of the materials in our model and then setting the model equations, boundary conditions and initial conditions.

In this model, an applied pressure of 200 psi across a 120 cm capillary with a 5 μm lumen produces a flow velocity less than 0.03 cm/s, which yields a lumen Reynolds number below 0.001 for water at 25°C. Therefore, a vortex-free laminar flow can be assumed so we can use the incompressible Navier-Stokes equations together with the equation of continuity,

$$\rho\frac{\partial \mathbf{v}}{\partial t}+\rho\mathbf{v}\cdot\nabla\mathbf{v}=-\nabla p+\nabla\cdot\mu_{eff}\nabla\mathbf{v} \tag{1}$$

$$\nabla\cdot\mathbf{v}=0 \tag{2}$$

to model both the flow, **v**, from the capillary lumen into the sample reservoir as well as the reverse flow as DNA is drawn into the lumen. Note that since this is a closed flow system, the gravitational body force term has been subsumed into the augmented pressure, *p*, and natural convection is neglected. The effective viscosity term takes into account the impact of the concentrated DNA on the viscosity of the electrolyte solution and *ρ* is the density of the solution.

The Nernst-Planck constitutive equation for the mass flux is used in the equation of conservation of mass,

$$\frac{\partial c_i}{\partial t}+\mathbf{v}\cdot\nabla c_{\mathrm{i}}+\nabla\cdot\left(z_{\mathrm{i}}\omega_{\mathrm{i}}c_{\mathrm{i}}F\mathbf{E}\right)=\nabla\cdot D_{eff,\,\mathrm{i}}\nabla c_{\mathrm{i}} \tag{3}$$

to describe the behavior in solution of the electrolyte and buffer ions as well as the highly-charged, double-stranded DNA, and includes the effects of diffusion, convection and electrophoretic migration on strongly-coupled ionic transport. Here c_i is the concentration of the ith specie, *ω* is its absolute electrophoretic mobility, *z* is its valence, **E** is the electric field and *F* is Faraday's constant.

The Poisson equation,

$$\nabla\cdot\varepsilon_{\mathrm{r}}\varepsilon_0\nabla\mathbf{E}=\sum_{all\ species} z_{\mathrm{i}}Fc_{\mathrm{i}} \tag{4}$$

is used to calculate that portion of the electric field which arises as a result of the ζ-potential near the interior and exterior surfaces of the capillary. Although the induced electric field and double-layer electric field are parts of a common electric field, in practice we find it simpler and computationally more stable to calculate them separately and superimpose these two fields than to calculate them together.

The no slip condition is applied on all solid surfaces, all glass surfaces are assumed to have a constant ζ-potential, to be electrically insulating and to be impermeable to the ions and to the flow. Finally, a point at the far end of the reservoir is set to ground and the upstream end of the capillary is assumed to be insulated so that the net current across the capillary is zero.

Initially there is no flow anywhere, the low-conductivity dsDNA-containing sample fluid fills the entire reservoir and penetrates about 120 microns into the capillary while the rest of the capillary is filled with the high-conductivity eluent buffer. The applied pressure driving the flow from the capillary into the sample reservoir starts after 2 seconds and ramps from zero to full pressure in < 0.25 seconds. At the end of the focusing period, the applied pressure is ramped down to zero and held at zero for 2 seconds before the reverse pressure is applied.

5.2.2. Reagent and Buffer Preparation

A wide range of reservoir and running buffers were used in this work. The properties of these buffers, their shorthand abbreviations, their MRT buffer role (reservoir buffer or running buffer), and the corresponding figure numbers are listed in **Table 5.1**. TE buffer (10 mM Tris-HCl, 1 mM EDTA, pH 8.0) was purchased from Ambion. Sodium Chloride (NaCl) 5M solution was purchased from Amresco. Potasium Chloride (KCl) 8M solution was purchased from Sigma-Aldrich. Hydrochloric Acid (HCl, 35%) was purchased from Sigma-

Aldrich. All remaining buffer reagents (Bis-Tris, EACA, HEPES, and Tris) were purchased in dry form from Sigma-Aldrich and dissolved in filtered deionized water. Polyvinylpyrrolidione (molecular weight 360,000, Sigma-Aldrich) was prepared in TE buffer at 2% w/v.

5.2.3. Sample Preparation

For fluorescent microscope experiments, *Hind*III digested λ DNA (New England Biolabs, Inc.) was diluted to 10 ng/μL and stained with 40x or 100x dilution of PicoGreen (Thermo Fisher Scientific, Inc.) in 1 mM HEPES-Tris buffer. For SML-FSHS experiments, *Hind*III digested λ DNA was diluted to 5 ng/μL and stained with 1 μM TOTO-3 Iodide (Thermo Fisher Scientific, Inc.) in either water or buffer. The samples were either used at this concentration or further diluted into the sample buffer before each experiment. Alexa 647-NHS ester "free dye" was used as a control to normalize retention times between experiments. It was stored at a stock concentration of 1 μM in water and spiked into each sample at 500 pM or 100 pM concentration.

5.2.4. Fluorescent Micrograph and Video Collection

All fluorescent images were taken using an upright epifluorescent microscope (BX51, Olympus) with a 10x air objective (UPlanFl, Olympus). A 470 nm LED (ThorLabs) provided fluorescent excitation light. Fluorescent emission was collected with a CCD camera (Regita Exi, QCapture) with 100 or 500 ms exposure. Images were collected once per second using the MicroManager plugin for ImageJ.[125] ImageJ was used to assemble the images into movies at 10x speed.

5.2.5. Capillary Preparation and Separation Protocol

A 5 μm nominal inner diameter fused silica capillary (Polymicro Technologies, Molex) was cut to a total length of 120 cm. A short section of the polyimide coating was burned from the capillary to form a viewing window 90 cm from the inlet (capillary effective length) that served as the detection window for the size-based hydrodynamic separations following MRT preconcentration. The inlet and outlet of the capillary were housed in their own pressure injection chambers which contained either 100 μL (inlet) or 200 μL (outlet) of reservoir or running buffer.

Flow was driven through the capillary using an argon pressure source, which was regulated at each end of the capillary by separate LabVIEW-controlled precision pressure regulators. The capillary was first filled with the running buffer (see **Table 5.1**; e.g. 25 mM Tris-HCl, 2X EB, etc.) from the injection side. Pressure was stopped and the tube of injection buffer was replaced with a tube containing the stained DNA sample in the reservoir buffer (e.g. water, EB buffer, etc.). Then pressure was applied to the outlet pressure chamber to force counterflow from the capillary into the reservoir at a specified pressure and time. Immediately after the counterflow pressure was vented, 50 psi pressure was applied to the capillary inlet for 10 seconds to inject a concentrated sample plug. After the injection pressure was vented, the sample tube in the inlet chamber was replaced with 100 μL of running buffer. The inlet chamber was pressurized to 450 psi for the duration of the separation. Retention time is counted from the application of the separation pressure. Flow rates were calculated from the retention time of the free alexa dye marker and the effective capillary length. The capillary was always rinsed with running buffer at least once between each separation for at least 11 minutes (approximately 1.5 column volumes) before concentrating and separating a new sample.

5.2.6. Data Collection and Analysis

Single molecule detection was performed with the cylindrical illumination confocal spectroscopy platform described in Chapter 2. Briefly, the capillary viewing window was aligned within the platform's optical observation volume. A 640 nm laser diode at 8 mW power provided fluorescent excitation, and photon counts were collected from the avalanche photodiode detector in 0.1 ms bins using a custom LabVIEW program. Fluorescent bursts from single molecules were detected and counted using thresholding analysis. Single molecule bursts were counted in 0.5 or 1 second bins and plotted as a chromatogram. Peak areas were obtained by fitting the chromatograms to a series of Gaussian peaks. The area of each peak was used to calculate the total number of molecules *N* present of each separated fragment size.

The concentration factor C_F was calculated for each experiment by normalizing the results after concentration to a no-concentration control separation performed in the same running buffer. The calculation was performed individually for each fragment size using equation 5 below,

$$C_F = D_F \frac{N}{N_C} \tag{5}$$

where *N* and N_C refer to the number of counted molecules of a given fragment size after concentration and in the no concentration control, respectively. D_F is the dilution factor of the starting DNA sample concentration from the sample used for the control separation. SML-FSHS quantification repeatability and calculation of the concentration factor for MRT-SML-FSHS was found to be within 50% for experiments done on the same day, as shown in **Fig. 5.2**.

It should be noted that the rectangular aperture used to eliminate out-of-plane fluorescence limited the dimensions of the observation region to a 4 x 1 μm slit along the capillary length. Molecules near the wall of the 5 μm diameter capillary could have passed outside the observation volume without being detected, limiting the mass detection efficiency of single molecule counting. However, this should not impact the ratiometric calculation the concentration factor because the fraction of the number of counted molecules to the number of actual molecules for any given fragment size should be the same for all separations.

5.3. Identification of the Underlying Concentration Mechanism

We unintentionally discovered MRT while observing the interface of a capillary orifice filled with a high ionic strength running buffer surrounded by a reservoir containing DNA in a low ionic strength sample buffer (**Fig. 5.3**). When pressure was used to drive flow of the high ionic strength buffer out of the capillary, counter-intuitively, DNA within the reservoir migrated against the direction of flow and gathered into a highly concentrated bolus at the capillary orifice (**Fig. 5.3c**). This concentration occurred despite the absence of an applied electric field. Then, by simply reversing the flow direction, we saw that the concentrated sample plug could be injected into the capillary (**Fig. 5.3d**), enabling direct coupling with downstream analysis methods. Our initial experiments achieved DNA concentration factors of more than 100 fold and catalyzed follow-up efforts to determine the underlying mechanism and further increase concentration factors.

In order to identify the mechanisms driving MRT, we performed a series of preliminary experiments (**Table 5.2**) to test various experimental factors including the influence of capillary surface charge and the effect of buffer composition of both the running and sample buffers. Based on the migration behavior of the DNA, we postulated that the underlying mechanism was electrokinetic in nature. After ruling out the possibility of spurious electric fields from external power sources, we began to examine mechanisms that would give rise to an internally-generated, local electric field. Given that accumulation of

DNA seemed to occur in response to pressure-driven flow from the capillary into the reservoir, we initially hypothesized that a streaming potential was driving the migration. A streaming potential arises when an electrolyte flows through a channel (or capillary) with a charged surface.[126] To elucidate the importance of the streaming potential, we neutralized the negatively charged silica capillary with the addition of polyvinylpyrrolidione (PVP) to the running buffer, a technique commonly used in microfluidic applications to decrease electroosmotic flow (EOF).[127] If the streaming potential was responsible for the DNA concentration behavior, shielding the charges to reduce the streaming potential would result in a significant decrease or elimination of the concentration effect. Surprisingly, DNA migration and concentration persisted with the addition of 0.5% PVP. This finding was verified with the numerical simulation, in which we observed DNA concentration with both negatively charged and neutrally charged capillary walls. These results suggested that streaming potential does not play a significant role in MRT.

We then examined the importance of the buffer mismatch between the capillary and the reservoir. We first observed the concentration phenomenon when the high ionic strength buffer (100 mM Tris-HCl) filled the capillary and flowed into a low ionic buffer (1mm Tris-HEPES). When we used the same buffer for the running and reservoir buffers, DNA concentration did not occur (**Table 5.2**, rows 3 and 4). It also did not occur when we reversed the buffers so that the low conductivity buffer flowed into the high conductivity buffer (row 5). Even more surprisingly, DNA concentration did not occur when the capillary was filled with 100 mM Tris-HEPES running buffer and flowed into a reservoir of 1 mM Tris-HEPES (row 6). This suggested that the conditions necessary for DNA concentration to occur were dependent not only on the absolution difference in ionic strength between the capillary and the reservoir, but also on a mismatch in the diffusion coefficient (or mobility) between the anion and cation in the capillary buffer.

In parallel to these experiments, we performed a numerical simulation using COMSOL Multiphysics® to confirm the effect of these parameters and further probe the contributions of individual underlying forces (**Fig. 5.4**). Excellent qualitative agreement between the simulation (**Fig. 5.3**, bottom) and experiments (**Fig. 5.3**, top) were obtained, including the step of flow reversal and sample injection (**Fig. 5.3**d and h). From this, we eliminated what we felt was the most likely cause, the generation of a streaming potential, and instead determined that the development of an ion concentration gradient generates localized forces that propel DNA migration toward the capillary orifice.

5.4. Proposed Concentration Mechanism

The proposed mechanism is illustrated schematically in **Fig. 5.5a** along with supporting results from the simulation in **Fig. 5.5b**. Flow of the high ionic strength running buffer out of the capillary and into the low ionic strength reservoir buffer generates a concentration gradient of ions surrounding the capillary orifice. At a static interface, diffusion would quickly dissipate the concentration gradient; however, in our system, flow out of the capillary acts as a steady source of ions and the reservoir as a 3-dimensional and nearly infinitely large sink, allowing the system to quickly equilibrate to a sustainable ion gradient. The ions expelled from the capillary can then diffuse down their concentration gradient and into the reservoir. The slower migration of cations relative to their anion counterparts generates an induced electric field (rainbow contour in **Fig. 5.5b**) that reaches a maximum less than 5 μm from the capillary orifice and decreases as it spans more than 50 μm into the reservoir (**Fig. 5.6**). Remarkably, we find that this electric field generates quickly (under 5 seconds), persists for long time periods (at least 45 minutes), and can reach a maximum magnitude approaching 40 V/cm. This resulting electrophoretic force drives the negatively charged DNA molecules in the reservoir to migrate against the ion concentration gradient toward the capillary orifice (**Fig. 5.5b**, green arrows) to the region at which it is balanced by the hydrodynamic force from the capillary flow, causing the DNA to accumulate into a concentrated bolus. The hydrodynamic force acts to disrupt the concentrated DNA while the electrophoretic force acts as a restoring force. Interestingly, the highly localized nature of these forces means that they are not spatially uniform even within the bolus region, causing the DNA to recirculate within the bolus (**Fig. 5.5b**, red arrows). Flow out of the capillary into the large reservoir also increases the size of the buffer interface region, increasing the volume over which the DNA can concentrate and allowing for the generation of even higher concentration factors.

Solute concentration gradients in the absence of other external forces were first seen to effect migration of colloid particles as early as 1947.[128] This phenomenon, termed diffusiophoresis, has since been well studied both theoretically and experimentally within the colloidal research community[129-134], but only recently has been expanded to manipulate biological species including DNA[135-138], proteins[138-141] and cells[138, 142]. MRT invokes the same forces to establish an ion diffusion-generated electric field, but utilizes counterflow from a micro-orifice to generate a stable and highly-localized ion gradient, increase ion flux, provide a counterbalancing force to DNA migration, and control the shape and location of the DNA focusing region. To our knowledge, diffusiophoresis alone has not been shown to generate the large concentration factors or high stability over time achieved with our flow-based method.

5.5. Integrated MRT-SML-FSHS Platform

To quantify the concentration factors experimentally, we integrated MRT with SML-FSHS, a single molecule separation platform that also operates in the absence of an applied electric field. The combined platform, illustrated schematically in **Fig. 5.7**, uses only pressure to control the direction, speed, and duration of flow during the sequential steps of MRT preconcentration, sample injection, and free solution hydrodynamic separation steps. Cylindrical illumination confocal spectroscopy (CICS) is used to individually detect each size separated DNA molecule by its discrete fluorescent burst.[53] The single molecule chromatogram generated by summing these single molecule bursts enables quantification for each DNA fragment size by absolute number of molecules rather than arbitrary fluorescence units (see Methods). This single molecule analysis not only enhances SML-FSHS detection sensitivity, but it also improves quantification accuracy compared to bulk fluorescence intensity through direct counting and by minimizing the impact of fluorescence artifacts (**Fig. 5.8**).[32, 48, 143]

5.6. Effects of Flow Parameters on Concentration Enhancement

We first characterized the effects of the counterflow rate (backpressure) on the DNA concentration enhancement by analyzing TOTO-3 stained *Hind*III digested λ DNA with 25 mM Tris-HCl as the running buffer and water as the low ionic strength reservoir buffer. In **Fig. 5.9a**, we report the concentration factor of each DNA fragment after 30 seconds of MRT at a range of backpressures. The concentration factor increased from 0 to 50 psi. At 50 psi, a concentration enhancement greater than 10 fold is achieved for all DNA fragments. This agreed with our initial observations, in which DNA concentrated in response to pressure-driven flow. Above 50 psi, the concentration factor decreased with increasing flow rates. This observation suggests an optimal pressure where low flow rates enhance the bolus formation, but high flow rates begin to disrupt it. We saw this visually manifest in two forms: (1) the center of the bolus was blown out to form a donut-shaped concentration region, which grows with increasing backpressure (**Fig. 5.10**) or, infrequently, (2) the concentration bolus became unstable and was dislodged from the capillary. Donut-shaped concentration was also observed in the simulation (**Fig. 5.11**).

Next, we characterized the effect of concentration time at the optimal backpressure of 50 psi (**Fig. 5.9b**). The concentration factor increased with time for all DNA species. At 25 minutes, all DNA fragments were concentrated more than 2000 fold. Minor size-dependent concentration bias was seen after 25 minutes; the concentration factor of the largest molecules (27 and 23 kbp) was approximately 4 fold higher than that of the smallest (2.3 and 2.0 kbp). This small bias could be related to the variety of forces operating in MRT: purely electrophoretic techniques do not typically exhibit a substantial concentration size-bias for this DNA size range[144, 145], and diffusiophoretic migration of colloid particles can be size-dependent or -independent depending on the parameter space[134]. However, the bias is minimal compared to the overall 10^3 concentration factors and could also be a result of fluorescence artifacts that cause undercounting of small DNA molecules (**Fig. 5.8**).

Beyond enhancing sensitivity, MRT could also simplify SML-FSHS operation by eliminating the sample plug injection. Typically, sample plugs are generated by sequentially injecting running buffer, sample, and elution buffer. However, MRT generates a very small bolus of highly concentrated DNA at the capillary inlet that can be injected and separated without switching to elution buffer. The DNA sample itself is so dilute that it can act as an elution buffer. We demonstrated the feasibility of this single-step separation technique by preconcentrating the sample ~2000 fold prior to a continuous injection and separation. Minimal loss in resolution was seen compared to the traditional injection scheme (**Fig. 5.12**).

5.7. Effects of Buffer Ions on Concentration Enhancement

The mechanistic resemblance to diffusiophoresis led us to investigate the potential contribution of a second chemiphoretic mechanism in which favorable interactions between positively charged cations and the negatively charged DNA molecules could also drive DNA migration (**Fig. 5.5**). Though not accounted for in our numerical simulation, the chemiphoretic component has been suggested to play a dominant role in diffusiophoresis in some circumstances.[146]

To determine the relative contributions of electrophoresis and chemiphoresis, we designed a buffer system where we could hold the chemiphoretic component relatively constant while modulating the electrophoretic component. In these experiments, a low ionic strength base buffer was used in both the reservoir and running buffers (see Experimental Details section). This "EB buffer" base consists of a weak acid (ε-aminocaproic acid, EACA) and a weak base (Bis-Tris), which titrate each other while remaining > 90% neutral and maintaining a high buffering capacity.[65] Three capillary running buffers were created with low, medium, and high expected electrophoretic components through the addition of 9 mM KCl, NaCl, and HCl, respectively. These species completely dissociate in solution and form an ion concentration gradient across the capillary orifice. With Cl^- and EB concentrations held constant, these running buffers therefore allow us to probe the effect of cation diffusivity on the size of the induced electrophoretic field and the DNA concentration factor.

For the low electrophoretic force KCl buffer (**Fig. 5.13**), virtually no concentration enhancement was observed in either simulation (striped) or experiment (solid). Since K^+ and Cl^- have very similar diffusivities, their diffusive fluxes are reported in the numerical simulation to be similar (**Fig. 5.14a**), minimizing the electrophoretic component (**Fig.**

5.14d). In this condition, any DNA concentration would be largely due to chemiphoresis. However, the low concentration factor for the KCl case suggests that chemiphoresis alone does not significantly induce DNA migration in our system.

For the medium electrophoretic force NaCl buffer, a DNA concentration factor of ~10 fold was seen in both the simulation and SML-FSHS experiment (**Fig. 5.13**). Na^+ has a lower diffusivity than Cl^- ($K^+ \approx Cl^- > Na^+$). This results in a lower diffusive flux (**Fig. 5.14b**) and an induced electric field reaching 15 V/cm—more than 3 fold larger than that generated with KCl (**Fig. 5.14e**). These results suggest that only the electrophoretic component is the major contributor to MRT concentration factor.

For the high electrophoretic force HCl buffer, concentration factors greater than 100 fold were achieved (**Fig. 5.13**). H^+ has the highest diffusivity of all three cations ($H^+ >> K^+ > Na^+$). However, reactions with water and the buffering species (EACA and Bis-Tris) effectively scavenge the free H^+, yielding H_3O^+ and Bis-Tris$^+$. At pH 7.0, Bis-Tris$^+$ holds most of the positive charges and becomes the majority cation. The diffusive flux of Bis-Tris+ in this buffer is ~10 fold larger than its flux in the KCl and NaCl cases, but still 3 and 4 fold smaller than the flux of Na^+ and K^+, respectively (**Fig. 5.14a-c**). The more than 4 fold difference in flux between Cl- and Bis-Tris+ generates the largest induced electric field (**Fig. 5.14f**), and consequently the largest DNA concentration factors. A comparison of the centerline electric potential reached using each of these buffer sstems is shown in **Fig. 5.15**.

We then used the EB buffer system to examine the effect of the sample buffer composition. **Fig. 5.16** shows single molecule separations performed on DNA in EB buffer with no MRT, DNA in DI water with MRT, and DNA in EB buffer with MRT. The DNA in DI water achieved over 1000 fold concentration enhancement after 12 min of preconcentration at 100 psi (**Fig 5.16b**). In contrast, the DNA in EB buffer required 12 min of preconcentration at 400 psi to achieve the same 1000 fold enhancement (**Fig 5.16c**). We hypothesize that the concentration gradient of EB buffer into a water reservoir results in a higher diffusive flux of the Bis-Tris$^+$ ions, resulting in a lower optimal flow rate. Simultaneously, the higher conductivity of the EB reservoir compared to water could also affect the magnitude and span of the electric field, which is compensated with a higher flow rate. A comparison of the separation resolution between the three chromatograms in Fig. 7 shows < 7% CV, verifying that MRT preconcentration does not negatively affect the separation efficiency. Additional control experiments (**Figs. 5.17 and 5.18**) validate that the high concentration factors require both counterflow and the running and reservoir buffer mismatch.

5.8. Exceeding 10,000-fold DNA Preconcentration

Finally, we attempted to maximize the DNA concentration factor by integrating all of the previously optimized conditions (**Fig. 5.19**). By switching from the initial Tris-HCl buffer to an optimized EB-HCl buffer, we observed a 2 fold increase in the optimal counterflow rate as well as a 2-3 fold increase in the concentration factors within the same concentration time. The EB-HCl buffer generates a larger electrophoretic field than the Tris-HCl buffer which allows the DNA migration to overcome higher counterflow velocities. We hypothesize two mechanisms that could lead to this result. First, faster DNA migration due to larger electrophoretic fields in the EB-HCl buffer enables the DNA migration to overcome higher counterflow velocities. Second, the higher counterflow rate expands the buffer interface and acts to attract DNA from a larger sample volume. Then by increasing concentration time from 10 min to 45 minutes, we were able to achieve concentration factors exceeding 10,000 fold (**Fig. 5.19**). While the results from the numerical simulation (striped bars) in **Fig. 5.19** show higher deviation from experiment (solid bars) than those in

Fig. 5.13, they do present the same trends as the experimental results with the same experimental conditions achieving the highest concentration factors. The > 10^4 concentration factors achieved experimentally increased the effective sample screening volume from ~45 pL (injected volume) to ~0.5 μL (preconcentrated volume containing the same number of DNA molecules), enabling SML-FSHS analysis from a starting sample concentration of only 150 aM (< 100 copies per μL). On average, we counted ~500 molecules per fragment size, well above a projected limit of detection (S/N = 3) of ~40-120 molecules, which would correspond to a sample concentration of 10-50 aM. In our previous work without preconcentration, we projected SML-FSHS limit of detection to be ~3.5 pM, which was a 2-3 orders of magnitude improvement over existing methods.[32] The addition of MRT improves SML-FSHS sensitivity by an additional 5-6 orders of magnitude, making it among the most sensitive amplification-free, size-based analytical methods.

5.9. Conclusion

In this chapter, we demonstrated a simple, unexpected method to concentrate DNA at a discontinuous buffer interface without an applied electric field. In this technique, based on the migratory phenomenon that we call Molecular Rheotaxis, DNA in a low ionic strength buffer reservoir migrates toward the outlet of a capillary dispelling a high ionic strength buffer driven by a pressure gradient. Complementary numerical and experimental approaches were used to develop the proposed underlying mechanism, which involves an ion gradient-induced electric field (as in diffusiophoresis) and a counteracting microfluidic flow to both generate the ion gradient and focus the DNA. Though diffusiophoresis does enable species specific manipulation over macroscopic length scales in a non-contact manner, we surmise that the slow adoption of diffusiophoresis is due to the challenge of establishing a stable solute concentration gradient for extended time periods.[131] To overcome this challenge, researchers have used semi-permeable membranes[130, 139], co-flow microfluidic devices[147], reactive surfaces[148-151], thermal gradients[142, 152, 153], and microdevices with flow channel reservoirs[134, 135, 142, 154]. In our technique, pressure-driven flow of a high ionic strength buffer out of the capillary and into a low ionic strength buffer reservoir generates a highly local but stable ion concentration gradient and induced electric field that is able to scavenge DNA from the reservoir for extended time periods. The pressure-driven flow also provides an additional hydrodynamic force acting to balance the induced electrophoretic migration of the DNA. DNA then accumulates into a highly concentrated region surrounding the capillary orifice.

Through optimization of the pressure, time, and buffer conditions, we have demonstrated concentration factors approaching 5 orders of magnitude, comparable to traditional DNA preconcentration methods such as FASS and ITP. In both FASS and ITP, a buffer mismatch is used to manipulate an externally applied electric field to cause DNA to preferentially accumulate at the interface.[155, 156] DNA analysis with FASS-CE, ITP-CE, and related electrokinetic platforms can boast limits of detection in the range of low pM to tens of fM.[113, 157, 158] In our technique, the electric field is generated internally via pressure-driven flow and diffusion, eliminating the need for an external input. The coupled MRT-SML-FSHS platform has a limit of detection approaching tens of aM, a 3-5 orders of magnitude improvement over traditional electrokinetic platforms, and represents a truly electrode-free platform for highly sensitive and quantitative DNA separation and sizing.

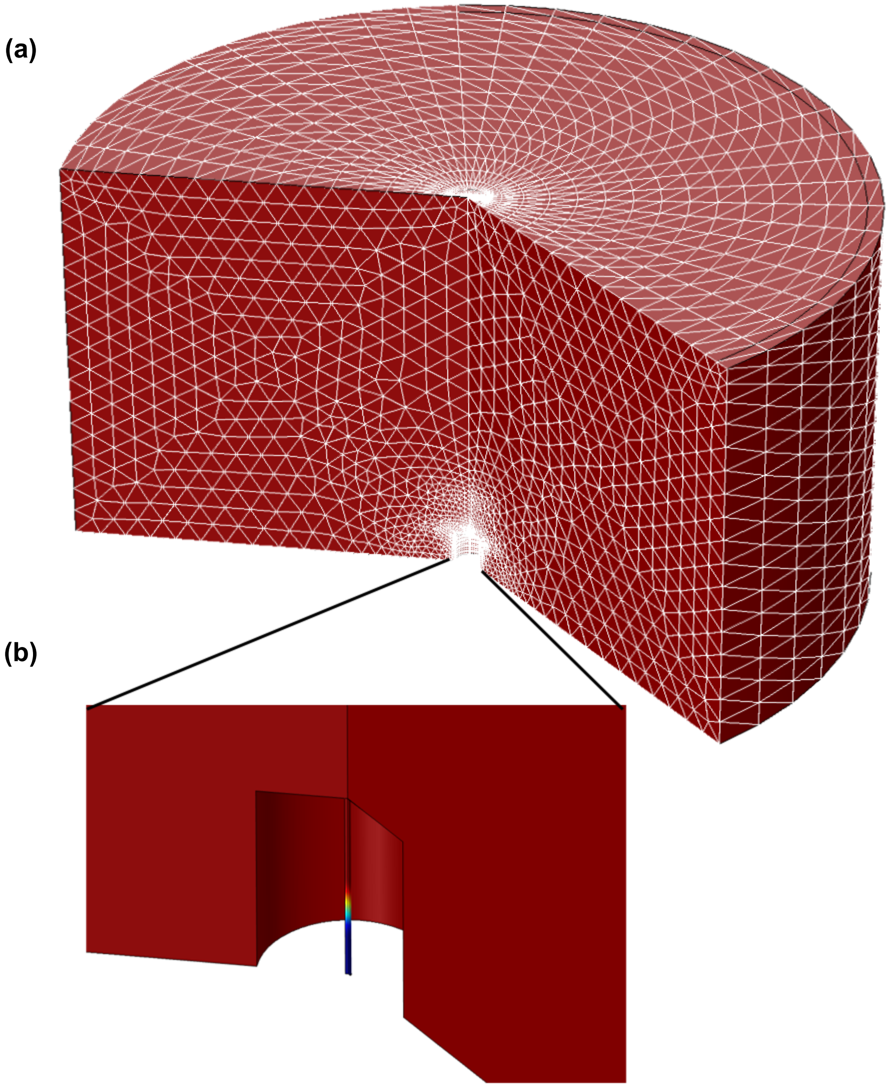
(a)
(b)

Figure 5.1. Model geometry

(a) The axisymmetric domain used in the COMSOL simulation in this paper consists of a 5 μl reservoir shaped like a right cylinder with the tip of a capillary inserted 150 μm into the reservoir. The mesh size is densest near the capillary orifice and increases in size towards the edges of the reservoir. A very coarse mesh is shown for the purposes of illustration. (b) The inset shows the capillary lumen (the fused silica is not part of the model geometry and is not shown) along with the initial distribution of the dsDNA (red) in the capillary at t=0. Reprinted from ref [54].

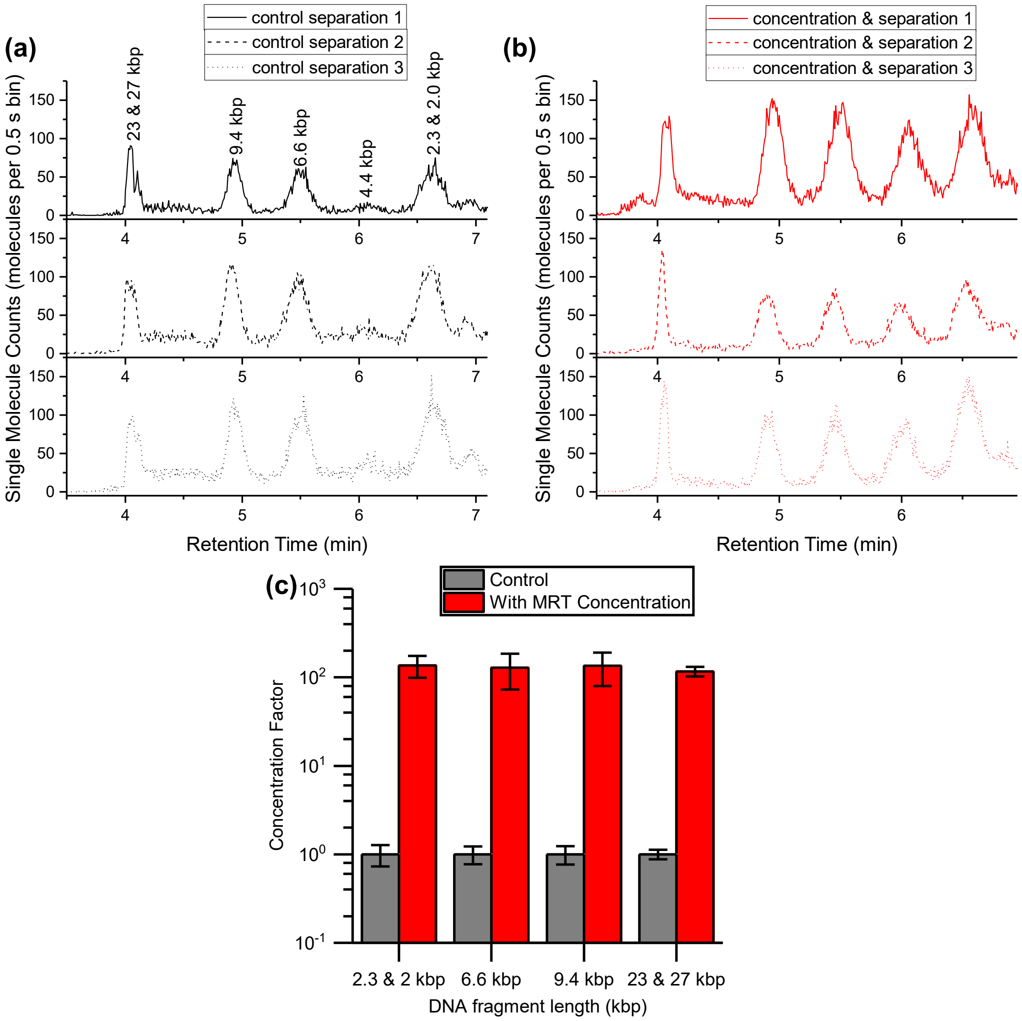
(a)
control separation 1
control separation 2
control separation 3
23 & 27 kbp
9.4 kbp
6.6 kbp
4.4 kbp
2.3 & 2.0 kbp
Single Molecule Counts (molecules per 0.5 s bin)
0
50
100
150
4
5
6
7
Retention Time (min)
(b)
concentration & separation 1
concentration & separation 2
concentration & separation 3
Single Molecule Counts (molecules per 0.5 s bin)
0
50
100
150
4
5
6
Retention Time (min)
(c)
Control
With MRT Concentration
Concentration Factor
10^{-1}
10^{0}
10^{1}
10^{2}
10^{3}
2.3 & 2 kbp
6.6 kbp
9.4 kbp
23 & 27 kbp
DNA fragment length (kbp)

Figure 5.2. Repeatability of SML-FSHS and MRT-SML-FSHS quantification

In (a), SML-FSHS of the same sample is repeated three times. In (b), a 100x diluted sample is concentrated for 2 min at 100 psi before being separated under the same conditions. These chromatograms are analyzed to calculate the average concentration factors for each fragment size, plotted in (c), with error bars representing +/-1 standard deviation. On a single day, coefficient of variation between MRT-SML-FSHS was < 50%, (within an order of magnitude). We did observe larger variation over experiments performed on different days. We attribute this to changes in environmental conditions that we could not control (e.g. temperature, humidity), which appear to affect the concentration enhancement. Reprinted from ref [54].

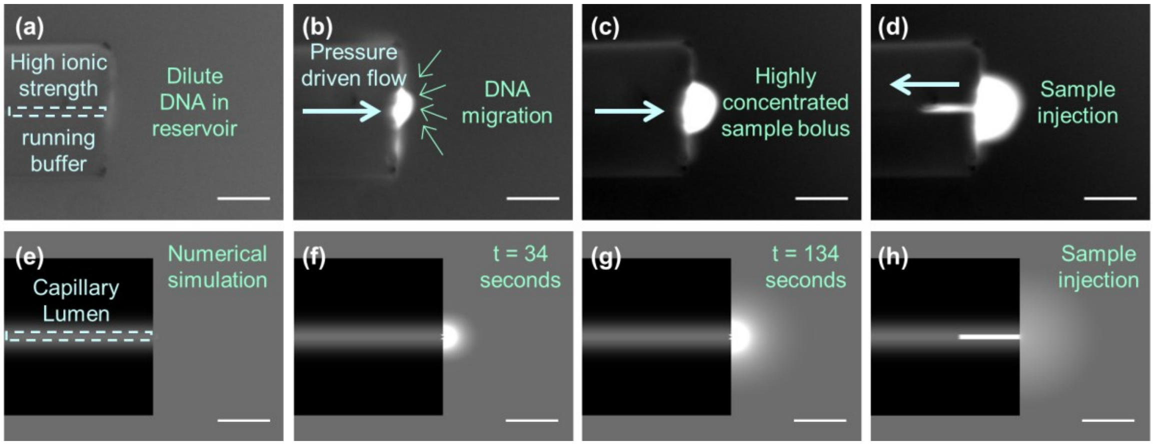
(a)
High ionic strength
running buffer
Dilute DNA in reservoir
(b)
Pressure driven flow
DNA migration
(c)
Highly concentrated sample bolus
(d)
Sample injection
(e)
Capillary Lumen
Numerical simulation
(f)
t = 34 seconds
(g)
t = 134 seconds
(h)
Sample injection

Figure 5.3. DNA preconcentration and injection into a microcapillary

(a) – (c) Snapshots capture DNA preconcentration at the outlet of a 5 μm inner diameter microcapillary when pressure is applied to drive flow of a high ionic strength solution out of the capillary and into the low concentration reservoir. (d) The bolus of concentrated DNA can be injected into the capillary by quickly reversing the flow direction. (e) – (h) The numerical simulation qualitatively captures the behavior of the DNA molecules in response to pressure-driven flow and the imposed buffer mismatch at the 5 μm capillary outlet. Scale bars are 50 μm. Reprinted from ref [54].

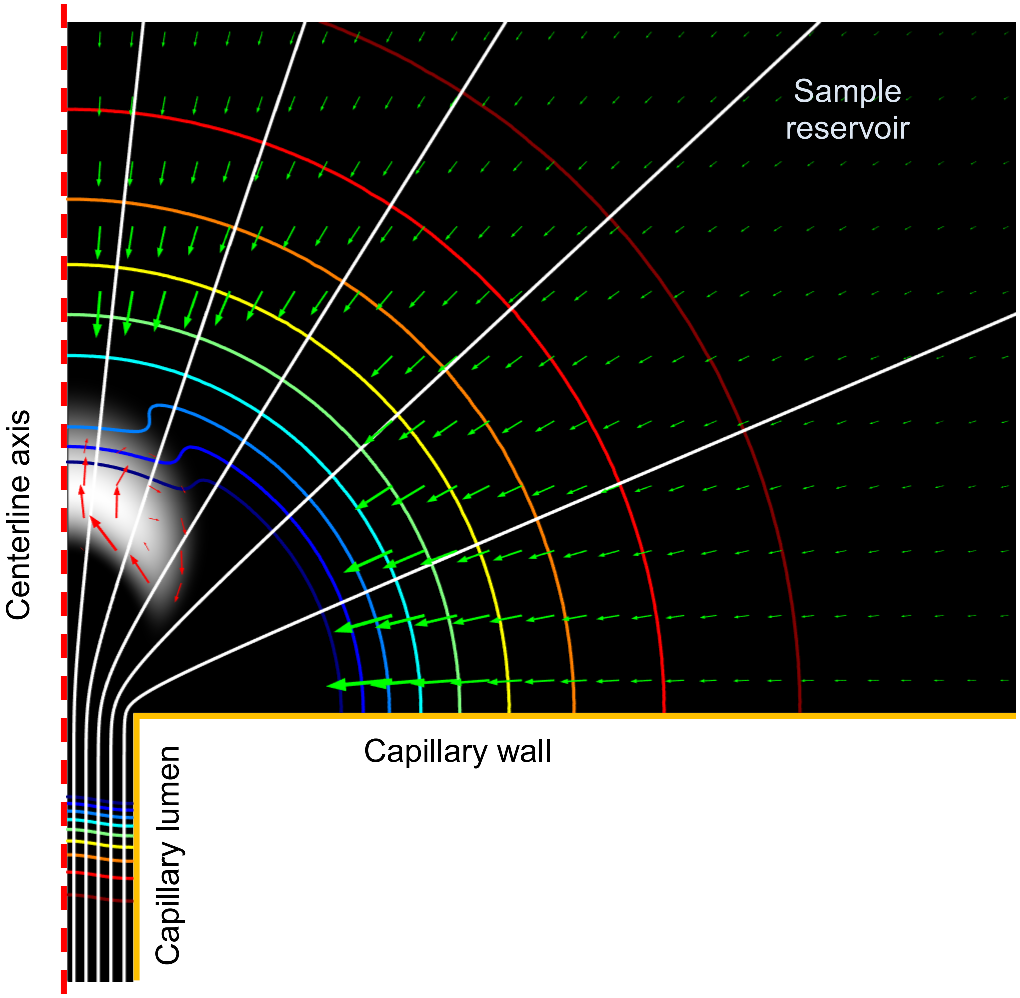
Sample reservoir
Centerline axis
Capillary wall
Capillary lumen

Figure 5.4. Flow streamlines, electric field lines, DNA migration vectors, and DNA concentration heatmap during MRT preconcentration

This image was produced with the simulation and used to generate Fig. 2b within the main text. The dotted red line indicates the centerline of the capillary and the gold lines indicate the walls of the fused silica capillary. The simulation conditions: sample buffer is water and the elution buffer is 2X EB + 18 mM HCl. Counterflow is applied to the sample for 45 minutes at 100 psi. The flow streamlines (white) radiate from the capillary orifice as expected. The electric field (multicolored) also radiates from the capillary orifice but is distorted by the highly concentrated DNA bolus (center). DNA migration is affected by both the electric field and the fluid flow, causing most of the DNA to enter the concentration bolus from near the capillary surface (green arrows). This force balance also causes the recirculating flow pattern of the DNA within the concentrated bolus (red arrows). Reprinted from ref [54].

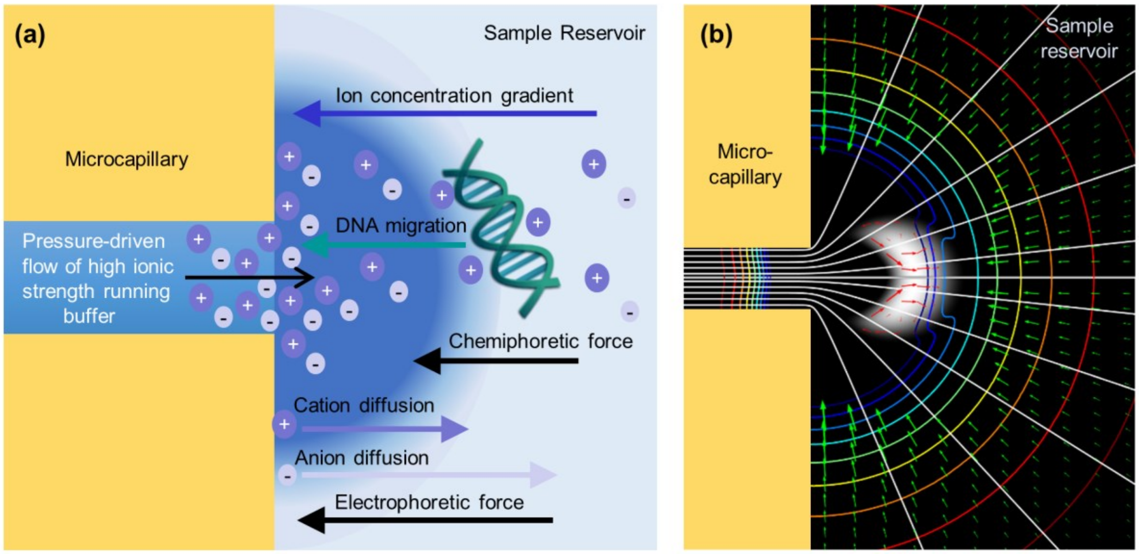
(a)
Microcapillary
Sample Reservoir
Ion concentration gradient
DNA migration
Pressure-driven flow of high ionic strength running buffer
Chemiphoretic force
Cation diffusion
Anion diffusion
Electrophoretic force
(b)
Micro-capillary
Sample reservoir

Figure 5.5. Mechanism of DNA Molecular Rheotaxis

(a) Schematic of the underlying mechanism of MRT. Pressure-driven flow drives the high ionic strength running buffer out of the capillary into the low ionic strength reservoir buffer. This forms a concentration gradient of ions surrounding the capillary orifice. The cations and anions migrate down their concentration gradients per their individual diffusivities. If anions diffuse faster than the cations, and induced electric field is generated that causes DNA to migrate toward the higher concentration of ions at the capillary orifice. Simultaneously, positive interactions between negatively charged DNA and cations can induce a chemiphoretic DNA migration towards the higher cation concentration near the capillary. (b) Results from the simulation show that flow out of the capillary (white streamlines emanating from microcapillary) is accompanied by an induced electric field (concentric rainbow contour lines) and results in DNA accumulation in a bolus near the capillary orifice (white shading). The direction and magnitude of DNA flux from the reservoir toward the bolus is shown in green arrows and with red arrows within the bolus. The original image was mirrored across the centerline to view the whole capillary (for the original figure, see **Fig. 5.4**). Reprinted from ref [54].

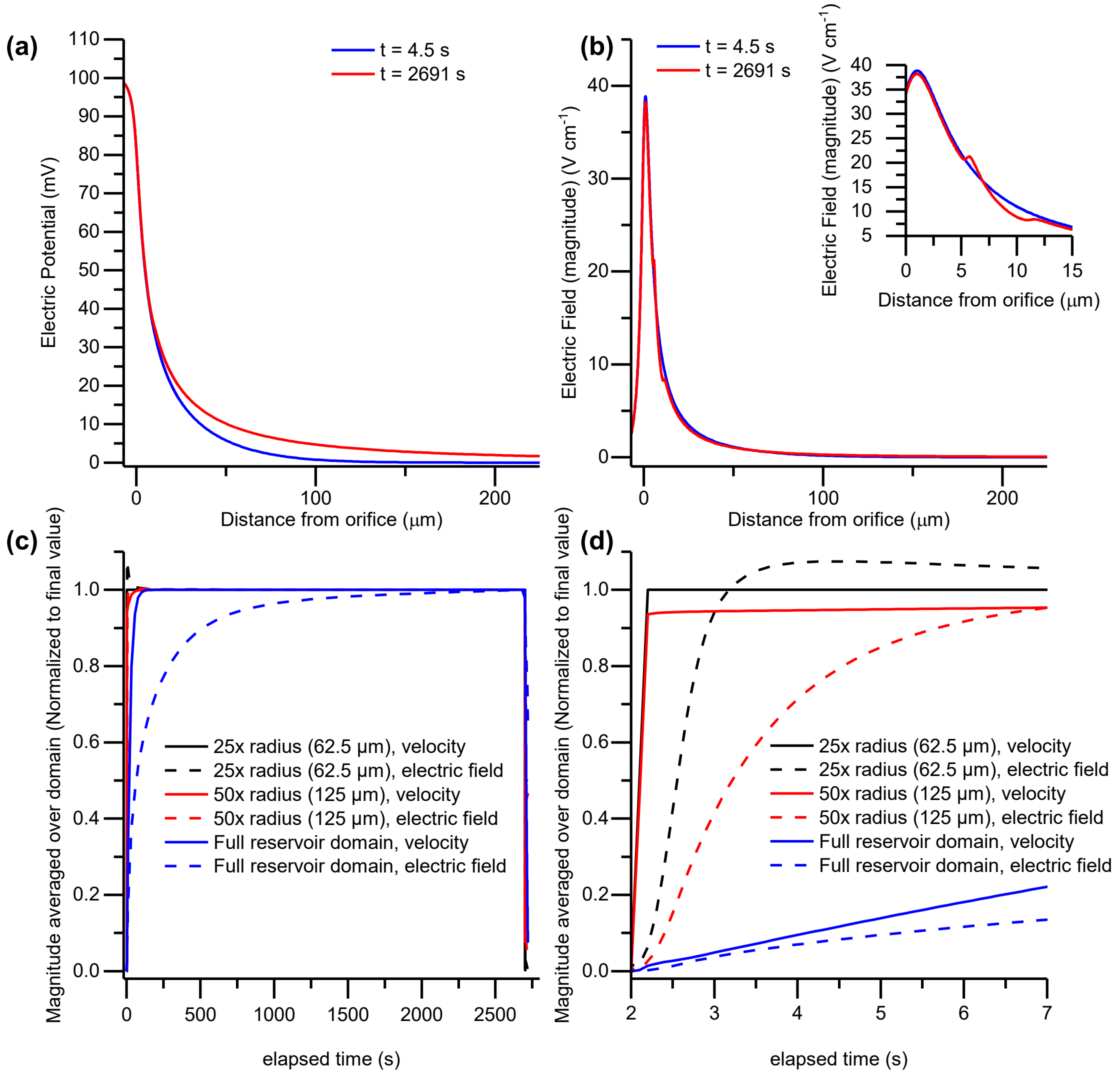
(a)
Electric Potential (mV)
Distance from orifice (μm)
t = 4.5 s
t = 2691 s
(b)
Electric Field (magnitude) (V cm^{-1})
Distance from orifice (μm)
t = 4.5 s
t = 2691 s
(c)
Magnitude averaged over domain (Normalized to final value)
elapsed time (s)
25x radius (62.5 μm), velocity
25x radius (62.5 μm), electric field
50x radius (125 μm), velocity
50x radius (125 μm), electric field
Full reservoir domain, velocity
Full reservoir domain, electric field
(d)
Magnitude averaged over domain (Normalized to final value)
elapsed time (s)
25x radius (62.5 μm), velocity
25x radius (62.5 μm), electric field
50x radius (125 μm), velocity
50x radius (125 μm), electric field
Full reservoir domain, velocity
Full reservoir domain, electric field

Figure 5.6. Responsivity and stability of fluid flow and induced electric field

The simulation conditions: sample buffer is water and the elution buffer is 2X EB + 18 mM HCl. Counterflow is applied to the sample for 45 minutes at 100 psi. Plots of the centerline (a) electric potential and (b) electric field at the beginning of fully developed flow (4.5 s), and at a late time point just before injection (2691 s) indicate that the induced electric field establishes quickly and is generally stable with time, with only minor changes observed to both curves over nearly 45 minutes of counterflow. The electric potential extends farther into the reservoir, but the electric field shape does not change significantly with time. The concentrated DNA bolus minorly distorts the electric field near the capillary inlet (inset), but this local field distortion does not affect the global field shape. Domain-averaged magnitude values of the velocity (solid) and electric field (dashed) are plotted over (c) the full concentration period and (d) the first 5 seconds of concentration. These values were computed over 3 domain sizes: 25x the capillary radius (black), 50x the capillary radius (red), and the full reservoir domain (blue), and normalized to the values at the final time point of applied pressure. Over the full reservoir domain, it takes ~50 s for the fluid flow to stabilize, and the electric field continues to change with time. This is likely due to the low volumetric flow rate (on the order of pL/s) that limits the speed at which the ions can span the full 5 μL reservoir region. However, the bolus concentration region is situated within 25 μm of the capillary orifice (inset of (b)) and is thus contained within a much smaller domain. Within the 62.5 μm domain, the velocity and the electric field stabilize much more quickly: the velocity curve closely follows the imposed pressure ramp rate, and the electric field reaches its maximum with only ~1s lag. The remainder of the reservoir serves as the sink, allowing the field within the bolus region to remain relatively stable. Reprinted from ref [54].

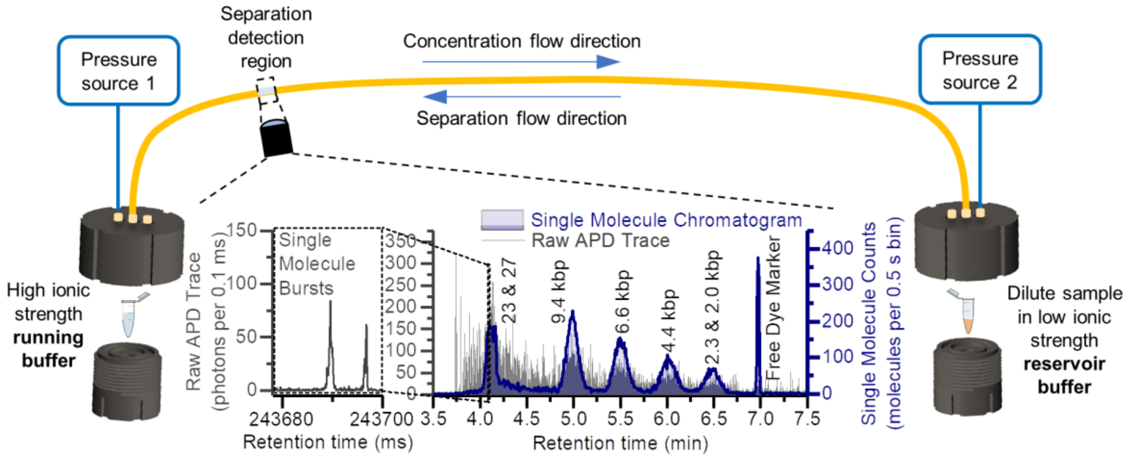
Separation detection region
Concentration flow direction
Separation flow direction
Pressure source 1
Pressure source 2
High ionic strength **running buffer**
Dilute sample in low ionic strength **reservoir buffer**
Single Molecule Chromatogram
Raw APD Trace
Single Molecule Bursts
Raw APD Trace (photons per 0.1 ms)
150
100
50
0
243680
243700
Retention time (ms)
350
300
250
200
150
100
50
0
3.5
4.0
4.5
5.0
5.5
6.0
6.5
7.0
7.5
Retention time (min)
23 & 27
9.4 kbp
6.6 kbp
4.4 kbp
2.3 & 2.0 kbp
Free Dye Marker
400
300
200
100
0
Single Molecule Counts (molecules per 0.5 s bin)

Figure 5.7. Coupled MRT-SML-FSHS platform

Each end of a long microcapillary is placed into its own individually controlled pressure chamber to enable precise control over the direction and speed of fluid flow. Concentration occurs by applying positive pressure to the running buffer pressure chamber with Pressure source 1, and sample injection and separation occur with positive pressure applied to the opposite end of the capillary with Pressure Source 2. The CICS observation volume is aligned with the detection region to enable detection of single DNA molecules (grey, background), which are counted to generate a single molecule chromatogram (navy, shaded foreground). This example chromatogram was generated after performing 100x MRT preconcentration and free solution separation of *Hind*III digested λ DNA. Reprinted from ref [54].

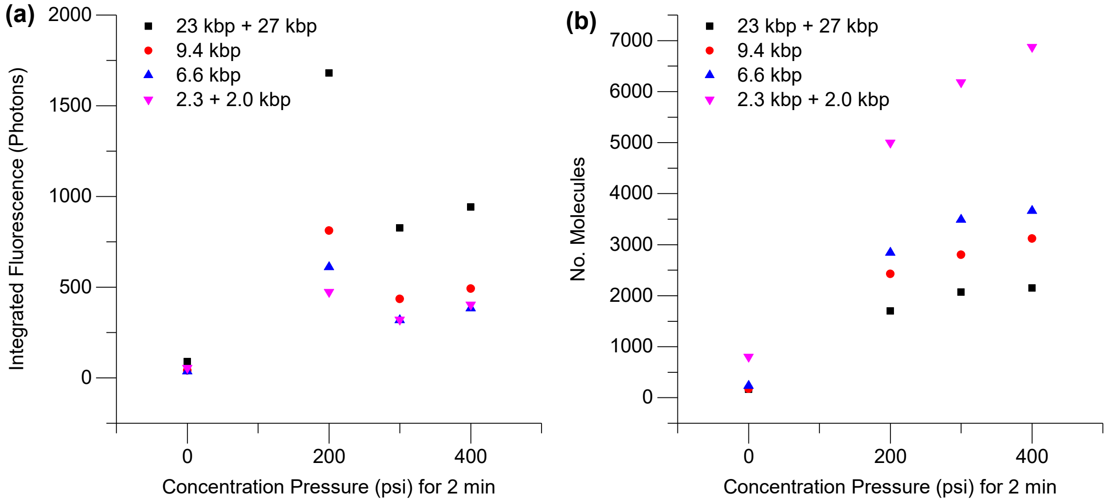
(a)
2000
1500
1000
500
0
Integrated Fluorescence (Photons)
0
200
400
Concentration Pressure (psi) for 2 min
■ 23 kbp + 27 kbp
● 9.4 kbp
▲ 6.6 kbp
▼ 2.3 + 2.0 kbp
(b)
7000
6000
5000
4000
3000
2000
1000
0
No. Molecules
0
200
400
Concentration Pressure (psi) for 2 min
■ 23 kbp + 27 kbp
● 9.4 kbp
▲ 6.6 kbp
▼ 2.3 kbp + 2.0 kbp

Figure 5.8. Concentration factor quantification comparison of fluorescence and single molecule counting

Single molecule counting more accurately measures DNA concentration than integration of fluorescence intensity.The sample buffer is 2X EB and the elution buffer is 2X EB + 18 mM HCl. Counterflow is applied to the sample for 2 minutes over a range of counterflow pressures. The raw data traces collected from each separation are then analyzed in terms of both (a) total fluorescence and (b) single molecule counting. Although fluorescence integration analysis suggests that the highest concentration factors are achieved at 200 psi backpressure, single molecule counting reveals that the DNA molecules continue to concentrate at 300 and 400 psi backpressure. This suggests that fluorescence intensity is also affected by the preconcentration technique, and thus integrating fluorescence intensity alone may not accurately represent the actual DNA concentration factors. This is likely due to the salt dependence of intercalating dye binding kinetics.[143, 159, 160] For this reason, we did not use fluorescence intensity to calculate concentration factors and limited the experimental conditions to concentrations that allow single molecule counting. Reprinted from ref [54].

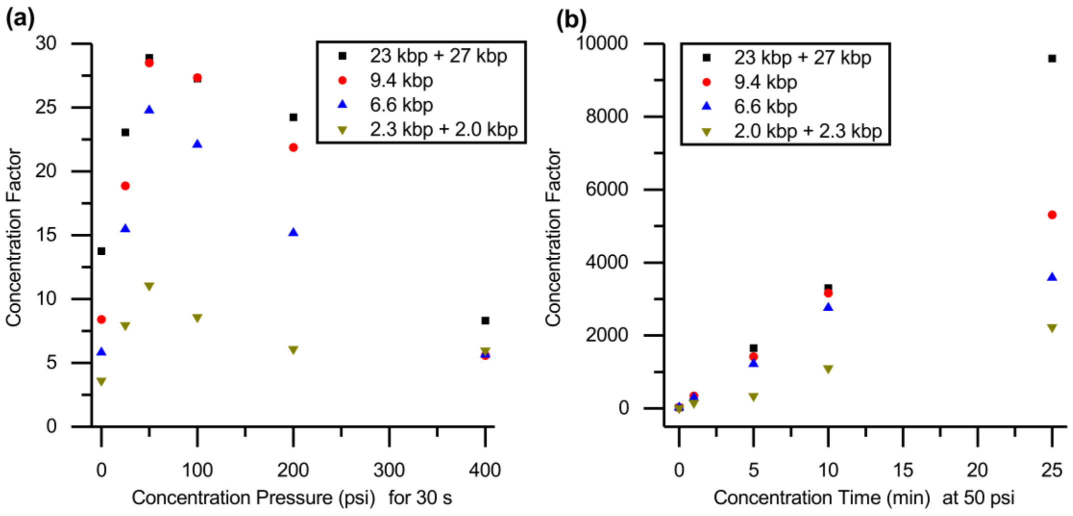
(a)
Concentration Factor
0
5
10
15
20
25
30
0
100
200
300
400
Concentration Pressure (psi) for 30 s
■ 23 kbp + 27 kbp
● 9.4 kbp
▲ 6.6 kbp
▼ 2.3 kbp + 2.0 kbp
(b)
Concentration Factor
0
2000
4000
6000
8000
10000
0
5
10
15
20
25
Concentration Time (min) at 50 psi
■ 23 kbp + 27 kbp
● 9.4 kbp
▲ 6.6 kbp
▼ 2.0 kbp + 2.3 kbp

Figure 5.9. Effects of pressure and time on the concentration enhancement

(a) High concentration running buffer (25 mM Tris-HCl buffer) is pumped through the capillary (5 µm nominal inner diameter, 150 µm outer diameter, 120 cm total length) into the reservoir (λ DNA *Hind*III digest in DI water) for 30 seconds at varying pressures. The highest concentration factor occurs at 50 psi pressure. (b) Using the optimal 50 psi concentration pressure, concentration time is varied from 30 seconds to 25 minutes. The concentration factor increases with time for all DNA species. Reprinted from ref [54].

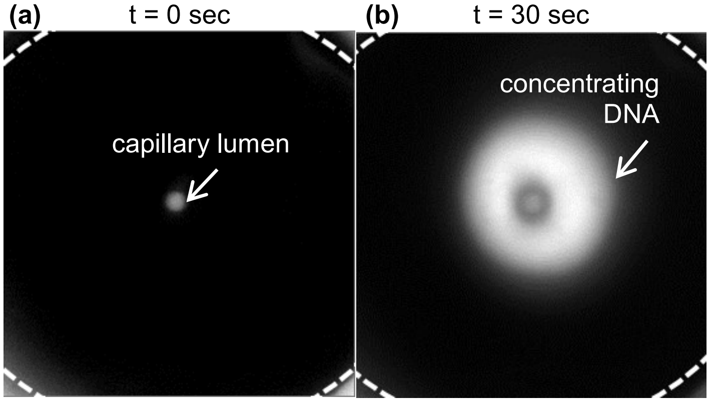
(a)
t = 0 sec
capillary lumen
(b)
t = 30 sec
concentrating DNA

Figure 5.10. Donut-shaped concentration bolus at high flow rates

At higher flow rates, the concentration bolus forms a doughnut shape surrounding the capillary outlet. The microcapillary with a 10 μm lumen diameter and length of 50 cm is filled with 100 mM Tris-HCl buffer. 10 ng/μL *Hind*III digested lambda DNA stained with PicoGreen is surrounding the capillary. 120 psi pressure is applied to the distal capillary end to initiate MRT DNA preconcentration. MRT is not sufficient to overcome the high flow rate exiting the capillary. Instead, the DNA molecules collect around the edges of the capillary lumen, forming a doughnut shaped concentration bolus. Reprinted from ref [54].

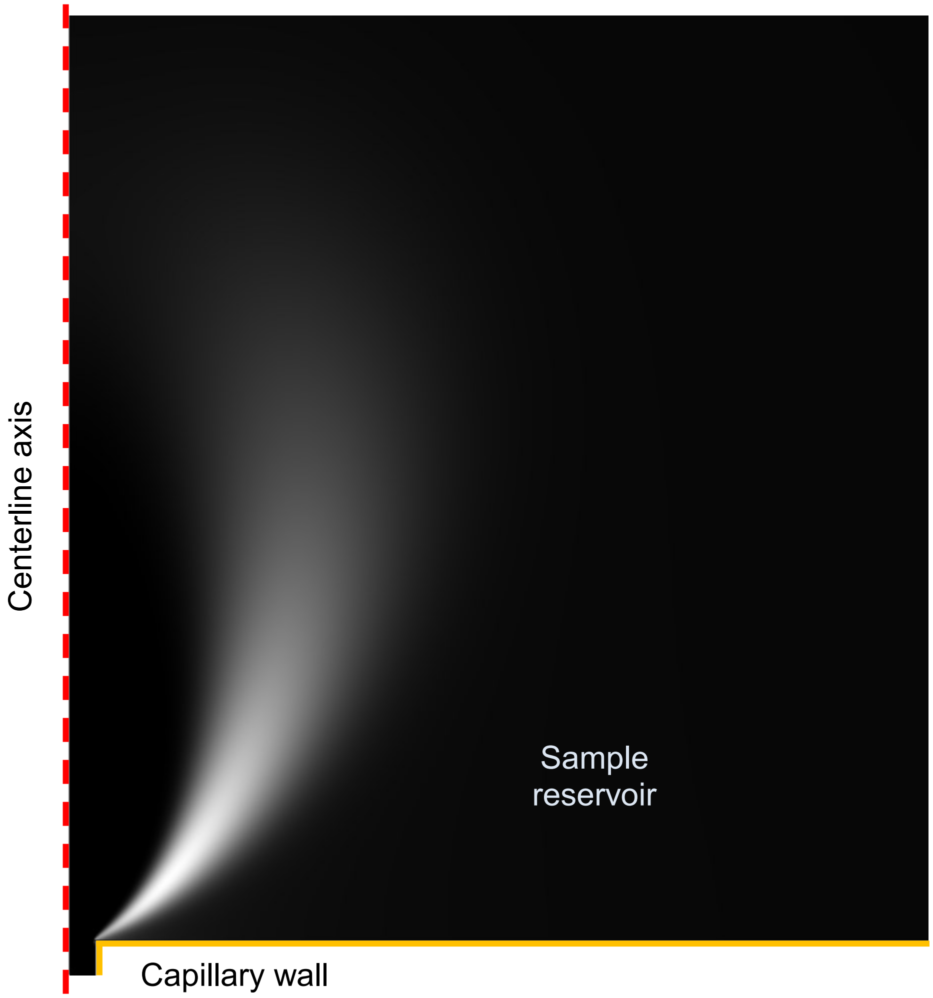
Centerline axis
Sample
reservoir
Capillary wall

Figure 5.11. Donut-shaped bolus observed in simulation

DNA concentration profile from 1X EB + 9mM NaCl simulation experiment. The DNA concentration bolus is donut shaped because fluid flow out of the capillary is stronger than the induced electric field. DNA can only concentrate in the slower flow streams away from the capillary center. Reprinted from ref [54].

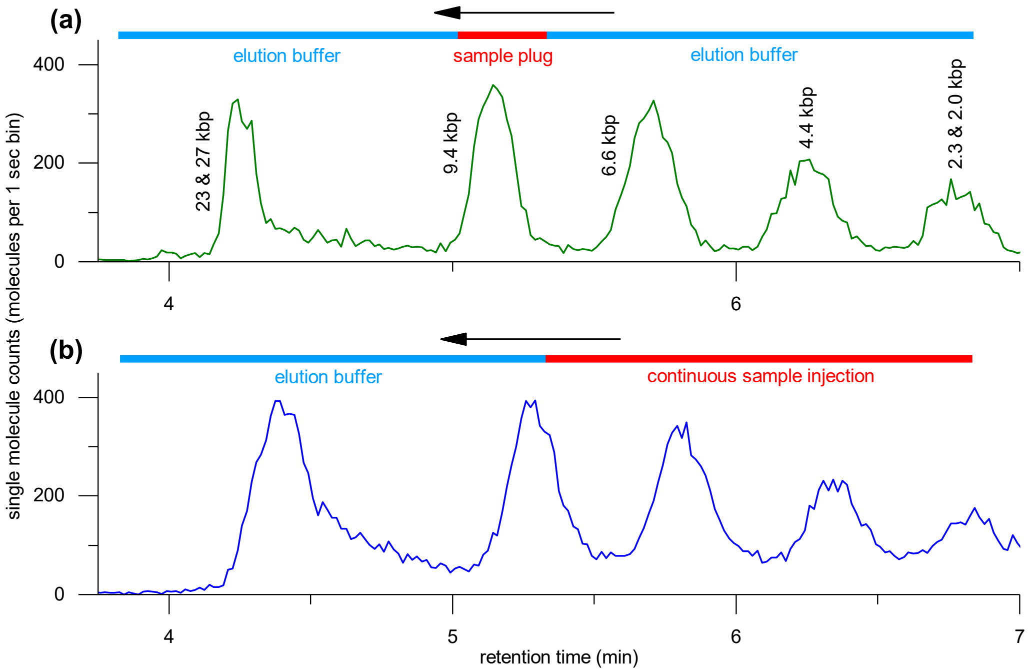

(c)

Fragment Size (kbp)	Number of Molecules		FWHM (min)		Resolution	
	Traditional	1-step	Traditional	1-step	Traditional	1-step
2.0 & 2.3	1744	663	0.21	0.15	1.51	1.75
4.4	2321	1691	0.20	0.17	1.74	1.70
6.6	3183	3272	0.17	0.20	2.06	1.64
9.4	3099	3716	0.14	0.18	4.10	2.48
23 & 27	2207	5105	0.11	0.24		

Figure 5.12. MRT preconcentration enables single-step sample injection and separation

Two chromatograms are presented after the same concentration conditions (15 minutes of counterflow at 200 psi). In (a), the traditional 2-step sample plug injection method is employed. The concentrated sample is injected as a plug (10 s injection at 50 psi). Separation is then performed by replacing the sample tube with a buffer tube for separation at 450 psi. In (b), separation is performed directly from the concentrated sample. After concentration, the sample tube is pressurized to 450 psi continuously throughout the entire separation. This allowed full automation from sample concentration through separation and detection without any additional user operation. The table in (c) compares the number of molecules, peak width, and resolution after fitting the chromatograms in (a) and (b). Reprinted from ref [54].

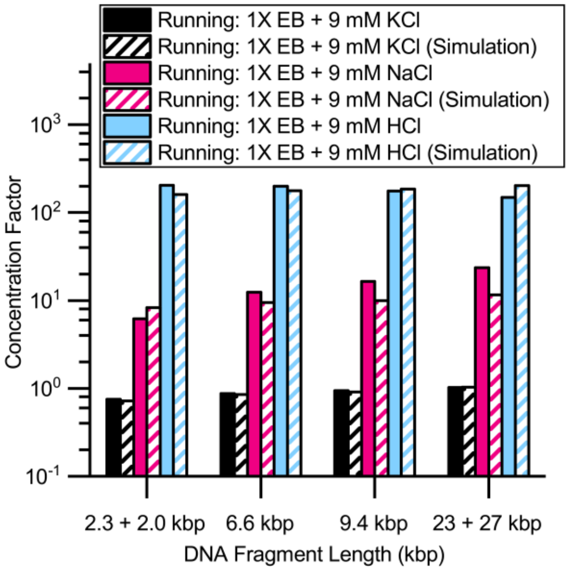
Running: 1X EB + 9 mM KCl
Running: 1X EB + 9 mM KCl (Simulation)
Running: 1X EB + 9 mM NaCl
Running: 1X EB + 9 mM NaCl (Simulation)
Running: 1X EB + 9 mM HCl
Running: 1X EB + 9 mM HCl (Simulation)
Concentration Factor
10^{3}
10^{2}
10^{1}
10^{0}
10^{-1}
2.3 + 2.0 kbp
6.6 kbp
9.4 kbp
23 + 27 kbp
DNA Fragment Length (kbp)

Figure 5.13. Effect of running buffer cation species on MRT concentration factor

The same buffering species are used in both the reservoir and running buffers: 1X EB (10 mM EACA and 40 mM Bis-Tris). Running buffer contains an additional 9 mM of the indicated species (KCl, NaCl, HCl). The concentration factor after 2 min of counterflow at 200 psi is plotted from experimental (solid) and simulated (striped) results. When KCl is added to the running buffer (black), the DNA does not concentrate above the starting concentration. When NaCl is added to the running buffer (pink), a 10 fold concentration effect is observed. The running buffer containing HCl (blue) results in the highest concentration factor– over 100 fold. Reprinted from ref [54].

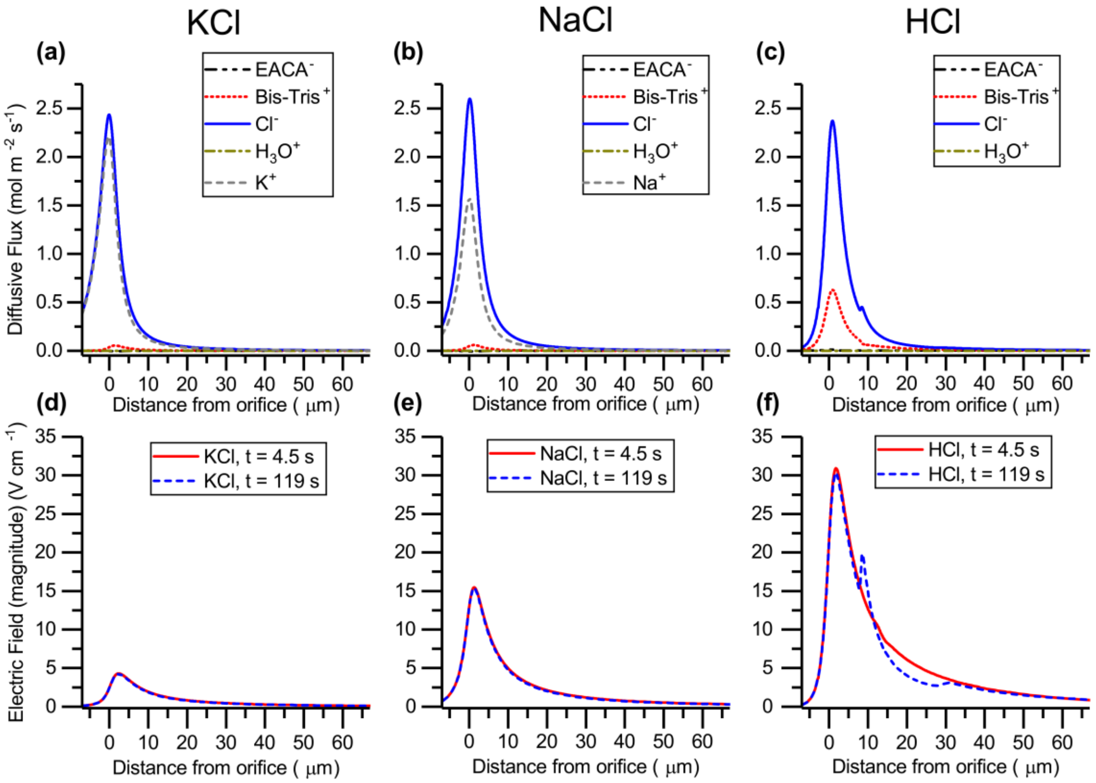
KCl
NaCl
HCl
(a)
(b)
(c)
EACA$^-$
Bis-Tris$^+$
Cl$^-$
H_3O^+
K^+
Na^+
Diffusive Flux (mol m^{-2} s^{-1})
0.0
0.5
1.0
1.5
2.0
2.5
0 10 20 30 40 50 60
Distance from orifice (µm)
(d)
(e)
(f)
KCl, t = 4.5 s
KCl, t = 119 s
NaCl, t = 4.5 s
NaCl, t = 119 s
HCl, t = 4.5 s
HCl, t = 119 s
Electric Field (magnitude) (V cm^{-1})
0
5
10
15
20
25
30
35

Figure 5.14. Centerline ion diffusive fluxes and induced electric field magnitude in KCl, HCl, and NaCl simulations

The simulation conditions are the same as Fig. 5: both reservoir and running buffers contain 1X EB; running buffer contains an additional 9 mM of KCl (left), NaCl (middle), or HCl (right). Diffusive fluxes of ions at 119 s time point in (a) KCl, (b) NaCl, and (c) HCl are plotted along the centerline of the capillary as a function of distance into the reservoir. The capillary orifice is located at x = 0. Cl^- is the majority anion carrier in all cases (blue, solid). In KCl (a), the diffusive flux of K^+ (grey, dashed) is almost as high as Cl^-, and the rest of the ions are negligible. In (b), Na^+ (gray, dashed) has the second largest flux, with the other ions negligible. In HCl (c), Bis-Tris$^+$ (red, dotted) becomes the majority cation, though its flux is smaller than both Na^+ and K^+. The magnitude of the induced electric field generated by these ion fluxes is plotted at 4.5 s (red, solid) and 119 s (blue, dashed) time points in (d) KCl, (e) NaCl, and (f) HCl. The largest field is generated in HCl and extends tens of microns into the sample reservoir. NaCl generates the second largest field, and KCl generates the smallest. The field magnitude and shape are highly stable with time for all 3 conditions, except where the concentrated DNA bolus somewhat distorts the field in HCl at 119 s. Reprinted from ref [54].

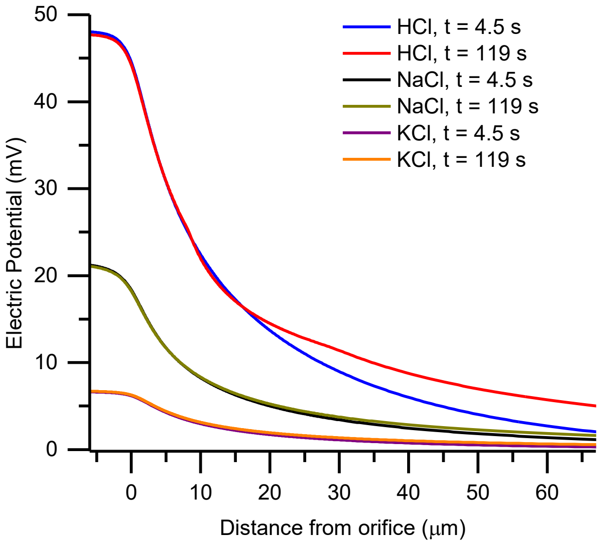

Electric Potential (mV)
50
40
30
20
10
0
0
10
20
30
40
50
60
Distance from orifice (μm)
HCl, t = 4.5 s
HCl, t = 119 s
NaCl, t = 4.5 s
NaCl, t = 119 s
KCl, t = 4.5 s
KCl, t = 119 s

Figure 5.15. Centerline electric potential in KCl, HCl, and NaCl simulations

The smallest potential, KCl, corresponds to the buffer with the majority ions (K^+ and Cl^-) with the most closely matched diffusivities. NaCl generates a larger potential, but the largest potential is generated in HCl. Reprinted from ref [54].

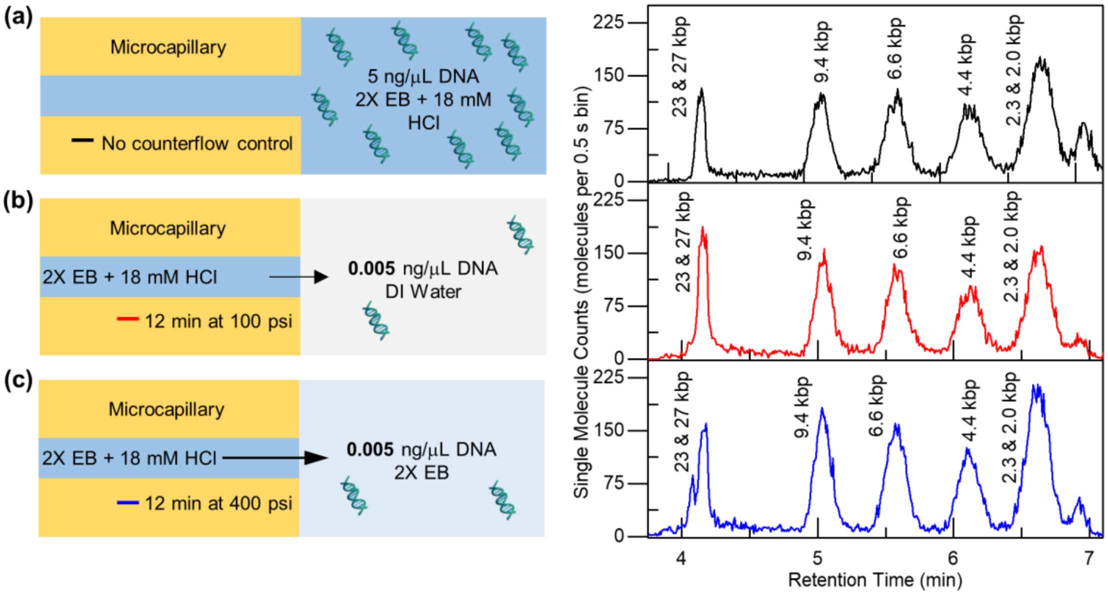
(a)
Microcapillary
5 ng/µL DNA
2X EB + 18 mM HCl
No counterflow control
(b)
Microcapillary
2X EB + 18 mM HCl
0.005 ng/µL DNA
DI Water
12 min at 100 psi
(c)
Microcapillary
2X EB + 18 mM HCl
0.005 ng/µL DNA
2X EB
12 min at 400 psi
23 & 27 kbp
9.4 kbp
6.6 kbp
4.4 kbp
2.3 & 2.0 kbp
225
150
75
0
Single Molecule Counts (molecules per 0.5 s bin)
4
5
6
7
Retention Time (min)

Figure 5.16: Effect of reservoir buffer solution on MRT preconcentration

A schematic describing the experimental preconcentration conditions is shown on the left, and the single molecule chromatogram after separation is shown on the right. In all conditions, 2X EB + 18 mM HCl was used as the running buffer. (a) Control separation of λ DNA *Hind*III digest without preconcentration or a buffer mismatch: the reservoir buffer is the same as the running buffer and no counterflow is applied. (b) Counterflow at 100 psi for 12 minutes into reservoir buffer containing *Hind*III digested λ DNA in DI water. The DNA, originally suspended at 0.005 ng/μL concentrates 1,000 fold prior to separation. (c) A similar 1,000 fold concentration factor is achieved with the reservoir buffer solutions containing DNA prepared in 2X EB by flowing at a 4 fold higher flow rate (400 psi for 12 min). Reprinted from ref [54].

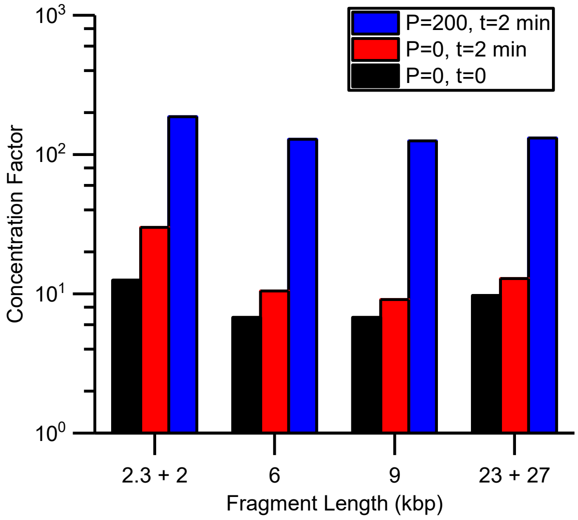
10^3
10^2
10^1
10^0
Concentration Factor
P=200, t=2 min
P=0, t=2 min
P=0, t=0
2.3 + 2
6
9
23 + 27
Fragment Length (kbp)

Figure 5.17. Counterflow increases concentration factor for EB Buffer system

The DNA sample is prepared in 2X EB and the running buffer is 2X EB + 18 mM HCl. The minimum achievable time between initial contact between the capillary orifice and sample reservoir and sample injection (limited by the experimental procedure to ~15-30 seconds) is called time t=0. Under these conditions (black), the concentration enhancement is approximately 10-fold. When the capillary outlet and DNA sample reservoir are held in contact for an additional 2 minutes without any applied pressure (red), minimal additional concentration is measured. When 200 psi counterflow is applied to that sample for 2 minutes (blue), the concentration factor increases to 100-fold. Reprinted from ref [54].

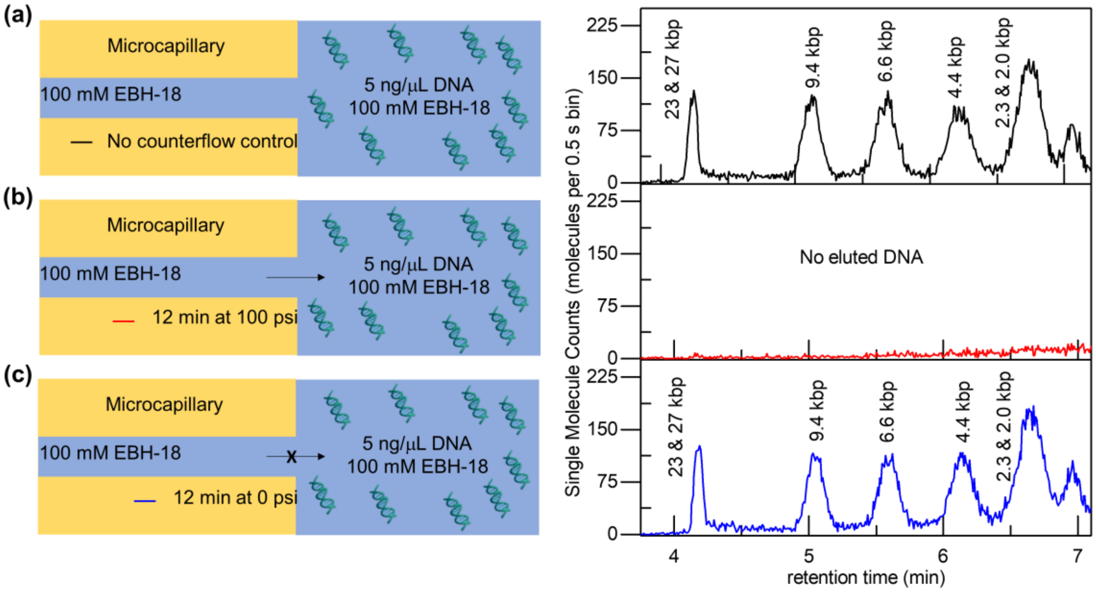
(a)
Microcapillary
100 mM EBH-18
— No counterflow control
5 ng/μL DNA
100 mM EBH-18
(b)
Microcapillary
100 mM EBH-18
— 12 min at 100 psi
5 ng/μL DNA
100 mM EBH-18
(c)
Microcapillary
100 mM EBH-18
x
— 12 min at 0 psi
5 ng/μL DNA
100 mM EBH-18
Single Molecule Counts (molecules per 0.5 s bin)
225
150
75
0
23 & 27 kbp
9.4 kbp
6.6 kbp
4.4 kbp
2.3 & 2.0 kbp
No eluted DNA
4
5
6
7
retention time (min)

Figure 5.18. Effect of counterflow and DNA diffusion in absence of buffer mismatch Running buffer and reservoir buffer are 2X EB + 18 mM HCl. *Hind*III digested λ DNA is prepared at 5 ng/mL concentration. (a) Control SML-FSHS separation without counterflow. Following traditional SML-FSHS protocol, the sample plug is injected quickly after the capillary contacts the sample reservoir. The sample reservoir is then exchanged with running buffer, and the sample plug is separated. (b) Counterflow is applied for 12 minutes at 100 psi prior to separation. In the absence of a buffer mismatch, counterflow generated a region of low DNA concentration around the capillary inlet, preventing any DNA molecules from being injected into the capillary when the pressure is reversed. As one would expect, the single molecule chromatogram under these conditions appears empty. (c) The capillary and sample reservoir are held in contact for 12 minutes without a pressure gradient (0 psi) prior to sample injection and separation. The chromatogram is very similar to (a), indicating that flow does not occur in the absence of an applied pressure gradient and that DNA diffusion driven by its own concentration gradient over this time scale is negligible and cannot be responsible for the high concentration factors achieved in other conditions. Reprinted from ref [54].

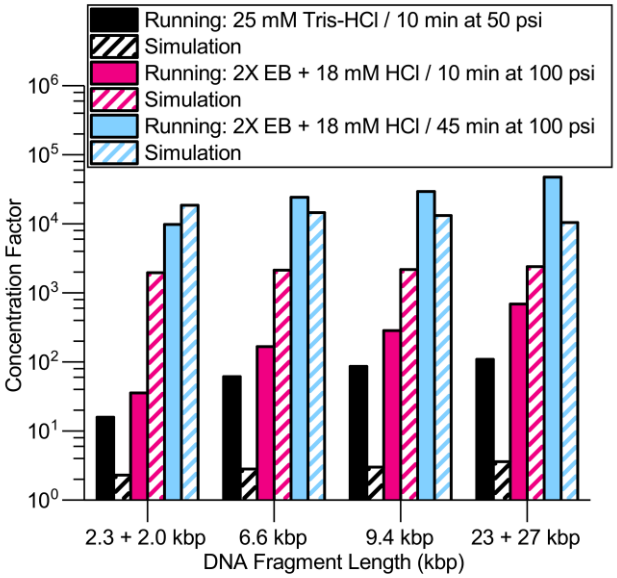
Running: 25 mM Tris-HCl / 10 min at 50 psi
Simulation
Running: 2X EB + 18 mM HCl / 10 min at 100 psi
Simulation
Running: 2X EB + 18 mM HCl / 45 min at 100 psi
Simulation
Concentration Factor
10^0
10^1
10^2
10^3
10^4
10^5
10^6
2.3 + 2.0 kbp
6.6 kbp
9.4 kbp
23 + 27 kbp
DNA Fragment Length (kbp)

Figure 5.19: Concentration factors increase with optimized buffers and concentration times

Experimental (solid) and simulated (striped) results compare concentration factors with 25 mM Tris-HCl running buffer (black) with 100 mM EBH-18 running buffer at 10 min (pink) and 45 min (blue) at each buffer's optimal flow rate. Simulated (striped) and experimental (solid) results show the same trend of increasing concentration factors with increased concentration time and mobility difference between the majority cation and anion in the running buffer. The 2X EB + 18 mM HCl running buffer has a greater mobility difference between the majority cation and anion and generates higher concentration factors than the 25 mM Tris-HCl running buffer over the same counterflow time. Further increase of the counterflow time allows more DNA to accumulate in the injection region for higher concentration factors. Concentration factors over 10,000 fold were achieved experimentally with 45 minutes of preconcentration counterflow. Reprinted from ref [54].

Buffer Short Name	**Buffer Components**	**pH**	**Running Buffer**	**Reservoir Buffer**	**Figure(s)**
100 mM Tris-HCl	100 mM Tris HCl titrated	8.0	X		1
1 mM HEPES-Tris	1 mM HEPES Tris titrated	6.8		X	1
25 mM Tris-HCl	25 mM Tris HCl titrated	8.0	X		3, 4, 8
2X EB + 18 mM HCl	80 mM Bis-Tris 20 mM EACA 18 mM HCl	7.0	X		2, 7, 8
1X EB+ 9 mM HCl	40 mM Bis-Tris 10 mM EACA 9 mM HCl	7.0	X		5, 6 (c,f)
1X EB+ 9 mM NaCl	40 mM Bis-Tris 10 mM EACA 9 mM NaCl	8.0	X		5, 6 (b,e)
1X EB+ 9 mM KCl	40 mM Bis-Tris 10 mM EACA 9 mM KCl	8.0	X		5, 6 (a,d)
DI Water	--	--		X	2, 3, 4, 7, 8
2X EB	80 mM Bis-Tris 20 mM EACA	8.5		X	7
1X EB	40 mM Bis-Tris 10 mM EACA	8.5		X	5, 6

Table 5.1. Characteristics of experimental buffers used in main text figures including component concentrations, pH, and principle use.

Reprinted from ref [54].

	Running Buffer	Reservoir Buffer	Concentration?
1	100 mM Tris-HCl	1 mM Tris-HEPES	Y
2	100 mM Tris-HCl + 0.5% PVP	1 mM Tris-HEPES	Y
3	100 mM Tris-HCl	100 mM Tris-HCl	N
4	1 mM Tris-HEPES	1 mM Tris-HEPES	N
5	1 mM Tris-HEPES	100 mM Tris-HCl	N
6	100 mM Tris-HEPES	1 mM Tris-HEPES	N

Table 5.2. Initial buffer combinations examined to identify MRT mechanism.

Reprinted from ref [54].

Chapter 6

6. Conclusion

7.1 Summary

We have demonstrated the unique capabilities of our SML-FSHS platform for highly versatile, sensitive, and quantitative analysis of DNA molecules and complexes. Free solution hydrodynamic separation enables high resolution separation over a wide dynamic sizing range without the need for polymeric gel matrices or mass tags to modulate DNA mobility. Cylindrical Illumination Confocal Spectroscopy enables single molecule detection with high mass detection efficiency and burst uniformity, increasing the sensitivity and quantitative capabilities and enabling new modes of multiparametric analysis of species shape and population distributions. The integrated platform has been used to separate and evaluate DNA fragment lengths, global conformations, DNA hybridization, and DNA-protein binding properties in free solution with near zero sample consumption. The development and integration of the Molecular Rheotaxis in-line preconcentration technique further increases the analytical sensitivity and detection dynamic range of the platform, overcoming the limitations of small injection volumes to enable amplification-free analysis of very dilute or rare DNA species.

7.2 Future Directions

As the study and use of DNA in fields of biology, diagnostics, and therapeutic development continues to expand, sensitive and quantitative methods for characterizing a diverse array of properties and interactions will be vital for continued and rapid development. We foresee applications of this technology in fundamental biomedical research, assay development, end-point detection for multiplexed analysis, and therapeutic development, testing, and quality control. For example, applications such as gene therapy will require methods to analyze and track the polydispersity of multiple properties of synthesized gene delivery vectors such as size, shape, DNA content, and mobility.[28] Third-generation sequencing can be made more robust and efficient with simple, effective, and low-sample consumption methods to evaluate sample integrity throughout library preparation.[56] And given the robustness and simplicity of MRT, we anticipate utility in a wide range of applications such as in microfluidic devices, point-of-care sample handling, and biomolecular assays for both nucleic acid and protein analysis, both as a stand-alone technology and coupled to subsequent molecular analysis operations including but not limited to our SML-FSHS platform.

Further improvements in the SML-FSHS platform operation and MRT concentration could help to bring such applications to fruition. For analysis in a commercial setting, full automation and parallelized analysis will be critical to achieving the high-throughput requirements of large centralized lab settings. Full automation can be achieved by integrating existing automated sample preparation with a serial sample loading system, as has been described previously.[161] Parallelization could be achieved with capillary arrays, as has been demonstrated with Capillary Electrophoresis[162], or by migrating the separation method to a microfluidic device, similar to Microchip Electrophoresis[163, 164], which can be designed with many parallel analysis channels. However, each method has its own hurdles to development. We have demonstrated FSHS on a microchip,[165] but improving fabrication throughput, sample introduction, and device interfacing will be required to reduce sample injection variability, minimize sample losses, and enable high speed, high resolution separations comparable to what has been demonstrated in a capillary. Development of a capillary array will require expansion and adjustment to the CICS single molecule detection scheme to scan across multiple capillary cross sections with accurate alignment.

For MRT, increasing the concentration speed, concentration factors, and/or concentration volume, as well as improving sample and buffer compatibility will be critical to realizing analysis directly from biosamples. We suggest multiple strategies could be implemented to improve the concentration enhancement. First,optimizing parameters such as the shape and volume of the sample reservoir and microcapillary could influence both the MRT duration limit and concentration rate. Second, the use of a higher ion concentration in the running buffer to increase the solute concentration gradient (i.e. the diffusive driving force) could enhance the concentration scheme in two ways: (1) an increase in the volume of the reservoir spanned by the solute concentration gradient and (2) an increase in the DNA migration speed. Similarly, a combination of mono- and multivalent salts may be able to boost the induced electric field and increase the speed or concentration capability of the MRT scheme. Finally, we propose that inducing gentle mixing within the sample solution could increase the achievable concentration factors in a similar fashion to what has been demonstrated for electrokinetic preconcentration.[166]

The relatively high salt concentrations present in many biofluids (e.g. serum) also presents a challenge for MRT. Adapting or modifying the technique to either utilize, neutralize, or overpower these salts would enable direct analysis of clinical samples without preprocessing. One possibility is to reverse the MRT operating mode and utilize the high ionic strength of the biosample to drive MRT concentration. We have performed concentration in this mode to validate the concept; however, concentration occurred more slowly due to the low volumetric flow rate that limited DNA flux to the interface. Overcoming this volumetric flow rate limitation would require understanding the relationship between capillary diameter, flow rate, and MRT concentration, which has not yet been elucidated.

Despite the current limitations listed here, the rate of growth in the fields of microfabrication, single molecule detection, and big data analytics are sure to yield impressive and meaningful advances and discoveries in the wide and diverse field of nucleic acid analysis.

References

1. Fan, H.C. and S.R. Quake, *Detection of aneuploidy with digital polymerase chain reaction.* Analytical chemistry, 2007. **79**(19): p. 7576-7579.
2. Fan, H.C., et al., *Non-invasive prenatal measurement of the fetal genome.* Nature, 2012. **487**(7407): p. 320-324.
3. Schwarzenbach, H., D.S. Hoon, and K. Pantel, *Cell-free nucleic acids as biomarkers in cancer patients.* Nature Reviews Cancer, 2011. **11**(6): p. 426-437.
4. Liu, K.J., et al., *Decoding Circulating Nucleic Acids in Human Serum Using Microfluidic Single Molecule Spectroscopy.* Journal of the American Chemical Society, 2010. **132**(16): p. 5793-5798.
5. Diaz, L.A., Jr. and A. Bardelli, *Liquid biopsies: genotyping circulating tumor DNA.* Journal of clinical oncology : official journal of the American Society of Clinical Oncology, 2014. **32**(6): p. 579-86.
6. Pisanic, T.R., et al., *DREAMing: a simple and ultrasensitive method for assessing intratumor epigenetic heterogeneity directly from liquid biopsies.* Nucleic acids research, 2015. **43**(22): p. e154.
7. Gerlinger, M., et al., *Intratumor heterogeneity and branched evolution revealed by multiregion sequencing.* New England Journal of Medicine, 2012. **366**(10): p. 883-892.
8. Marusyk, A. and K. Polyak, *Tumor heterogeneity: causes and consequences.* Biochimica et biophysica acta, 2010. **1805**(1): p. 105-17.
9. Ottesen, E.A., et al., *Microfluidic digital PCR enables multigene analysis of individual environmental bacteria.* Science, 2006. **314**(5804): p. 1464-1467.
10. Du, W., et al., *SlipChip.* Lab on a Chip, 2009. **9**(16): p. 2286-2292.
11. Hindson, B.J., et al., *High-throughput droplet digital PCR system for absolute quantitation of DNA copy number.* Analytical chemistry, 2011. **83**(22): p. 8604-8610.
12. Song, L.A., et al., *Direct Detection of Bacterial Genomic DNA at Sub-Femtomolar Concentrations Using Single Molecule Arrays.* Analytical chemistry, 2013. **85**(3): p. 1932-1939.
13. Guan, W., et al., *Droplet Digital Enzyme-Linked Oligonucleotide Hybridization Assay for Absolute RNA Quantification.* Scientific Reports, 2015. **5**: p. 13795.
14. Vasdekis, A.E. and G.P.J. Laporte, *Enhancing Single Molecule Imaging in Optofluidics and Microfluidics.* International Journal of Molecular Sciences, 2011. **12**(8): p. 5135-5156.
15. Mouliere, F. and N. Rosenfeld, *Circulating tumor-derived DNA is shorter than somatic DNA in plasma.* Proceedings of the National Academy of Sciences, 2015. **112**(11): p. 3178-3179.
16. Elshimali, Y., et al., *The Clinical Utilization of Circulating Cell Free DNA (CCFDNA) in Blood of Cancer Patients.* International Journal of Molecular Sciences, 2013. **14**(9): p. 18925-18958.
17. Yu, S.C.Y., et al., *Size-based molecular diagnostics using plasma DNA for noninvasive prenatal testing.* Proceedings of the National Academy of Sciences, 2014. **111**(23): p. 8583-8588.
18. Hyytia-Trees, E.K., et al., *Recent developments and future prospects in subtyping of foodborne bacterial pathogens.* Future microbiology, 2007. **2**(2): p. 175-85.
19. Eid, J., et al., *Real-Time DNA Sequencing from Single Polymerase Molecules.* Science, 2009. **323**(5910): p. 133-138.

20. Feng, Y., et al., *Nanopore-based fourth-generation DNA sequencing technology.* Genomics, proteomics & bioinformatics, 2015. **13**(1): p. 4-16.
21. Schwartz, D.C., et al., *Ordered restriction maps of Saccharomyces cerevisiae chromosomes constructed by optical mapping.* Science, 1993. **262**(5130): p. 110-4.
22. Lim, A., et al., *Shotgun optical maps of the whole Escherichia coli O157 : H7 genome.* Genome Research, 2001. **11**(9): p. 1584-1593.
23. Dimalanta, E.T., et al., *A microfluidic system for large DNA molecule arrays.* Analytical chemistry, 2004. **76**(18): p. 5293-5301.
24. Xiao, M., et al., *Rapid DNA mapping by fluorescent single molecule detection.* Nucleic acids research, 2007. **35**(3): p. e16.
25. Egger, G., et al., *Epigenetics in human disease and prospects for epigenetic therapy.* Nature, 2004. **429**(6990): p. 457-463.
26. Ha, T., et al., *Probing the interaction between two single molecules: Fluorescence resonance energy transfer between a single donor and a single acceptor.* Proceedings of the National Academy of Sciences of the United States of America, 1996. **93**(13): p. 6264-6268.
27. Deniz, A.A., et al., *Single-pair fluorescence resonance energy transfer on freely diffusing molecules: Observation of Forster distance dependence and subpopulations.* Proceedings of the National Academy of Sciences of the United States of America, 1999. **96**(7): p. 3670-3675.
28. Beh, C.W., et al., *Direct interrogation of DNA content distribution in nanoparticles by a novel microfluidics-based single-particle analysis.* Nano Letters, 2014. **14**(8): p. 4729-35.
29. Silverstein, T.D., B. Gibb, and E.C. Greene, *Visualizing protein movement on DNA at the single-molecule level using DNA curtains.* DNA Repair, 2014. **20**: p. 94-109.
30. Horrocks, M.H., et al., *Single-Molecule Measurements of Transient Biomolecular Complexes through Microfluidic Dilution.* Analytical chemistry, 2013. **85**(14): p. 6855-6859.
31. Friedrich, S.M., H.C. Zec, and T.-H. Wang, *Analysis of Single Nucleic Acid Molecules in Micro- and Nano- Fluidics.* Lab on a chip, 2016. **16**(5): p. 790-811.
32. Liu, K.J., et al., *Single-molecule analysis enables free solution hydrodynamic separation using yoctomole levels of DNA.* Journal of the American Chemical Society, 2011. **133**(18): p. 6898-901.
33. Friedrich, S.M., K.J. Liu, and T.H. Wang. *Single Molecule Hydrodynamic Separation for Ultrasensitive and Quantitative DNA Size Separations*. in *Proceedings of The 17th International Conference on Miniaturized Systems for Chemistry and Life Sciences*. 2013. Freiburg, Germany: The Printing House, Inc.
34. Wang, B.G., et al., *Increased plasma DNA integrity in cancer patients.* Cancer Research, 2003. **63**(14): p. 3966-3968.
35. Jahr, S., et al., *DNA fragments in the blood plasma of cancer patients: quantitations and evidence for their origin from apoptotic and necrotic cells.* Cancer Research, 2001. **61**(4): p. 1659-1665.
36. Danna, K. and D. Nathans, *Specific cleavage of simian virus 40 DNA by restriction endonuclease of Hemophilus influenzae.* Proceedings of the National Academy of Sciences, 1971. **68**(12): p. 2913-2917.
37. Jeffreys, A.J., V. Wilson, and S.L. Thein, *Hypervariable ‘minisatellite’ regions in human DNA.* Nature, 1985. **314**(6006): p. 67-73.
38. Schouten, J.P., et al., *Relative quantification of 40 nucleic acid sequences by multiplex ligation-dependent probe amplification.* Nucleic acids research, 2002. **30**(12): p. e57.

39. Weinberger, R., *Practical Capillary Electrophoresis*. 2000: Academic Press.
40. Horvath, J. and V. Dolník, *Polymer wall coatings for capillary electrophoresis.* Electrophoresis, 2001. **22**(4): p. 644-655.
41. Ye, X., et al., *DNA aggregation and cleavage in CGE induced by high electric field in aqueous solution accompanying electrokinetic sample injection.* Electrophoresis, 2013. **34**(22-23): p. 3155-3162.
42. Striegel, A.M. and A.K. Brewer, *Hydrodynamic Chromatography.* Annual Review of Analytical Chemistry, Vol 5, 2012. **5**: p. 15-34.
43. Tijssen, R., J.P.A. Bleumer, and M.E. Vankreveld, *Separation by Flow (Hydrodynamic Chromatography) of Macromolecules Performed in Open Microcapillary Tubes.* Journal of Chromatography, 1983. **260**(2): p. 297-304.
44. Wang, X., et al., *Nanocapillaries for Open Tubular Chromatographic Separations of Proteins in Femtoliter to Picoliter Samples.* Analytical chemistry, 2009. **81**(17): p. 7428-7435.
45. Iki, N., Y. Kim, and E.S. Yeung, *Electrostatic and Hydrodynamic Separation of DNA Fragments in Capillary Tubes.* Analytical chemistry, 1996. **68**(24): p. 4321-4325.
46. Wang, X.Y., et al., *Bare nanocapillary for DNA separation and genotyping analysis in gel-free solutions without application of external electric field.* Analytical Chemistry, 2008. **80**(14): p. 5583-5589.
47. Wang, X.Y., et al., *Free Solution Hydrodynamic Separation of DNA Fragments from 75 to 106 000 Base Pairs in A Single Run.* Journal of the American Chemical Society, 2010. **132**(1): p. 40-+.
48. Friedrich, S.M., K.J. Liu, and T.H. Wang, *Single Molecule Hydrodynamic Separation Allows Sensitive and Quantitative Analysis of DNA Conformation and Binding Interactions in Free Solution.* Journal of the American Chemical Society, 2016. **138**(1): p. 319-327.
49. Frost, N.W., M. Jing, and M.T. Bowser, *Capillary Electrophoresis.* Analytical Chemistry, 2010. **82**(12): p. 4682-4698.
50. Kostal, V., J. Katzenmeyer, and E.A. Arriaga, *Capillary electrophoresis in bioanalysis.* Analytical Chemistry, 2008. **80**(12): p. 4533-4550.
51. Zhu, Z.F., et al., *Simultaneously Sizing and Quantitating Zeptomole-Level DNA at High Throughput in Free Solution.* Chemistry-a European Journal, 2014. **20**(43): p. 13945-13950.
52. Haab, B.B. and R.A. Mathies, *Single molecule fluorescence burst detection of DNA fragments separated by capillary electrophoresis.* Anal Chem, 1995. **67**(18): p. 3253-60.
53. Liu, K.J. and T.H. Wang, *Cylindrical illumination confocal spectroscopy: rectifying the limitations of confocal single molecule spectroscopy through one-dimensional beam shaping.* Biophysical journal, 2008. **95**(6): p. 2964-75.
54. Friedrich, S.M., et al., *Molecular rheotaxis directs DNA migration and concentration against a pressure-driven flow.* Nat Commun, 2017. **8**(1): p. 1213.
55. Tijssen, R., J. Bos, and M.E. Vankreveld, *Hydrodynamic Chromatography of Macromolecules in Open Microcapillary Tubes.* Analytical Chemistry, 1986. **58**(14): p. 3036-3044.
56. Zhang, Y., et al., *A Simple Thermoplastic Substrate Containing Hierarchical Silica Lamellae for High-Molecular-Weight DNA Extraction.* Advanced Materials, 2016. **28**(48): p. 10630-+.
57. Wang, X.Y., et al., *Pressure-Induced Transport of DNA Confined in Narrow Capillary Channels.* Journal of the American Chemical Society, 2012. **134**(17): p. 7400-7405.

58. Hellman, L.M. and M.G. Fried, *Electrophoretic Mobility Shift Assay (EMSA) for Detecting Protein-Nucleic Acid Interactions.* Nature protocols, 2007. **2**(8): p. 1849-1861.
59. Xu, Y., et al., *Induced-fit or preexisting equilibrium dynamics? Lessons from protein crystallography and MD simulations on acetylcholinesterase and implications for structure-based drug design.* Protein science : a publication of the Protein Society, 2008. **17**(4): p. 601-5.
60. DiGabriele, A.D., M.R. Sanderson, and T.A. Steitz, *Crystal lattice packing is important in determining the bend of a DNA dodecamer containing an adenine tract.* Proceedings of the National Academy of Sciences of the United States of America, 1989. **86**(6): p. 1816-20.
61. Meseth, U., et al., *Resolution of fluorescence correlation measurements.* Biophysical journal, 1999. **76**(3): p. 1619-1631.
62. Roy, R., S. Hohng, and T. Ha, *A practical guide to single-molecule FRET.* Nature Methods, 2008. **5**(6): p. 507-516.
63. Petty, J.T., et al., *Characterization of DNA Size Determination of Small Fragments by Flow-Cytometry.* Analytical Chemistry, 1995. **67**(10): p. 1755-1761.
64. Reccius, C.H., et al., *Conformation, Length, and Speed Measurements of Electrodynamically Stretched DNA in Nanochannels.* Biophysical journal, 2008. **95**(1): p. 273-286.
65. Bier, M., J. Ostrem, and R.B. Marquez, *A new buffering system and its use in electrophoresis and isoelectric focusing.* Electrophoresis, 1993. **14**(1): p. 1011-1018.
66. Chen, H., et al., *Ionic strength-dependent persistence lengths of single-stranded RNA and DNA.* Proceedings of the National Academy of Sciences, 2012. **109**(3): p. 799-804.
67. Baumann, C.G., et al., *Ionic effects on the elasticity of single DNA molecules.* Proceedings of the National Academy of Sciences, 1997. **94**(12): p. 6185-6190.
68. Korolev, N., et al., *Competitive binding of mg(2+), ca(2+), na(+), and K(+) ions to DNA in oriented DNA fibers: experimental and monte carlo simulation results.* Biophysical journal, 1999. **77**(5): p. 2736-2749.
69. Graham, M.D., *Fluid Dynamics of Dissolved Polymer Molecules in Confined Geometries.* Annual Review of Fluid Mechanics, 2011. **43**(1): p. 273-298.
70. Shafer, R.H., N. Laiken, and B.H. Zimm, *Radial migration of DNA molecules in cylindrical flow: I. Theory of the free-draining model.* Biophysical Chemistry, 1974. **2**(2): p. 180-184.
71. Shafer, R.H., *Radial migration of DNA molecules in cylindrical flow: II. The non-draining model and possible application to fractionation.* Biophysical Chemistry, 1974. **2**(2): p. 185-188.
72. Jendrejack, R., et al., *DNA Dynamics in a Microchannel.* Physical Review Letters, 2003. **91**(3).
73. Jendrejack, R.M., et al., *Shear-induced migration in flowing polymer solutions: Simulation of long-chain DNA in microchannels (vol 120, pg 2513, 2004).* Journal of Chemical Physics, 2004. **120**(13): p. 6315-6315.
74. Raghunath, C., G.W. Roland, and G. Gerhard, *Semiflexible polymer conformation, distribution and migration in microcapillary flows.* Journal of Physics: Condensed Matter, 2011. **23**(18): p. 184117.
75. Takahashi, M., et al., *Discrete coil-globule transition of single duplex DNAs induced by polyamines.* Journal of Physical Chemistry B, 1997. **101**(45): p. 9396-9401.
76. Yoshikawa, Y., K. Yoshikawa, and T. Kanbe, *Formation of a giant toroid from long duplex DNA.* Langmuir, 1999. **15**(12): p. 4085-4088.

77. Arscott, P.G., A.Z. Li, and V.A. Bloomfield, *Condensation of DNA by trivalent cations. 1. Effects of DNA length and topology on the size and shape of condensed particles.* Biopolymers, 1990. **30**(5-6): p. 619-30.
78. Bloomfield, V.A., *Condensation of DNA by multivalent cations: considerations on mechanism.* Biopolymers, 1991. **31**(13): p. 1471-81.
79. Limpert, E., W.A. Stahel, and M. Abbt, *Log-normal distributions across the sciences: Keys and clues.* Bioscience, 2001. **51**(5): p. 341-352.
80. Dey, B., et al., *DNA-protein interactions: methods for detection and analysis.* Molecular and Cellular Biochemistry, 2012. **365**(1-2): p. 279-299.
81. Wanunu, M. and Y. Tor, *Methods for Studying Nucleic Acid/Drug Interactions.* Methods for Studying Nucleic Acid/Drug Interactions, 2012: p. 1-360.
82. Sirajuddin, M., S. Ali, and A. Badshah, *Drug-DNA interactions and their study by UV-Visible, fluorescence spectroscopies and cyclic voltametry.* Journal of Photochemistry and Photobiology B-Biology, 2013. **124**: p. 1-19.
83. Schuck, P., *Protein interactions : biophysical approaches for the study of complex reversible systems*. Protein reviews. 2007, New York, NY: Springer. xi, 532 p.
84. Zavaleta, J., et al., *Recent developments in affinity capillary electrophoresis: A review.* Current Analytical Chemistry, 2006. **2**(1): p. 35-42.
85. Rundlett, K.L. and D.W. Armstrong, *Methods for the estimation of binding constants by capillary electrophoresis.* Electrophoresis, 1997. **18**(12-13): p. 2194-2202.
86. Southern, E.M., *Detection of Specific Sequences among DNA Fragments Separated by Gel-Electrophoresis.* Journal of Molecular Biology, 1975. **98**(3): p. 503-&.
87. Alwine, J.C., D.J. Kemp, and G.R. Stark, *Method for detection of specific RNAs in agarose gels by transfer to diazobenzyloxymethyl-paper and hybridization with DNA probes.* Proceedings of the National Academy of Sciences of the United States of America, 1977. **74**(12): p. 5350-5354.
88. Rippel, G., et al., *Affinity capillary electrophoresis.* Electrophoresis, 1997. **18**(12-13): p. 2175-2183.
89. Xue, B., O.S. Gabrielsen, and A.H. Myrset, *Capillary electrophoretic mobility shift assay (CEMSA) of a protein-DNA complex.* Journal of Capillary Electrophoresis, 1997. **4**(5): p. 225-231.
90. Petrov, A., et al., *Kinetic capillary electrophoresis (KCE): a conceptual platform for kinetic homogeneous affinity methods.* J Am Chem Soc, 2005. **127**(48): p. 17104-10.
91. Adams, C.A. and M.G. Fried, *Analysis of Protein-DNA Equilibria by Native Gel Electrophoresis*, in *Protein Interactions: Biophysical Approaches for the Study of Complex Reversible Systems*, P. Schuck, Editor. 2007, Springer US: Boston, MA. p. 417-446.
92. Rigler, R. and E. Elson, *Fluorescence Correlation Spectroscopy - Theory and Applications*. Springer series in chemical physics,. 2001, Berlin ; New York: Springer. xx, 487 p.
93. Meyer, R.R. and P.S. Laine, *The single-stranded DNA-binding protein of Escherichia coli.* Microbiol Rev, 1990. **54**(4): p. 342-80.
94. Shereda, R.D., et al., *SSB as an Organizer/Mobilizer of Genome Maintenance Complexes.* Critical Reviews in Biochemistry and Molecular Biology, 2008. **43**(5): p. 289-318.
95. Lohman, T.M. and M.E. Ferrari, *Escherichia coli single-stranded DNA-binding protein: multiple DNA-binding modes and cooperativities.* Annu Rev Biochem, 1994. **63**: p. 527-70.
96. Lohman, T.M. and L.B. Overman, *Two binding modes in Escherichia coli single strand binding protein-single stranded DNA complexes. Modulation by NaCl concentration.* J Biol Chem, 1985. **260**(6): p. 3594-603.

97. Ferrari, M.E., W. Bujalowski, and T.M. Lohman, *Co-operative binding of Escherichia coli SSB tetramers to single-stranded DNA in the (SSB)35 binding mode.* J Mol Biol, 1994. **236**(1): p. 106-23.
98. Krauss, G., et al., *Escherichia coli single-strand deoxyribonucleic acid binding protein: stability, specificity, and kinetics of complexes with oligonucleotides and deoxyribonucleic acid.* Biochemistry, 1981. **20**(18): p. 5346-52.
99. Bujalowski, W., L.B. Overman, and T.M. Lohman, *Binding mode transitions of Escherichia coli single strand binding protein-single-stranded DNA complexes. Cation, anion, pH, and binding density effects.* J Biol Chem, 1988. **263**(10): p. 4629-40.
100. Lohman, T.M. and W. Bujalowski, *Effects of base composition on the negative cooperativity and binding mode transitions of Escherichia coli SSB-single-stranded DNA complexes.* Biochemistry, 1994. **33**(20): p. 6167-76.
101. Bujalowski, W. and T.M. Lohman, *Negative co-operativity in Escherichia coli single strand binding protein-oligonucleotide interactions. II. Salt, temperature and oligonucleotide length effects.* J Mol Biol, 1989. **207**(1): p. 269-88.
102. Jerabek-Willemsen, M., et al., *MicroScale Thermophoresis: Interaction analysis and beyond.* Journal of Molecular Structure, 2014. **1077**: p. 101-113.
103. Williams, K.R., J.B. Murphy, and J.W. Chase, *Characterization of the structural and functional defect in the Escherichia coli single-stranded DNA binding protein encoded by the ssb-1 mutant gene. Expression of the ssb-1 gene under lambda pL regulation.* J Biol Chem, 1984. **259**(19): p. 11804-11.
104. LeCaptain, D.J. and O.A. Van, *Two-beam fluorescence cross-correlation spectroscopy in an electrophoretic mobility shift assay.* Anal Chem, 2002. **74**(5): p. 1171-6.
105. Okhonin, V., et al., *Plug-plug kinetic capillary electrophoresis: method for direct determination of rate constants of complex formation and dissociation.* Anal Chem, 2006. **78**(14): p. 4803-10.
106. Kunzelmann, S., et al., *Mechanism of Interaction between Single-Stranded DNA Binding Protein and DNA.* Biochemistry, 2010. **49**(5): p. 843-852.
107. Williams, K.R., et al., *Limited proteolysis studies on the Escherichia coli single-stranded DNA binding protein. Evidence for a functionally homologous domain in both the Escherichia coli and T4 DNA binding proteins.* J Biol Chem, 1983. **258**(5): p. 3346-55.
108. Weiner, J.H., L.L. Bertsch, and A. Kornberg, *The deoxyribonucleic acid unwinding protein of Escherichia coli. Properties and functions in replication.* J Biol Chem, 1975. **250**(6): p. 1972-80.
109. Walker, G.M. and D.J. Beebe, *An evaporation-based microfluidic sample concentration method.* Lab on a chip, 2002. **2**(2): p. 57-61.
110. Sharma, N.R., et al. *Development of an evaporation-based microfluidic sample concentrator*. in *Proc. SPIE 6886, Microfluidics, BioMEMS, and Medical Microsystems VI*. 2008. International Society for Optics and Photonics.
111. Svec, F., *Less common applications of monoliths: Preconcentration and solid-phase extraction.* Journal of Chromatography B, 2006. **841**(1–2): p. 52-64.
112. Kutter, J.P., S.C. Jacobson, and J.M. Ramsey, *Solid phase extraction on microfluidic devices.* Journal of Microcolumn Separations, 2000. **12**(2): p. 93-97.
113. Giordano, B.C., et al., *On-line sample pre-concentration in microfluidic devices: A review.* Analytica Chimica Acta, 2012. **718**: p. 11-24.
114. Lin, C.-C., J.-L. Hsu, and G.-B. Lee, *Sample preconcentration in microfluidic devices.* Microfluidics and Nanofluidics, 2011. **10**(3): p. 481-511.

115. Osbourn, D.M., D.J. Weiss, and C.E. Lunte, *On-line preconcentration methods for capillary electrophoresis.* Electrophoresis, 2000. **21**(14): p. 2768-2779.
116. Rogacs, A., L.A. Marshall, and J.G. Santiago, *Purification of nucleic acids using isotachophoresis.* Journal of Chromatography A, 2014. **1335**: p. 105-120.
117. Ye, X., et al., *Electrokinetic supercharging preconcentration prior to CGE analysis of DNA: Sensitivity depends on buffer viscosity and electrode configuration.* Electrophoresis, 2013. **34**(4): p. 583-589.
118. Montgomery, J.C., C.F. Baker, and A.G. Carton, *The lateral line can mediate rheotaxis in fish.* Nature, 1997. **389**(6654): p. 960-963.
119. Marcos, et al., *Bacterial rheotaxis.* Proceedings of the National Academy of Sciences of the United States of America, 2012. **109**(13): p. 4780-4785.
120. Kaya, T. and H. Koser, *Direct Upstream Motility in Escherichia coli.* Biophysical Journal, 2012. **102**(7): p. 1514-1523.
121. Bretherton, F.P. and Rothschild, *Rheotaxis of Spermatozoa.* Proceedings of the Royal Society of London, Series B: Biological Sciences, 1961. **153**(953): p. 490-502.
122. Palacci, J., et al., *Artificial rheotaxis.* Science Advances, 2015. **1**(4).
123. Uspal, W.E., et al., *Rheotaxis of spherical active particles near a planar wall.* Soft Matter, 2015. **11**(33): p. 6613-6632.
124. Friedrich, S.M., et al., *In-Line DNA Preconcentration, Size Separation, and Single Molecule Detection without Applied Electric Fields.* 2016 Ieee 29th International Conference on Micro Electro Mechanical Systems (Mems), 2016: p. 181-184.
125. Edelstein, A., et al., *Computer Control of Microscopes Using µManager*, in *Current Protocols in Molecular Biology*, F.M. Ausubel, Editor. 2001, John Wiley & Sons, Inc. p. 14.20.1-14.20.17.
126. Wall, S., *The history of electrokinetic phenomena.* Current Opinion in Colloid & Interface Science, 2010. **15**(3): p. 119-124.
127. Kaniansky, D., M. Masár, and J. Bielčíková, *Electroosmotic flow suppressing additives for capillary zone electrophoresis in a hydrodynamically closed separation system.* Journal of Chromatography A, 1997. **792**(1–2): p. 483-494.
128. Derjaguin, B., et al., *Kinetic phenomena in boundary films of liquids.* Kolloidn. Zh, 1947. **9**: p. 335-347.
129. Prieve, D.C. and R. Roman, *Diffusiophoresis of a rigid sphere through a viscous electrolyte solution.* Journal of the Chemical Society, Faraday Transactions 2, 1987. **83**(8): p. 1287.
130. Ebel, J.P., J.L. Anderson, and D.C. Prieve, *Diffusiophoresis of latex particles in electrolyte gradients.* Langmuir, 1988. **4**(2): p. 396-406.
131. Anderson, J.L., *Colloid Transport by Interfacial Forces.* Annual Review of Fluid Mechanics, 1989. **21**(1): p. 61-99.
132. Keh, H.J., *Diffusiophoresis*, in *Encyclopedia of Microfluidics and Nanofluidics*, D. Li, Editor. 2008, Springer-Verlag: Boston, MA.
133. Florea, D., et al., *Long-range repulsion of colloids driven by ion exchange and diffusiophoresis.* Proceedings of the National Academy of Sciences of the United States of America, 2014. **111**(18): p. 6554-6559.
134. Shin, S., et al., *Size-dependent control of colloid transport via solute gradients in dead-end channels.* Proceedings of the National Academy of Sciences of the United States of America, 2016. **113**(2): p. 257-261.
135. Palacci, J., et al., *Osmotic traps for colloids and macromolecules based on logarithmic sensing in salt taxis.* Soft Matter, 2012. **8**(4): p. 980-994.

136. Wanunu, M., et al., *Electrostatic focusing of unlabelled DNA into nanoscale pores using a salt gradient.* Nature nanotechnology, 2010. **5**(2): p. 160-165.
137. Chou, T., *Enhancement of charged macromolecule capture by nanopores in a salt gradient.* The Journal of Chemical Physics, 2009. **131**(3): p. 034703.
138. Maeda, Y.T., *(2+1)-Dimensional manipulation of soft biological materials by opto-thermal diffusiophoresis.* Applied Physics Letters, 2013. **103**(24): p. 243704.
139. Astorga-Wells, J. and H. Swerdlow, *Fluidic Preconcentrator Device for Capillary Electrophoresis of Proteins.* Analytical chemistry, 2003. **75**(19): p. 5207-5212.
140. Song, Y.-A., et al., *Continuous-Flow pI-Based Sorting of Proteins and Peptides in a Microfluidic Chip Using Diffusion Potential.* Analytical chemistry, 2006. **78**(11): p. 3528-3536.
141. Annunziata, O., D. Buzatu, and J.G. Albright, *Protein Diffusiophoresis and Salt Osmotic Diffusion in Aqueous Solutions.* The Journal of Physical Chemistry B, 2012. **116**(42): p. 12694-12705.
142. Fukuyama, T., et al., *Directing and Boosting of Cell Migration by the Entropic Force Gradient in Polymer Solution.* Langmuir, 2015. **31**(46): p. 12567-12572.
143. Rye, H.S. and A.N. Glazer, *Interaction of dimeric intercalating dyes with single-stranded DNA.* Nucleic acids research, 1995. **23**(7): p. 1215-1222.
144. Meagher, R.J. and N. Thaitrong, *Microchip electrophoresis of DNA following preconcentration at photopatterned gel membranes.* Electrophoresis, 2012. **33**(8): p. 1236-1246.
145. Li, X., L. Luo, and R.M. Crooks, *Low-voltage paper isotachophoresis device for DNA focusing.* Lab on a Chip, 2015. **15**(20): p. 4090-4098.
146. Schurr, J.M., et al., *A theory of macromolecular chemotaxis.* Journal of physical chemistry B, 2013. **117**(25): p. 7626-52.
147. Abecassis, B., et al., *Boosting migration of large particles by solute contrasts.* Nature Materials, 2008. **7**(10): p. 785-789.
148. Smith, R.E. and D.C. Prieve, *Accelerated deposition of latex particles onto a rapidly dissolving steel surface.* Chemical Engineering Science, 1982. **37**(8): p. 1213-1223.
149. Golestanian, R., T.B. Liverpool, and A. Ajdari, *Propulsion of a Molecular Machine by Asymmetric Distribution of Reaction Products.* Physical Review Letters, 2005. **94**(22): p. 220801.
150. Paxton, W.F., et al., *Catalytic Nanomotors: Autonomous Movement of Striped Nanorods.* Journal of the American Chemical Society, 2004. **126**(41): p. 13424-13431.
151. Howse, J.R., et al., *Self-Motile Colloidal Particles: From Directed Propulsion to Random Walk.* Physical Review Letters, 2007. **99**(4): p. 048102.
152. Odagiri, K., K. Seki, and K. Kudo, *Ring formation by competition between entropic effect and thermophoresis.* Soft Matter, 2012. **8**(25): p. 6775-6781.
153. Maeda, Y.T., T. Tlusty, and A. Libchaber, *Effects of long DNA folding and small RNA stem–loop in thermophoresis.* Proceedings of the National Academy of Sciences of the United States of America, 2012. **109**(44): p. 17972-17977.
154. Shi, N., et al., *Diffusiophoretic Focusing of Suspended Colloids.* Physical Review Letters, 2016. **117**(25): p. 258001.
155. Bharadwaj, R. and J.G. Santiago, *Dynamics of field-amplified sample stacking.* Journal of Fluid Mechanics, 2005. **543**: p. 57-92.
156. Boček, P., et al., *Analytical Isotachophoresis*. 1988: VCH.

157. Kitagawa, F. and K. Otsuka, *Recent applications of on-line sample preconcentration techniques in capillary electrophoresis.* Journal of Chromatography A, 2014. **1335**: p. 43-60.
158. Malá, Z., P. Gebauer, and P. Boček, *Analytical capillary isotachophoresis after 50 years of development: Recent progress 2014–2016.* Electrophoresis, 2017. **38**(1): p. 9-19.
159. Paik, D.H. and T.T. Perkins, *Dynamics and Multiple Stable Binding Modes of DNA Intercalators Revealed by Single-Molecule Force Spectroscopy.* Angewandte Chemie International Edition, 2012. **51**(8): p. 1811-1815.
160. Nyberg, L., et al., *Heterogeneous staining: a tool for studies of how fluorescent dyes affect the physical properties of DNA.* Nucleic Acids Research, 2013. **41**(19): p. e184-e184.
161. Rane, T.D., H.C. Zec, and T.H. Wang, *A Serial Sample Loading System: Interfacing Multiwell Plates with Microfluidic Devices.* Jala, 2012. **17**(5): p. 370-377.
162. Mathies, R.A. and X.C. Huang, *Capillary Array Electrophoresis - an Approach to High-Speed, High-Throughput DNA Sequencing.* Nature, 1992. **359**(6391): p. 167-169.
163. Harrison, D.J., et al., *Capillary Electrophoresis and Sample Injection Systems Integrated on a Planar Glass Chip.* Analytical Chemistry, 1992. **64**(17): p. 1926-1932.
164. Lacher, N.A., et al., *Microchip capillary electrophoresis/electrochemistry.* Electrophoresis, 2001. **22**(12): p. 2526-2536.
165. Wu, J.K., et al. *Chip-based DNA separation in free solution by inertial hydrodynamic forces*. in *Proceedings of The 17th International Conference on Miniaturized Systems for Chemistry and Life Sciences*. 2013. Freiburg, Germany: The Printing House, Inc.
166. Xu, Z., et al., *Another Approach Toward over 100 000-Fold Sensitivity Increase in Capillary Electrophoresis: Electrokinetic Supercharging with Optimized Sample Injection.* Analytical chemistry, 2011. **83**(1): p. 398-401.

Curriculum Vitae

Sarah M. Friedrich

Cell: 443-789-4109
E-Mail: smfriedri@gmail.com

714 W. 33rd St.
Baltimore, MD 21211

EDUCATION:

Doctorate of Philosophy, Biomedical Engineering March 2018 (expected)
Johns Hopkins Medical Institution (JHU), Baltimore MD
GPA: 4.0/4.0
Advisor: Jeff Tza-Huei Wang
Thesis: "A Versatile Platform for Highly Sensitive Analysis of DNA Size, Conformation, and Binding Interactions in Free Solution"

Bachelors of Mechanical Engineering with Distinction *summa cum laude* May 2011
University of Delaware (UD), Newark DE
GPA: 3.98/4.0
Minor: Mathematics
Advisor: Erik Thostenson
Senior Thesis: "Processing and Electrical Characterization of Nanocomposites for Damage Detection in Composite Joints "

HONORS, AWARDS, AND AFFILIATIONS:

• Siebel Scholar Class of 2018, *Siebel Foundation*	September 2017
• Second Place 2017 JHGCC Spring Biotech and Healthcare Case Competition, *JHU*	April 2017
• Best Paper Award, *IEEE MEMS 2016 Conference*	January 2016
• Institute for NanoBio Technology (INBT) Member, *JHU*	Fall 2011 – Spring 2016
• NSF Graduate Research Fellow	September 2012 – September 2015
• Young Researcher Poster Competition: Finalist, *MicroTAS 2013*	October 2013
• Graduate Research Intern, *INBT, JHU, Baltimore MD and IMEC, Lueven BE*	Summer 2012
• Fundamentals of Engineering (FE)	Spring 2011
• SAMPE Senior Student Award International Competition 2nd Place	May 2011
• W. Francis Lindell Mechanical Engineering Award to the Outstanding Senior, *UD*	May 2011
• Undergraduate Research Award, *CCM, UD*	May 2010
• W. Francis Lindell Mechanical Engineering Award to the Outstanding Junior, *UD*	May 2010
• Dean's List, *UD*	Fall 2007 – Spring 2011
• General Honors Award, *UD*	November 2009
• Science and Engineering Scholar, *UD*	May 2009
• Scholarship Winner, *Social Security Administration, Baltimore, MD*	Fall 2007 & 2008

- Honors Program Member, *UD* Fall 2007 – Spring 2011
- Academic Scholarship Recipient, *UD* Fall 2007 – Spring 2011

TEACHING EXPERIENCE:

- Cell and Tissue Engineering Lab, *Teaching Assistant, JHU* Spring 2015
- Microfabrication Lab, *Lab Assistant, JHU* Spring 2015 & 2016
- Molecules and Cells, *Teaching Assistant, JHU* Fall 2014
- Computer Aided Design Lab, *Teaching Assistant, UD* Spring 2011
- Mechanics of Solids Lab, *Teaching Assistant, UD* Fall 2010

LEADERSHIP, MENTORING, AND OUTREACH:

- Mentor for undergraduate researchers, *BioMEMS Lab, JHU* Fall 2013 – Present
    a. Student: Rachel Bang “Optimization of single-molecule hydrodynamic separations for DNA/protein interactions”
- Study Buddy tutor, *Hampden Family Center, Baltimore, MD* 2015-18 School Years (Present)
- Afterschool science and engineering mentor to Baltimore City elementary school students, *SABES program* 2015-17 School Years
- WISE project host and mentor to high school student, *Women in Science and Engineering (WISE) program, JHU* October 2015 – February 2016
    a. Vasiliki Argeroplos “Quantification of DNA Preconcentration with Varied Counter-Flow Rate”
- Science Fair Judge, Engineering Section, Montgomery County Science Fair Spring 2015 & 2016
- Lead Mentor for Baltimore City high school student, *Incentive Mentoring Program (IMP), Baltimore, MD* Fall 2013 – Fall 2014
- Mentor for Baltimore City high school student, *Incentive Mentoring Program (IMP), Baltimore, MD* Fall 2011 – Fall 2013
- Secretary and Outreach Coordinator, *Society for the Advancement of Material and Process Engineering (SAMPE), UD Chapter* 2010-11 School Year

ADDITIONAL EXPERIENCE:

- Graduate Research Intern, *INBT, JHU, Baltimore MD and IMEC, Lueven BE* Summer 2012
- Math Tutor, *Academic Enrichment Center, UD, Newark DE* Fall 2008 – Spring 2011
- Science and Engineering Scholar, *UD* Summer 2009
- General Contracting Engineering Intern, *The Whiting-Turner Contracting Company, Baltimore MD* Summer 2008

PUBLICATIONS:

1. **S. M. Friedrich**, R. Bang, A. Li, and T-H Wang. “Hydrodynamic Separation and Single Molecule Detection Streamlines Multiparametric Analysis of DNA-Biomolecule Interactions in Free Solution” (*in preparation*).
2. H. S. Antila, **S. M. Friedrich**, T-H Wang, and E. Luijten, “Controlling the Hydrodynamic Separation of Polyelectrolytes by Ionic Strength” (*in preparation*).
3. **S. M. Friedrich**, J. M. Burke, K. J. Liu, C. F. Ivory, and T-H Wang, “Molecular Rheotaxis Directs DNA Migration and Concentration Against a Pressure-Driven Flow”. *Nature Communications*. 2017; 8; 10.1038/s41467-017-01214-y.

4. Y. Zhang, Y. Zhang, J. M. Burke, K. Gleistman, **S. M. Friedrich**, K. J. Liu, and T-H Wang, "A Simple Thermoplastic Substrate Containing Hierarchical Silica Lamellae for High Molecular Weight DNA Extraction". *Advanced Materials*. 2016; 28: 10630–10636.
5. Y-H Lao, C-W Chi, **S. M. Friedrich**, K. Peck, T-H Wang, K. W. Leong, and L-C Chen, "Signal-On Protein Detection via Dye Translocation Between Aptamer and Quantum Dot". *ACS Applied Materials & Interfaces*. 2016; 8(19):12048-12055.
6. **S. M. Friedrich**, H. C. Zec, and T-H Wang, "Analysis of Single Nucleic Acid Molecules in Micro- and Nano- Fluidics". *Lab on a Chip*. 2016; 16(5):790-811.
7. **S. M. Friedrich**, K. J. Liu, and T-H Wang, "Single Molecule Hydrodynamic Separation Allows Sensitive and Quantitative Analysis of DNA Conformation and Binding Interactions in Free Solution". *Journal of the American Chemical Society*. 2016; 138(1):319-327.
8. A. Kundu, L. Micholt, **S. M. Friedrich**, D. R. Rand, C. Bartic, D. Braeken, A. Levchenko, "Superimposed topographic and chemical cues synergistically guide neurite outgrowth." *Lab on a Chip*. 2013; 13(15):3070-3081.
9. **S. M. Friedrich**, A. S. Wu, E. T. Thostenson, and T-W Chou, "Damage mode characterization of mechanically fastened composite joints using carbon nanotube networks." *Composites Part A*. 2011; 42(12):2003-2009.

CONFERENCE PROCEEDINGS AND PRESENTATIONS:

Peer-reviewed Conference Papers:

1. **S. M. Friedrich**, J. M. Burke, K. J. Liu, and T-H Wang, "In-Line DNA Preconcentration, Size Separation, and Single Molecule Detection without Applied Electric Fields". 29th *IEEE International Conference on Micro Electro Mechanical Systems (IEEE MEMS 2016)*. 181-184.
2. **S. M. Friedrich**, K. J. Liu, and T-H Wang, "Single Molecule Hydrodynamic Separation for Ultrasensitive and Quantitative DNA Size Separation." *17th International Conference on Miniaturized Systems for Chemistry and Life Sciences (MicroTAS 2013)*. 35-37.
3. **J-K Wu, S. M. Friedrich**, K. J. Liu, and T-H Wang, "Chip-Based DNA Separation in Free Solution by Inertial Hydrodynamic Forces". *17th International Conference on Miniaturized Systems for Chemistry and Life Sciences (MicroTAS 2013)*. 578-580.
4. K. J. Liu, T. D. Rane, Y. Zhang, C. Beh, **S. M. Friedrich**, D. J. Shin, and T-H Wang, "An Integrated Platform for Single Molecule Free Solution Hydrodynamic Separation Using Yoctomoles of DNA and Picoliter Samples." *ASME 2012 10th International Conference on Nanochannels, Microchannels and Minichannels (ICNMM 2012),* ICNMM2012-73154. 1-5.

Conference Abstracts and Presentations:

1. Y. Zhang, Y. Zhang, J. M. Burke, K. Gleistman, **S. M. Friedrich**, K. J. Liu, T-H Wang, "Shrinking-Induced Silica Lamella For High-Molecular Weight DNA Extraction". *IEEE Nanotechnology Materials and Devices Conference (NMDC 2017), (October 2, 2017)*.
2. **S. M. Friedrich**, J. M. Burke, K. J. Liu, T-H Wang, and C. F. Ivory, "Concentration then Separation of Double-Stranded DNAs using an Open Capillary without an Applied Electric Field". *72nd Annual Northwest Regional Meeting of the American Chemical Society (NORM 2017), (June 26, 2017)*.
3. A. Li, **S. M, Friedrich**, and T-H Wang, "Free Solution Sizing and Conformational Analysis of Single Molecules". *Johns Hopkins Nano-Bio Symposium, (May 5, 2017)*.
4. A. Li, **S. M, Friedrich**, and T-H Wang, "Free Solution Sizing and Conformational Analysis of Single Molecules". *Chesapeake Bay Area Single Molecule Biology Meeting (CBASMB 2017), (April 8, 2017)*.
5. **S. M. Friedrich** and T-H Wang, "Separation and Characterization of DNA Molecules and Intermolecular Interactions in Pressure-Driven Micro Flow". *APS March Meeting 2017, (March 13, 2017).*

6. C. F. Ivory, J. M. Burke, **S. M. Friedrich**, T-H Wang, and K. J. Liu, “Extraction, Concentration and Separation of dsDNAs Using an Open Capillary Without an Applied Electric Field”. *The 43rd Annual North American Meeting of the Federation of Analytical Chemistry and Spectroscopy Societies (FACSS) (SciX 2016), (September 20, 2016).*
7. **S. M. Friedrich**, J. M. Burke, K. J. Liu, T-H Wang, and C. F. Ivory, “Extraction, Concentration and Separation of DsDNAs Using an Open Capillary Without an Applied Electric Field”. *40th International Symposium on Capillary Chromatography (ISCC), (June 3, 2016)*.
8. **S. M. Friedrich**, J. M. Burke, K. J. Liu, and T-H Wang, “Counter-Flow DNA Preconcentration Without Applied Electric Fields”. *ASME 2016 NanoEngineering for Medicine and Biology Conference (NEMB 2016),* (*Feb 23, 2016*).
9. J. M. Burke, **S. M. Friedrich**, C. F. Ivory, T-H Wang, and K. J. Liu, “Inline Sample Preconcentration for Single Molecule DNA Sizing”. *AIChE Annual Meeting: 2015 Annual Meeting of the AES Electrophoresis Society, (November 11, 2015).*
10. **S. M. Friedrich**, A. S. Wu, and E. T. Thostenson, “Influence of Calendering on Carbon Nanotube/Polymer Composites for *In Situ* Damage Sensing Applications,” *SAMPE Long Beach 2011 Conference and Exhibition, (May 24, 2011).*